UNIVERSITY OF CALIFORNIA SAN DIEGO

Wakes of underwater hills : Vortex dynamics, Form drag and Turbulence

A dissertation submitted in partial satisfaction of the
requirements for the degree
Doctor of Philosophy

in

Engineering Sciences (Mechanical Engineering)

by

Pranav Puthan Naduvakkate

Committee in charge:

Professor Sutanu Sarkar, Chair
Professor Eugene Pawlak, Co-Chair
Professor Matthew Alford
Professor Jennifer MacKinnon
Professor Oliver Schmidt

2021

The dissertation of Pranav Puthan Naduvakkate is approved, and it is acceptable in quality and form for publication on microfilm and electronically.

University of California San Diego

2021

DEDICATION

To my parents, Suresh and Premila

and my brother Prathiv

TABLE OF CONTENTS

LIST OF FIGURES

LIST OF TABLES

ACKNOWLEDGEMENTS

I express my sincere thanks to my advisor Prof. Sutanu Sarkar for all his support and guidance during my PhD. His support has been invaluable. I would also like to thank Prof. Geno Pawlak, my co-advisor, for his mentorship. I would like to thank all my thesis committee members : Prof. Oliver Schmidt, Prof. Jennifer MacKinnon and Prof. Matthew Alford for their helpful suggestions and encouragement. I am grateful for the financial support provided through the National Science Foundation (NSF) grants OCE-1459774 and OCE-1737367.

I thank the recent graduates from the CFD lab Dr. Masoud Jalali, Prof. Vamsi Chalamalla, Prof. Karu Chongsiripinyo and Dr. Jose Luis Ortiz-Tarin for their guidance and support. Their training and mentorship helped me navigate my initial learning curve and provide motivation to stay on my pursuit despite occasional roadblocks. As my co-authors, they have helped me a lot in the research and I am extremely grateful to them. I would also like to thank Dr. Hieu Pham for his research ideas. I would also like to make a special mention of his help in academic writing which has been very useful during my PhD.

Our group was very friendly and supportive. Discussions with Dr. Sungwon Lee, Dr. Vicky Verma, Sheel Nidhan, Akhil Nekkanti and Divanshu Gola were a lot of fun. I would also like to thank Jinyuan Liu. His intriguing questions often motivated me to explore new ideas in my work.

During graduate school, I made many friends outside my work, who have shaped my life : Jacob Johnson, Rohit Parasnis, Aditya Sant, Achal Mahajan, Ajay Mohan, Tapan Goel, Kumaran Gunasekaran, Vinay Kumar and Nikita Kharat. Their help and support was invaluable and they played an important role in my journey.

Finally, I would like to thank my parents, my brother and my cousins for their support during this journey. They have stood beside me during the challenging times of my life and I cannot imagine finishing graduate school without their support.

The contents of Chapter 2 are published in *Ocean Modeling*. P. Puthan, M. Jalali, J. L. Ortiz-Tarin, K. Chongsiripinyo, G. Pawlak and S. Sarkar, The wake of a three-dimensional underwater obstacle: effect of bottom boundary conditions, *Ocean Modeling*, 149, 2020. The dissertation author was the primary investigator and author of this paper.

The contents of Chapter 3 are published in *Geophysical Research Letters*. P. Puthan, S. Sarkar and G. Pawlak, Tidal synchronization of lee vortices in geophysical wakes, *Geophysical Research Letters*, 48, 2021. The dissertation author was the primary investigator and author of this paper.

The contents of Chapter 4, in part, has been submitted for publication and it may appear in *Journal of Physical Oceanography*. P. Puthan, S. Sarkar and G. Pawlak, High drag states in tidally distorted stratified wakes, 2022. The dissertation author was the primary investigator and author of this paper.

The contents of Chapter 5 is currently being prepared for submission, for publication of the material. P. Puthan, S. Sarkar and G. Pawlak. The dissertation author was the primary investigator and author of this paper.

The contents of Chapter 6 are published in *Journal of Fluid Mechanics*. P. Puthan, M. Jalali, V. K. Chalamalla and S. Sarkar, Energetics and mixing in buoyancy-driven near-bottom stratified flow, *Journal of Fluid Mechanics*, 869, 2019. The dissertation author was the primary

investigator and author of this paper.

VITA

2021	Ph.D. in Engineering Sciences (Mechanical Engineering), University of California San Diego
2017	M.S. in Engineering Sciences (Mechanical Engineering), University of California San Diego
2016	M.Tech. in Applied Mechanics, Indian Institute of Technology, Madras, India
2016	B.Tech. in Naval Architecture and Ocean Engineering, Indian Institute of Technology, Madras, India

PUBLICATIONS

Pranav Puthan, S. Sarkar, G. Pawlak, Wake vortices and dissipation in tidally modulated abyssal hill wakes, in preparation.

Pranav Puthan, S. Sarkar, G. Pawlak, High drag states in tidally distorted wakes, under review for publication in *Journal of Physical Oceanography*.

Pranav Puthan, S. Sarkar, G. Pawlak, Tidal synchronization of lee vortices in geophysical wakes, *Geophysical Research Letters*, 48, 2021.

Pranav Puthan , M. Jalali, J. L. Ortiz-Tarin, K. Chongsiripinyo, S. Sarkar and G. Pawlak, The wake of a three-dimensional underwater obstacle: effect of bottom boundary conditions, *Ocean Modeling*, 149, 2020.

Pranav Puthan, M. Jalali, V. K. Chalamalla, S. Sarkar, Energetics and mixing in buoyancy-driven near-bottom stratified flow, *Journal of Fluid Mechanics*, 869, 2019.

ABSTRACT OF THE DISSERTATION

Wakes of underwater hills : Vortex dynamics, Form drag and Turbulence

by

Pranav Puthan Naduvakkate

Doctor of Philosophy in Engineering Sciences (Mechanical Engineering)

University of California San Diego, 2021

Professor Sutanu Sarkar, Chair
Professor Eugene Pawlak, Co-Chair

Wakes of three-dimensional topographies in the abyssal ocean are sites of enhanced flow variability and mixing. To investigate the attendant vortex dynamics, internal waves and turbulence, a three-phased approach is adopted. In the first phase, a steady current impinges on a conical abyssal hill in a stratified environment. The sensitivity of the flow to boundary conditions (slip and partial-slip instead of no-slip) on the flat wall and on the obstacle surface is examined. Significant changes occur in the structure of lee vortices and wake turbulence when the boundary condition (BC) is changed. For instance, the boundary layer on the flat bottom in the no-slip case suppresses the unsteady behavior of the separated boundary layer

behind the hill. In contrast, unsteady shedding of vortices from the body in a high Reynolds number flow is captured by slip and partial-slip BCs.

In the second phase, tidal modulations are superimposed on the steady flow to study the changes in vortex dynamics in the abyssal hill wake. The strength of the tidal modulations relative to the mean flow (R) and the tidal excursion number (Ex) are varied to reveal tidal synchronization of wake vortices. The ratio of the natural shedding frequency to the tidal frequency (f^*) varies from 0.1 to 1 when Ex is varied, at $R = 1$. Wake vortices are observed at the subharmonics of the tidal frequency when $0.25 \leq f^* \leq 1$. Even weak tidal modulations ($R \sim O(0.1)$) can alter the frequency of these wake vortices. Qualitative changes are observed in the spatial organization of the vortices, which influences form drag and dissipation.

In the third phase, a statically unstable disturbance (originating from internal wave propagation) over a slope with inclination β and background buoyancy frequency N is considered. The energy exchange occurs between four energy reservoirs, namely the mean and turbulent components of kinetic energy (KE) and available potential energy (APE). When β is non-zero, a mean flow is initiated at a frequency of $N \sin\beta$ accompanied by an oscillatory energy exchange between the mean KE and APE reservoirs. The energy transfer between the mean and turbulent reservoirs of KE and APE is explored.

Chapter 1

Introduction

Turbulent mixing in the ocean interior is a key control on the meridional overturning circulation (Wunsch and Ferrari, 2004) and quantification of mixing in the ocean is critical to predictions related to the ocean circulation (Saenko and Merryfield, 2004). Turbulent dissipation is intensified by encounters of stratified flow with rough topography, a finding that has often been attributed predominantly to topographic internal waves. However, the contribution of mixing from wakes of underwater multiscale topography has received less attention in observational studies. With the advent of computing power and improved simulation techniques, our ability to model wakes of flow past topography has advanced. Wakes of islands and seamounts have been simulated using ocean circulation models with early efforts by Beckmann and Haidvogel (1997); Coutis and Middleton (2002) and more recent work by Dong et al. (2007); Liu and Chang (2018); Perfect et al. (2018). Flow separation and eddy formation off coastal topography has been examined for the California Undercurrent (Molemaker et al., 2015), the Gulf Stream (Gula et al., 2015), and for tidally modulated currents past Three Tree Point in the context of form drag (Warner and MacCready, 2014). Notably, submesoscale eddies with large vertical vorticity (relative to the inertial frequency) are injected into the flow. On the other hand, measurements in the abyssal ocean reveal strong boundary currents and elevated

turbulent dissipation rates at bottom mixed layers (Polzin et al., 2014; Ruan et al., 2017; Garabato et al., 2019). The increasing resolution of ocean models also reveal the importance of topographic features, e.g., enhanced tracer mixing as the Antarctic Circumpolar Current (ACC) passes through the Drake Passage (Mashayek et al., 2017) and enhanced submesoscale vortices as the ACC negotiates the Kerguelen Plateau in the South Indian Ocean (Rosso et al., 2015).

Stratification, rotation and tidal forcing are key elements of geophysical wakes. When a tidally modulated flow encounters an underwater obstacle, the wake structure is governed predominantly by the obstacle Froude number (Fr_c), the tidal excursion number (Ex_t), the Rossby number (Ro_c) and velocity ratio (R) :

$$Fr_c = \frac{U_c}{Nh} \quad ; \quad Ex_t = \frac{U_t}{\Omega_t D} \quad ; \quad Ro_c = \frac{U_c}{fD} \quad ; \quad R = \frac{U_t}{U_c} \,,$$

where U_c and U_t are the mean and tidal constituents of the barotropic flow respectively, N is the background buoyancy frequency, $\Omega_t = 2\pi f_t$ is the tidal frequency, f is the inertial frequency, h is the height of the obstacle and D is the obstacle base diameter.

The topographic length scale can vary significantly in the ocean. Large seamount wakes span over distances of O(50km) while the signature of wakes generated by smaller topographies, including small island wakes, extend upto O(4km). Underwater topography is 3D with multiple length scales, e.g. see fig. 1.1 which shows 3D bumps at $O(1-10)$ km horizontal scale in the double-ridge Luzon Strait. Recent observations of eddy formation in the wake of Palau island (Zeiden et al., 2019; MacKinnon et al., 2019) depicts wake eddies formed by a complex interaction of a tidally modulated current with the island (see fig. 1.2). These eddies possess relative vorticity of the $O(\sim 30f)$ and the tide has an excursion length of O(8km), where f is the inertial frequency. Similar strong eddies were observed by Chang et al. (2019) at Taiwan's, Green Island. The cross-stream tidal flow is observed to affect the

vortex shedding frequency although its amplitude is five times weaker than the background Kuroshio current impinging on the island. The shedding of vortices occurs at M2 frequency instead of the natural period of shedding.

In unstratified environments, a hill with a 3D geometry does not shed vortices similar to the vertically coherent lee eddies which are observed in the ocean. Instead a standing horseshoe vortex and periodic hairpin vortices are observed downstream at low Reynolds number (Re_D) (see Acarlar and Smith, 1987) which become indistinct at higher Reynolds number (Garcia-Villalbaa et al., 2009). A low Fr_c ($Fr_c \ll 1$) flow is constrained to move around rather than over the obstacle, owing to the large potential energy barrier. This leads to roll-up of the lateral shear layer into lee vortices (Hunt and Snyder, 1980).

Topographic wakes are also affected by planetary rotation. A relatively large planetary rotation rate (small Ro_c) induces asymmetry in the strength of cyclonic and anticyclonic eddies shed from the topography (Dietrich et al., 1996). Dong et al. (2006) attributed the loss in symmetry to centrifugal instabilities in the wake. Perfect et al. (2018) and Srinivasan et al. (2018) showed that the change in vertical structure of wake vortices is governed by the Burger number Bu, defined as $(Ro_c/Fr_c)^2$. Their idealized simulations show decoupling of vortices along their vertical extent owing to loss of geostrophic balance, when $Bu > 12$.

The regime of weak rotation and strong stratification (or equivalently, large Bu) applies to wakes behind abyssal hills. For example, consider the abyssal hills in the Brazil Basin (Ledwell et al., 2000; Nikurashin and Legg, 2011). The bottom topographic roughness is $O(1$ km) in the horizontal. For an obstacle with $D = 1.5$ km, buoyancy period of 1 hr and $U_c = U_t = 10$ cm/s, the tidal excursion number is $Ex_t \approx 0.5$ for the M2 tide and the average value of Fr_c lies close to 0.2. The value of Rossby number is $Ro_c \approx 3$, at 15°S latitude. The resolution of GCMs is insufficient to resolve these hills. Thus, parametrization of the wake dynamics at these length scales is critical.

Owing to numerical constraints, idealized simulations often ignore tidal forcing. Yet,

in situ observations affirm that tides can significantly influence flow separation at islands, continental slopes and submerged topography. Observations by Black and Gay (1987) showed the formation of 'phase' eddies in the continental shelf of Great Barrier Reef. Denniss et al. (1995) and Chang et al. (2019) reported lee eddies shed past islands at the dominant tidal frequency. This phase-locking phenomenon is observed even when the tidal velocity amplitude is small relative to the mean flow. A lack of numerical studies exploring these findings motivates this research on numerical modeling of abyssal hill wakes. We perform turbulence-resolving simulations of wakes past an idealized conical underwater hill to explore the vortex dynamics, form drag and turbulence in this realm. Planetary rotation, stratification and tidal forcing are included for accurate representation of the abyssal ocean environment. Thus, these simulations capture the essential features of a class of turbulent flows that exists in the ocean. Numerical challenges in modeling these wakes are also addressed.

This dissertation is organized as follows. Chapter 2 presents simulations of a steady current impinging on a conical abyssal hill. Numerical challenges in modeling abyssal wakes are discussed to highlight the effect of numerical boundary conditions on the characteristics of the shed lee vortices. Additionally, the progenitors of lee vorticity and their relative contributions are assessed to reveal the role of stratification in such wakes. In chapter 3, a tide with strength equal to the mean is added to the background flow. In this parametric study, the relative magnitude of the natural shedding frequency to the tidal frequency is varied. Far wake vortices were found to be tidally synchronized. Specifically, these vortices were observed at tidal subharmonics, a novel result. Notable changes were also observed in the spatial organization of vortices and form drag. The vortex shedding patterns are classified into three distinct regimes. A detailed investigation of form drag in each regime is presented in chapter 4.

Although tidal synchronization is found here when the tidal velocity is as strong as the background current, the influence of weaker tidal modulations on wake vortices is still

unknown. To this end, the magnitude of the tidal modulation relative to the mean flow is varied in chapter 5 to examine the onset of synchronized wake vortices. The underlying mechanisms responsible for changes in the wake vortex frequency are discussed. Chapter 5 concludes with a brief discussion on dissipation 'hot-spots' in the lee of the hill. The discussion of turbulence and dissipation is incomplete when the contribution of IW driven mixing is excluded. Therefore to complete the picture, a statically unstable disturbance at a slope β generated by IW propagation is considered in chapter 6. The flow evolution involves energy exchange between four energy reservoirs, namely the mean and turbulent components of kinetic energy (KE) and available potential energy (APE). The influence of β and initial disturbance amplitude on the energy exchange are investigated in this parametric study.

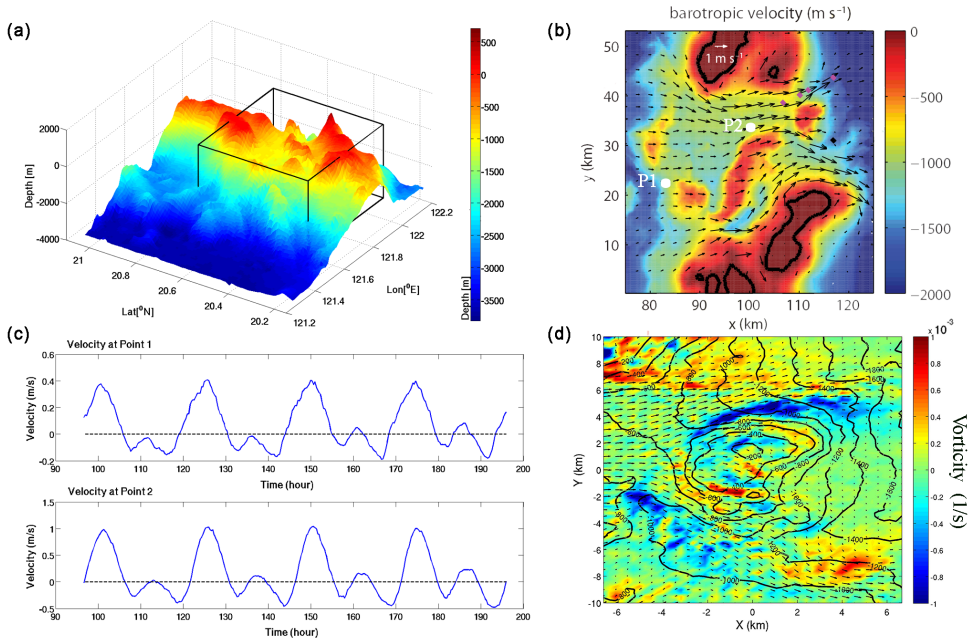

Figure 1.1: Rough underwater topography in the ocean: (a) A central section of the east ridge of Luzon Strait, a steep double-ridge system. Although the topography is elongated in the north-south direction so as to present a quasi-two dimensional geometry akin to a ridge, there are several three-dimensional topographic features. (b) Barotropic (depth-averaged) velocity in a zoom of the rectangular box in part (a) shows flow in a channel with submerged 3D hills (from Pinkel et al. (2012)) (c) Barotropic velocity at points P1 and P2 show asymmetry with mean and oscillating components of the same order. (d) Vertical vorticity of the boundary flow around three-dimensional features is large ($\approx 20f$). (b) and (c) based on simulation data provide by M. Buijsman and reported by Buijsman et al. (2012)

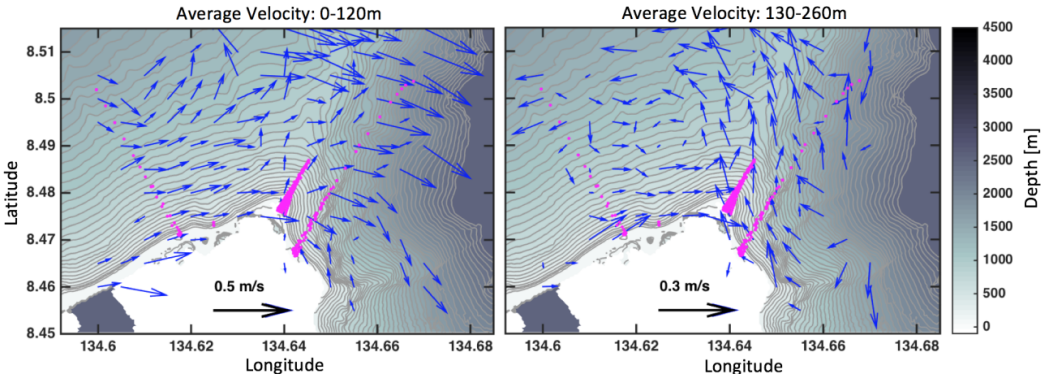

Figure 1.2: Observations of flow around three-dimensional topography from shipboard surveys around the northern tip of Palau. a) Velocities averaged over 0-120m showing eastward flow with flow separation evident in the lee. b) Velocities averaged over 130-260m with westward flow and wake/eddy structure evident to the west of the tip. Data provided by MacKinnon et al. (2019)

Chapter 2

The wake of a three-dimensional underwater obstacle: effect of bottom boundary conditions

Three-dimensional (3D) obstacles on the bottom are common sites for the generation of vortices, internal waves and turbulence by ocean currents. Turbulence-resolving simulations are conducted for stratified flow past a conical hill, a canonical example of 3D obstacles. Motivated by the use of slip boundary condition (BC) and drag-law (effectively partial slip) BC in the literature on geophysical wakes, we examine the sensitivity of the flow to BCs on the obstacle surface and the flat bottom. Four BC types are examined for a non-rotating wake created by a steady current impinging on a conical obstacle, with a detailed comparison being performed between two cases, namely **NOSL** (no-slip BC used at all solid boundaries) and **SL** (slip BC used at all solid boundaries). The other two cases are as follows: **Hybrid**, undertaken with slip at the flat bottom and no-slip at the obstacle boundaries, and case **DL** wherein a quadratic drag-law BC is adopted on all solid boundaries. The no-slip BC allows the formation of a boundary layer which separates and sheds vorticity into the wake. Significant

changes occur in the structure of the lee vortices and wake when the BC is changed. For instance, bottom wall friction in the no-slip case suppresses unsteadiness of flow separation leading to a steady attached lee vortex. In contrast, when the bottom wall has a slip BC (the **SL** and **Hybrid** cases) or has partial slip (**DL** case), unsteady separation leads to a vortex street in the near wake and the enhancement of turbulence. The recirculation region is shorter and the wake recovery is substantially faster in the case of slip BC. In the lee of the obstacle, turbulent kinetic energy (TKE) for case **NOSL** is concentrated in a shear layer between the recirculating wake and the free stream, while TKE is bottom-intensified in the other three cases. The sources of lee vorticity are also examined in this study for each choice of BC. The sloping sides lead to horizontal gradients of density at the obstacle, which create vorticity through baroclinic torque. Independent of the type of BC, the baroclinic torque dominates. Vortex stretch and tilt are also substantial. An additional unstratified free-slip case (**SL-UN**) is simulated and the wake is found to be thin without large wake vortices. Thus, stratification is necessary for the formation of coherent lee vortices of the type seen in geophysical wakes.

2.1 Introduction

Wakes are generated as the flow separates at three-dimensional (3D) steep, multiscale bathymetry, e.g. at Luzon Strait (Zheng et al., 2008; Pinkel et al., 2012; Buijsman et al., 2014). Separated flow and wake eddies in stratified water, for example, at the headlands of Three Tree Point (Pawlak et al., 2003; Canals et al., 2008) and Palau (MacKinnon et al., 2019) lead to form drag and, additionally, to turbulent dissipation and mixing. Stratification exerts significant dynamic control in these examples and in the model problem simulated here, unlike the more studied configuration of island wakes in shallow, well-mixed water. The role of wake vortices and attendant flow variability in flow past submerged topography has received less attention than internal waves, motivating the present study of a canonical problem of stratified

flow past a conical hill with a focus on wake dynamics. Consider a current of characteristic speed $U_c = U_0$ in a stratified background with buoyancy frequency N and Coriolis frequency f. As the current flows past an obstacle of horizontal length scale D and height h, a flow is established with dynamics governed by the following non-dimensional parameters: (1) Reynolds number (Re_D) defined as $U_0 D/\nu$ where ν is the viscosity, (2) topographic Froude number (Fr_c) defined as U_0/Nh, (3) topographic Rossby number (Ro) defined as U_0/fD, and (4) topographic slope h/D. The value of Fr_c is quite variable in deep water. For example, in the Southern Ocean, a current with $U_0 = 0.1$ ms^{-1} that flows over a hill of 200 m height in backgrounds with $N = 10^{-2} - 10^{-3}$ s^{-1} has $Fr_c = 0.05 - 0.5$, e.g. Nikurashin and Ferrari (2010).

Previous studies of atmospheric lee vortices in mountain wakes are relevant. Baroclinic generation, namely, the production of horizontal vorticity by baroclinic torque and its subsequent tilt towards the vertical, appears to be the favored mechanism for lee vortices rather than the vorticity injected by boundary layer separation. This mechanism was proposed by Smolarkiewicz and Rotunno (1989), prompted by their simulation of flow past a bell-shaped hill. Their model, which used a slip BC on all solid boundaries (therefore, no boundary layer), exhibited an attached lee vortex when Fr_c was decreased below ~ 0.5. The flow pattern was similar to that in laboratory experiments at similar Fr_c by Hunt and Snyder (1980). Subsequent work, e.g., Rotunno et al. (1998); Epifanio and Rotunno (2005) has further developed this explanation by analysis of vorticity and potential vorticity (PV) balances. Alternate mechanisms for lee vortices in the case of slip BC have been proposed, e.g., streamline curvature of the boundary flow (Smith, 1989) and dissipative production of PV (Schar and Durran, 1996). No-slip BC has been employed by Ding and Street (2002) and their $Fr_c = 0.2$ simulation conducted at $Re_D = 730$ exhibits a steady attached vortex pair in the lee with little turbulence. Unlike the quasi-steady lee vortex found in several numerical models of the atmospheric hill wake, Schar and Durran (1996); Vosper (2000) report an unsteady vortex street. Laboratory

experiments of stratified flow past obstacles (Hunt and Snyder, 1980; Vosper et al., 1999) report unsteady vortex shedding at Fr_c sufficiently below 1, but the cutoff value of Fr_c varies and is likely sensitive to Re_D, obstacle shape and free-stream disturbances.

In this chapter, we consider a low Froude number of $Fr_c = 0.2$ where predominant horizontal flow is anticipated, along with a relatively steep slope of $h/D = 0.3$, which accentuates flow separation. Since Fr_c is not $\ll 1$, some of the oncoming fluid can go over the obstacle to generate internal waves. Our study examines a model oceanic wake problem in this regime and, rotation effects and tidal forcing are excluded in this paper so as to focus on stratification effects. The literature review shows that stratified oceanic flows in a regime with both internal waves and some upstream blocking and, additionally, at high Rossby numbers have received less attention. We are thus motivated in the present study to examine the sensitivity of a non-rotating wake to various BCs with parameters as described by table 2.2.

2.2 Problem Formulation

2.2.1 Governing equations

$$\frac{\partial u_i}{\partial x_i} = 0, \tag{2.1}$$

$$\frac{\partial u_i}{\partial t} + u_j \frac{\partial u_i}{\partial x_j} = -\frac{1}{\rho_0}\frac{\mathrm{d}p^*}{\mathrm{d}x_i} - \frac{g\rho^*}{\rho_0}\delta_{i3} + \frac{\partial \boldsymbol{\tau}_{ij}}{\partial x_j}, \tag{2.2}$$

$$\frac{\partial \rho}{\partial t} + u_j \frac{\partial \rho}{\partial x_j} = \frac{\partial \boldsymbol{\chi}_j}{\partial x_j}. \tag{2.3}$$

The density field is decomposed as :

$$\rho = \rho_0 + \rho_{bg}(z) + \rho^*(x,y,z,t), \tag{2.4}$$

where ρ_{bg} is a linear function of z, leading to a constant N in the simulations. The large eddy simulation (LES) technique is employed to model the effect of unresolved scales of the flow. Thus, $\boldsymbol{\tau}_{ij}$ and $\boldsymbol{\chi}_j$ include the contribution from both molecular viscosity and the subgrid-scale stress.

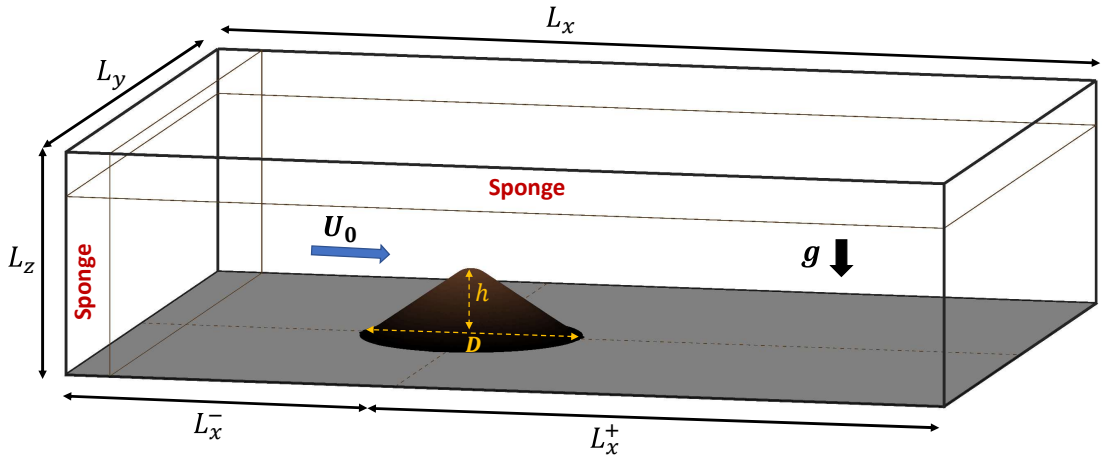

Figure 2.1: Setup of the problem (not to scale): Uniform steady stratified flow encounters a conical obstacle. L_x, L_y and L_z are the streamwise, spanwise and vertical domain sizes. The uniform current U_0 is oriented in the streamwise (x) direction. The obstacle is placed at $x = 0$, with L_x^- being the upstream domain length and L_x^+ being the downstream distance traversed by the flow before reaching the outlet.

2.2.2 Simulated Cases

The setup of the problem is illustrated in fig. 2.1. The flow is initialized with uniform velocity, $\mathbf{u} = (U_0, 0, 0)$, which also serves as the inlet BC. At solid boundaries, the velocity vectors can be decomposed as u_n, u_{t_1} and u_{t_2}, where u_n is the velocity normal to the wall and u_{t_1} & u_{t_2} are the wall-tangential velocities. The BCs are varied among cases. In particular, the

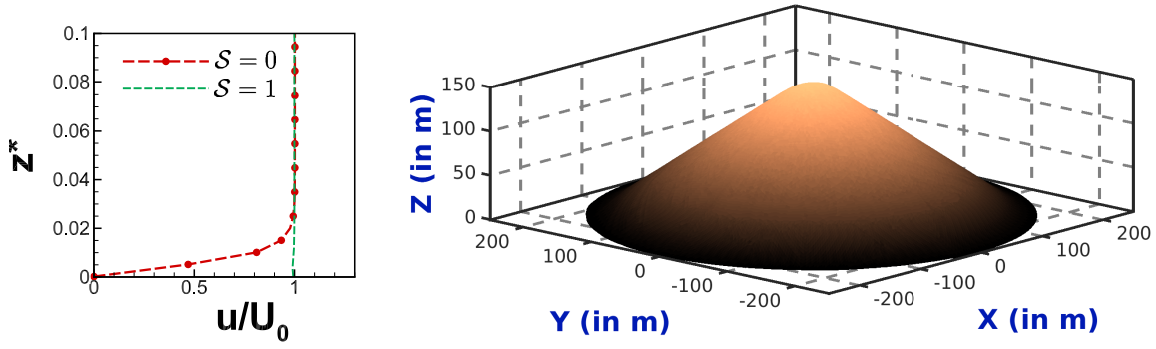

(a) (b)

Figure 2.2: Left : Incoming fluid velocity profile shown for cases with $S = 0$ and $S = 1$ at an upstream location $x^* = -2.4$. Right : Three-dimensional representation of the obstacle.

solid boundaries are either assigned as no-slip walls or slip walls :

$$\text{No-slip wall } (\mathcal{S} = 0): \quad u_n = 0, \quad u_{t_1} = 0, \quad u_{t_2} = 0. \tag{2.5}$$

$$\text{Impermeable slip wall } (\mathcal{S} = 1): \quad u_n = 0, \quad (\boldsymbol{\tau} \cdot \mathbf{n}) \cdot \mathbf{t_1} = 0, \quad (\boldsymbol{\tau} \cdot \mathbf{n}) \cdot \mathbf{t_2} = 0. \tag{2.6}$$

In the above equations, $\mathcal{S}$ is a parameter used to distinguish between a slip wall (where $\mathcal{S} = 1$) and a no-slip wall ($\mathcal{S} = 0$) as shown in eq. (2.6).

2.2.2.1 LES model

Large eddy simulations (LES) are conducted with effects of the unresolved fine scales represented with a subgrid scale (SGS) model. Thus, the viscous stress and density flux vector in eq. (2.1) and eq. (2.3) are computed as :

$$\boldsymbol{\tau}_{ij} = (\nu + \nu_{sgs}) \frac{\partial u_i}{\partial x_j} \quad , \quad \boldsymbol{\chi}_j = (\kappa + \kappa_{sgs}) \frac{\partial \rho}{\partial x_j}. \tag{2.7}$$

Here, ν_{sgs} is estimated using the dynamic eddy viscosity model of Germano et al. (1991) as $\nu_{sgs} = C_s \overline{\Delta}^2 |\overline{S}|$, where $|S| = \sqrt{2 S_{ij} S_{ij}}$. The coefficient C_s is dynamically computed (Lilly,

Table 2.1: Notation used in the model formulation and analysis of results.

x_i	= position vector (x, y, z)
t	= time
u_i	= velocity vector (u, v, w)
(u, v, w)	= streamwise, spanwise and vertical velocity components
(x^*, y^*, z^*)	= $(x/D, y/D, z/h)$
t^*	= tU/D
$\omega_i = \mathcal{E}_{ijk}\frac{\partial u_k}{\partial x_j}$	= vorticity vector $(\omega_x, \omega_y, \omega_z)$
$\omega_i\omega_i$	= enstrophy
$(\omega_x, \omega_y, \omega_z)$	= streamwise, spanwise and vertical components of the vorticity vector
$\mathbf{n}, \mathbf{t_1}, \mathbf{t_2}$	= wall normal vector and two mutually orthogonal tangent vectors
$\rho_{bg}(z)$, ρ_0	= background density profile and reference density (resp.)
ρ, ρ^*	= density and density deviation
$b = -g\rho^*/\rho_0$	= buoyancy
$N = \sqrt{\frac{-g}{\rho_0}\frac{\mathrm{d}\rho}{\mathrm{d}z}}$	= Brunt-Väisälä frequency
p^*	= pressure deviation from hydrostatic
g	= gravitational acceleration
ν	= kinematic viscosity
κ	= thermal diffusivity
τ_{ij}	= stress tensor
χ_i	= density flux vector
$S_{ij} = \frac{1}{2}\left(\frac{\partial u_i}{\partial x_j} + \frac{\partial u_j}{\partial x_i}\right)$	= rate of strain tensor
ν_{sgs}	= subgrid scale eddy viscosity
κ_{sgs}	= subgrid scale eddy diffusivity
$\overline{A}$	= LES filter applied to A
Δ	= LES filter length
C_s	= Smagorinsky coefficient

1992). The customary smoothing of C_s is performed in this problem with Lagrangian averaging (Meneveau et al., 1996) along particle trajectories using an exponential weighting function. Lagrangian averaging is effective in flows which do not have a homogeneous spatial direction to implement smoothing. In all simulations, the subgrid Prandtl number ($Pr_{sgs} = \nu_{sgs}/\kappa_{sgs}$) is fixed as unity.

The mean value (Reynolds average) of any field variable is obtained by averaging in time after the initial transient has subsided. The mean value of the parameter ϕ is denoted by $\langle\phi\rangle$, and the fluctuating field becomes $\phi' = \phi - \langle\phi\rangle$. The turbulent kinetic energy is denoted by

Table 2.2: Simulation parameters for different cases in this study. The streamwise domain size (split into values, upstream and downstream of the obstacle) is as given in the table, and the other domain sizes (L_y and L_z) are fixed at $6D$ and $20h$, respectively, for all cases. The grid sizes in the corresponding directions are N_x, N_y and N_z. The slip parameter $\mathcal{S}$ is either 0 or 1. The Reynolds number (Re_D) for all cases is 15,000.

Case	L_x^-	L_x^+	N_x	N_y	N_z	Fr_c	Description
NOSL	3D	14D	1280	1024	430	0.2	No-slip ($\mathcal{S}=0$) BC everywhere
SL	8D	14D	1536	1024	400	0.2	Slip ($\mathcal{S}=1$) BC everywhere
Hybrid	8D	14D	1536	1024	400	0.2	$\mathcal{S}=0$ on obstacle & $\mathcal{S}=1$ on bottom wall
SL-UN	8D	14D	1536	1024	400	Inf	Unstratified & Slip ($\mathcal{S}=1$) BC everywhere
DL	8D	14D	1536	1024	400	0.2	Quadratic drag law BC everywhere

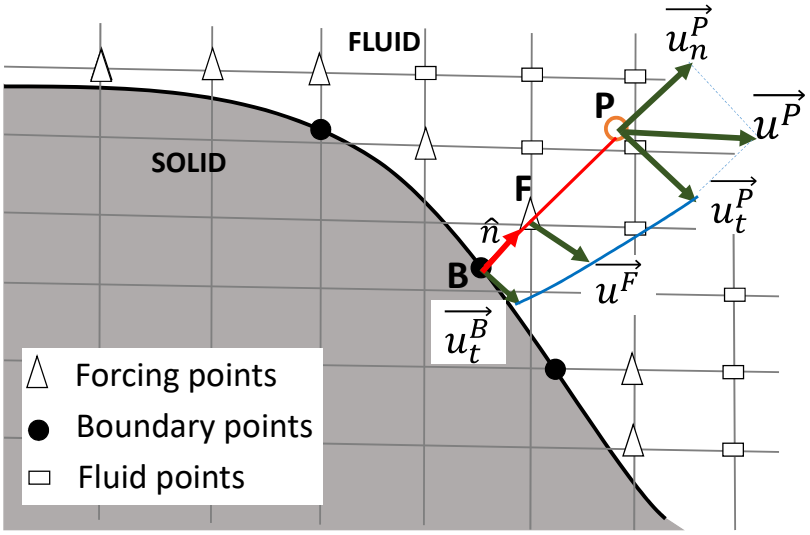

Figure 2.3: Generalized interpolation stencil used in IBM for implementing the appropriate BC on the forcing points. Here, **B** is the boundary point, **F** represents the forcing point and **P** is the interpolation point. **BF** line segment is normal to the fluid-solid interface (dark black line).

$K = \langle u_i' u_i' \rangle / 2$

2.3 Flow velocity

2.3.1 Streamlines

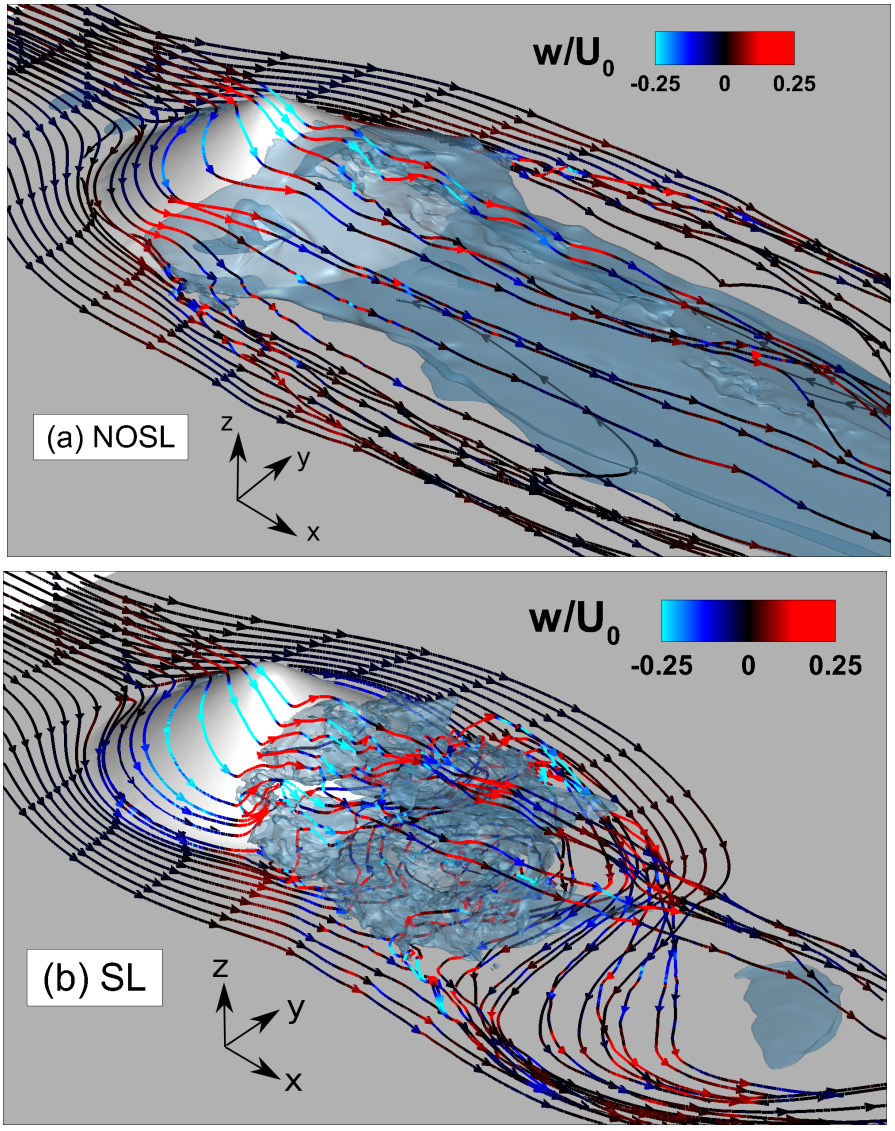

Figure 2.4: Instantaneous streamlines which originate from upstream are plotted at $t^* = 100$: (a) **NOSL** and (b) **SL**. The streamlines are colored with the vertical velocity. The silver blue colour represents the isosurface $u = 0$, which demarcates the recirculation zone behind the obstacle upto $x^* = 2.2$ downstream.

Figure 2.4 shows instantaneous streamlines in **NOSL** and **SL**. These streamlines originate upstream of the body and are colored with the vertical velocity (w) value. One set

of streamlines originates from a vertical line ($y^* = -0.01$ and $x^* = -0.6$) located centrally and upstream. Some of the upper streamlines in this set (those that originate above z_s) have sufficient positive (red) w to surmount the obstacle after which they slope downward to follow a downslope jet. The subsequent oscillation of these streamlines is indicative of a lee wave. Streamlines that originate below z_s on the vertical line are unable to surmount the obstacle and their lateral (sideways) deflection can be seen as they negotiate the obstacle. Another set of streamlines in fig. 2.4 originates from a spanwise-oriented upstream line located at $z^* = 0.066$ (a height below z_s) and $x^* = -0.6$. These streamlines illustrate the downward and lateral motion of fluid that originates from the blocked region. The isosurface of $u = 0$ is plotted in silver blue and serves to demarcate the recirculation zone.

Flow separation in **NOSL** has a pattern that is distinct from **SL**, although both cases exhibit upstream blocking. Fluid in **NOSL** experiences viscous drag and, owing to the larger reduction of flow speed, separates earlier relative to **SL**. The streamlines in **SL** show that the fluid is able to navigate around the obstacle curvature for a longer distance and curve inward before eventual separation. Consequently, the separation line, which is the intersection of the $u = 0$ isosurface in silver blue with the obstacle, has a smaller lateral size in **SL**.

The post-separation flow is strikingly different between **NOSL** and **SL**. The recirculation region is significantly shorter in **SL**. The small-scale corrugations in the $u = 0$ isosurface and the rapid changes in the direction of w along streamlines indicate that the near wake in **SL** has stronger turbulence than **NOSL**. Figure 2.4 (b) shows that some of the streamlines adjacent to the bottom exhibit large lateral excursion around the recirculation region. These excursions illustrate unsteady, large-amplitude lateral meanders of fluid in the wake that are prominent in **SL** and absent in **NOSL**.

2.3.2 Mean velocity

To investigate the influence of the BC on the flow statistics, we examine the mean streamwise and vertical velocity fields, shown in fig. 2.5. Initially, the flow in the downstream wake is allowed to become statistically steady. The equilibrium time needed to attain this state is estimated to be $70D/U_0$. After $t^* = 70D/U_0$, statistics are recorded and the temporal average is performed over a time span of $\Delta t = 40D/U_0$. Comparison among fig. 2.5(a-d) shows that the recirculation bubble in the lee of the obstacle is largest in **NOSL**, followed by **DL** & **Hybrid** and then **SL**. The unblocked layer of fluid, which is able to traverse the obstacle vertically, generates steady lee waves with phase lines that are prominent in the vertical velocity contours of fig. 2.5(e-h). The lee waves far away from the obstacle (beyond $x^* = 2.5$) are similar in the centerplane ($y^* = 0$) among the three cases. However the lee-wave near field is different in **NOSL** (fig. 2.5 e) relative to the other cases. Here, the larger recirculation zone does not allow the lee waves to penetrate into a substantial portion of the near wake. However, in **SL**, **DL** and **Hybrid**, the lee-wave phase lines in fig. 2.5 (f-h) that are downstream of $x^* = 2$ (end of the recirculation region), extend close to the flat bottom.

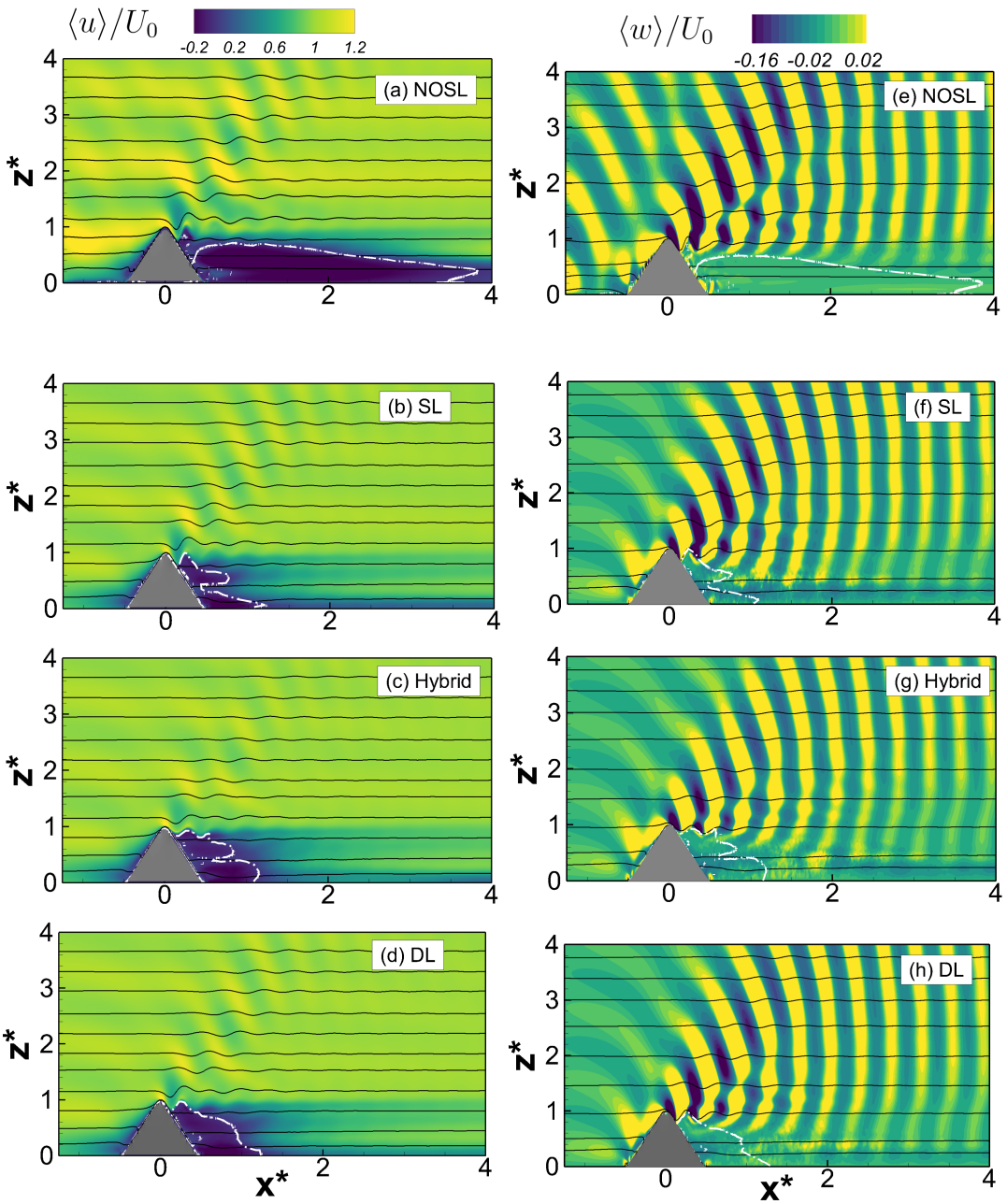

Figure 2.5: Mean streamwise velocity (a-d) and vertical velocity (e-h) in the centreplane ($y^* = 0$): The four cases - **NOSL** (first row), **SL** (second-row) , **Hybrid** (third row) and **DL** (fourth row) show substantial differences in the size of the recirculation region of the wake (a-d) and the penetration of the internal waves into the wake (e-h) at the same Re_D and Fr_c. Note that the aspect ratio is changed for better visualization. The dotted white line denotes the $u = 0$ contour.

Although the **Hybrid** and **DL** cases exhibit a slightly larger recirculation zone downstream, the wake in these cases is qualitatively similar to **SL**. Therefore, the comparison in subsequent sections will be primarily between cases **SL** and **NOSL**.

2.3.3 Velocity Spectra

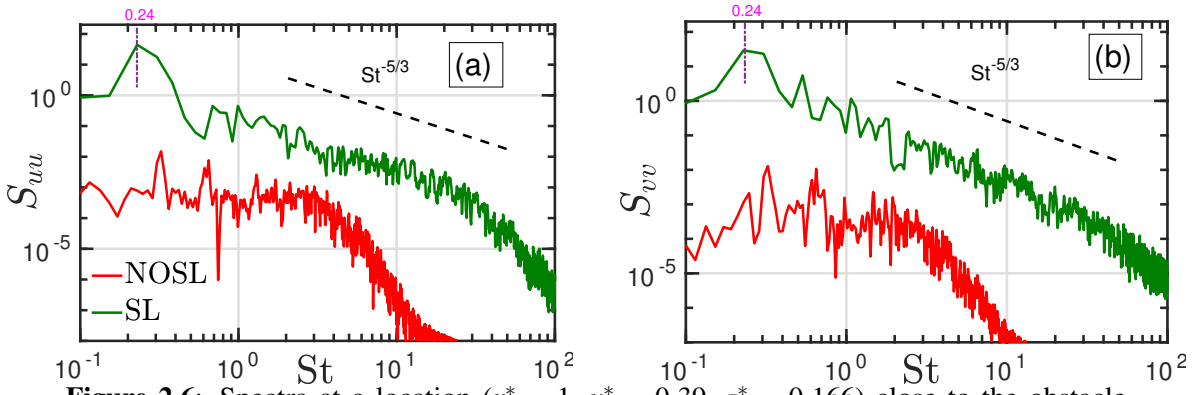

Figure 2.6: Spectra at a location ($x^* = 1$, $y^* = 0.39$, $z^* = 0.166$) close to the obstacle compared between **NOSL** and **SL** cases: (a) streamwise velocity (S_{uu}), and (b) spanwise velocity S_{vv}.

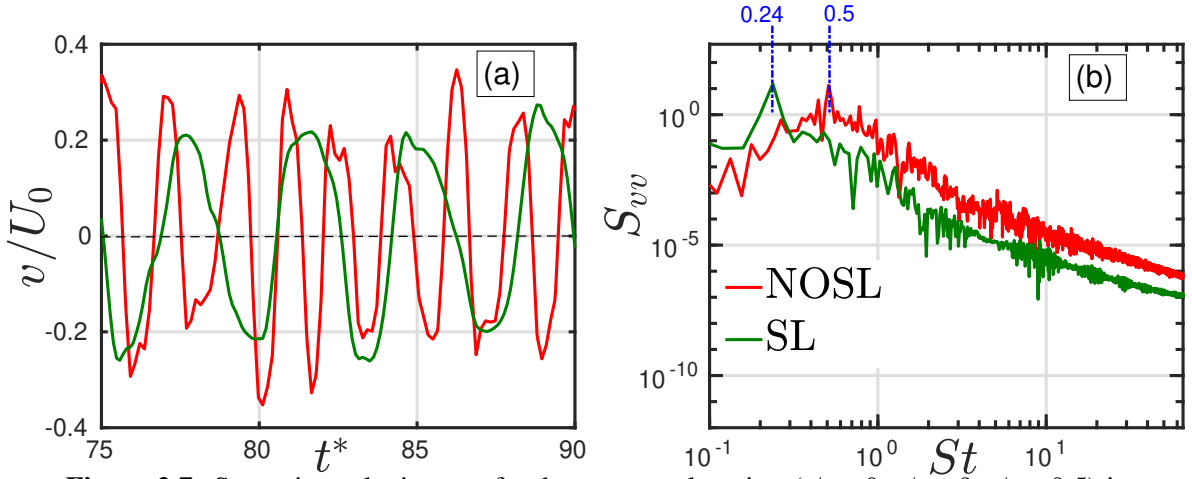

Figure 2.7: Spanwise velocity at a far downstream location ($y^* = 0$, $x^* = 9$, $z^* = 0.5$) is contrasted between **NOSL** and **SL** cases: (a) time history, and (b) corresponding velocity spectra. At this downstream location, the turbulent fluctuations in the flow have diminished leaving behind a clear signature of the instabilities of the velocity profile of a quasi-two dimensional wake.

In Figure 2.6, the spectra of streamwise (u) and spanwise (v) velocity are plotted at a

downstream location ($x^* = 1$, $y^* = 0.39$ and $z^* = 0.166$) close to the obstacle. Case **SL** shows a broadband spectrum with a wide separation of time scales in the flow, indicative of a fully turbulent flow. In contrast, the amplitude of the spectrum in **NOSL** is smaller by a factor of 10^3 and, furthermore, spans a narrower range of frequencies. The amplitude of S_{uu} and S_{vv} are comparable in **SL**. Both S_{uu} and S_{vv} in **SL** reveal a discrete peak at $St = St_c = 0.24$ which corresponds to the shedding frequency of the lee vortices off the obstacle. The observed $St = 0.24$ is close to the estimate of $St = 0.264$ computed from the $St - Re_D$ relationship proposed by Williamson and Brown (1998) for cylinder wakes. There is no such periodic component in **NOSL** at this location.

Moving to a further downstream location, we find a periodic signal in both components of horizontal velocity and a corresponding spectral peak in both **SL** and **NOSL**. This temporal periodicity is illustrated by Figure 2.7(a) for the v component at a downstream location: $x^* = 9, y^* = 0$ and $z^* = 0.5$. In **NOSL**, the spectral peak of v at this location is at $St = 0.5$, and corresponds to the barotropic sinuous instability of the quasi-two-dimensional wake (Lesieur, 2008). The barotropic instability of wakes and jets takes the form of a sinuous mode that evolves into two staggered rows of vortices of opposite sign (Maslowe, 1991; Perret et al., 2011) and, under forcing, also a varicose mode with two non-staggered vortex rows. The frequency of this instability in **NOSL** is found to vary with height so that St takes values between 0.4 and 0.8. However for case **SL**, the vortex shedding frequency does not change with height.

2.3.4 Turbulent kinetic energy

To quantify the influence of BCs on the wake turbulence, snapshots of TKE are shown in the central vertical plane ($y^* = 0$) in fig. 2.8. Additionally, mean velocity vectors are shown at selected streamwise locations to illustrate the overall flow structure. In **NOSL**, there is strong bottom shear in the recirculation region. However, the bottom boundary layer is quasi-

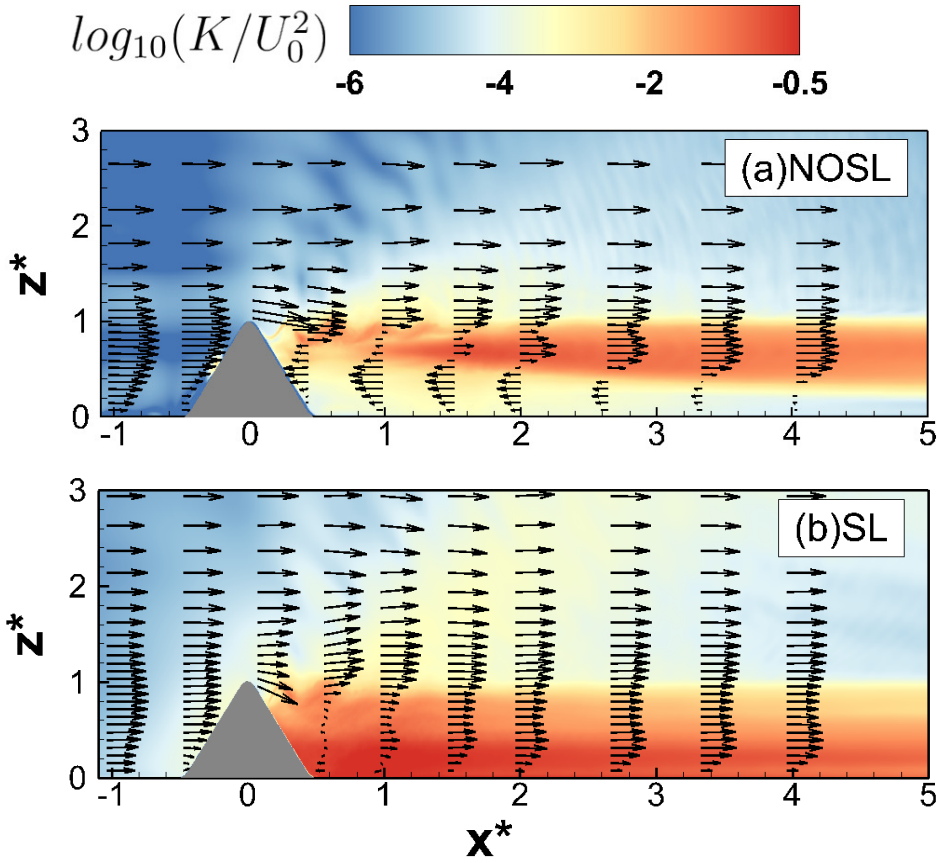

Figure 2.8: Spatial organization of turbulent kinetic energy ($K = \langle u_i' u_i' \rangle / 2$) normalized by U_0^2 in the vertical plane $y^* = 0$: (a) **NOSL**, and (b) **SL**. Vectors representing the mean velocity field are also shown at selected cross-sections.

laminar at this moderate *Re* and, furthermore, bottom friction restricts the lateral meander of the wake that would generate turbulent fluctuations. Therefore, in the near-bottom region of $0 < z^* < 0.2$, **NOSL** exhibits small TKE. In the upper region, a shear layer forms at the boundary of the recirculation zone with the downslope jet and lee wave to support turbulent fluctuations, shown by a zone of enhanced TKE (fig. 2.8a), which spreads vertically with increasing x^*. These fluctuations also trigger instability of the horizontal shear in the wake to eventually allow the spanwise oscillation (fig. 2.7) which is seen further downstream. In **SL**, the recirculation zone is small. The slip BC allows near-bottom lateral meanders close to the body as well as broadband fluctuations which are reflected in the high TKE content of the

flow in the lee of the obstacle. Unlike **NOSL**, a strong upper shear layer does not develop and the TKE is bottom-intensified.

2.4 Vortex Dynamics

2.4.1 Lee wake vortices

The organization of vertical vorticity (ω_z) in **NOSL** is strikingly different from **SL, DL** and **Hybrid** cases, while the latter three cases resemble each other. Figure 2.9 illustrates the difference by showing ω_z contours on horizontal planes at four different heights in the wake.

In **NOSL** (fig. 2.9a), there is a pair of counter-rotating vortices at $z^* = 0.066$ close to the bottom. These lee vortices are found to be steady in time and take the form of an attached recirculation bubble. The presentation of these vortices resembles the lee vortex pair found near the bottom in the laboratory experiment of Hunt and Snyder (1980) and also in aerial observations by Smith and Grubisic (1993) of the wake of Hawaii. At the somewhat higher location of $z^* = 0.33$ too, there is a steady recirculation bubble. However, at the even higher location of $z^* = 0.66$, the recirculation bubble, while remaining attached, displays unsteadiness at its tail end, and coherent lee vortices appear further downstream. The size of the lee vortices at a given height is proportional to the local diameter ($d(z)$) of the conical obstacle. This large-scale unsteadiness, observed further downstream, sets in at heights above $z^* = 0.2$ through barotropic sinuous instability (Lesieur, 2008) of the velocity profile of a quasi-two-dimensional wake that develops into coherent vortices.

In contrast, the bottom slip wall in **SL** allows unsteady shedding of alternating opposite-signed Kármán vortices from the obstacle. Their instantaneous presentation is qualitatively different from **NOSL**, as can be seen by comparing the $z^* = 0.066$ and 0.33 planes (fig. 2.9b) to the corresponding planes in **NOSL** (fig. 2.9a). The shedding of Kármán vortices from

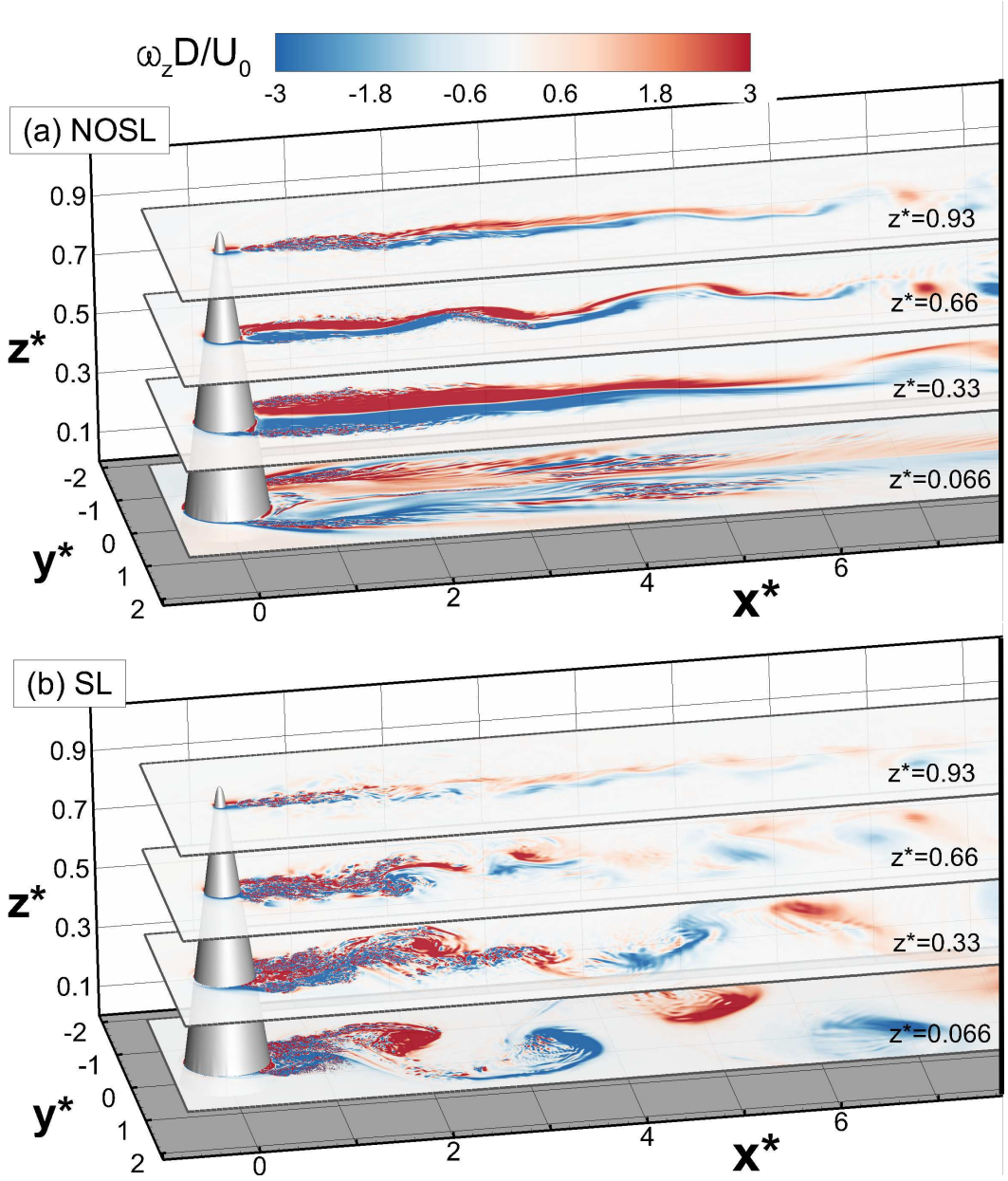

Figure 2.9: The organization of the lee vortices is affected by the boundary conditions. Lee vortices are shown by contours of normalized vertical vorticity (ω_z) at $t^* = 100$: (a) **NOSL**, and (b) **SL**

the body leads to lateral flapping of the wake which is manifested by the lateral meanders in the streamlines and the oscillation of the centerline lateral velocity which were described previously. At $z^* = 0.93$, the lee waves interfere strongly with the coherent structures in the wake, thereby disturbing the vortex street.

To summarize, lee vortices form behind the obstacle, independent of the BC. Furthermore, their lateral size at a given height is proportional to the local diameter of the obstacle. The critical difference introduced by the type of BC is that the lee vortices in **SL** are shed off the body unsteadily to result in a Kármán vortex street while, in **NOSL** there is a quasi-steady, attached vortex pair.

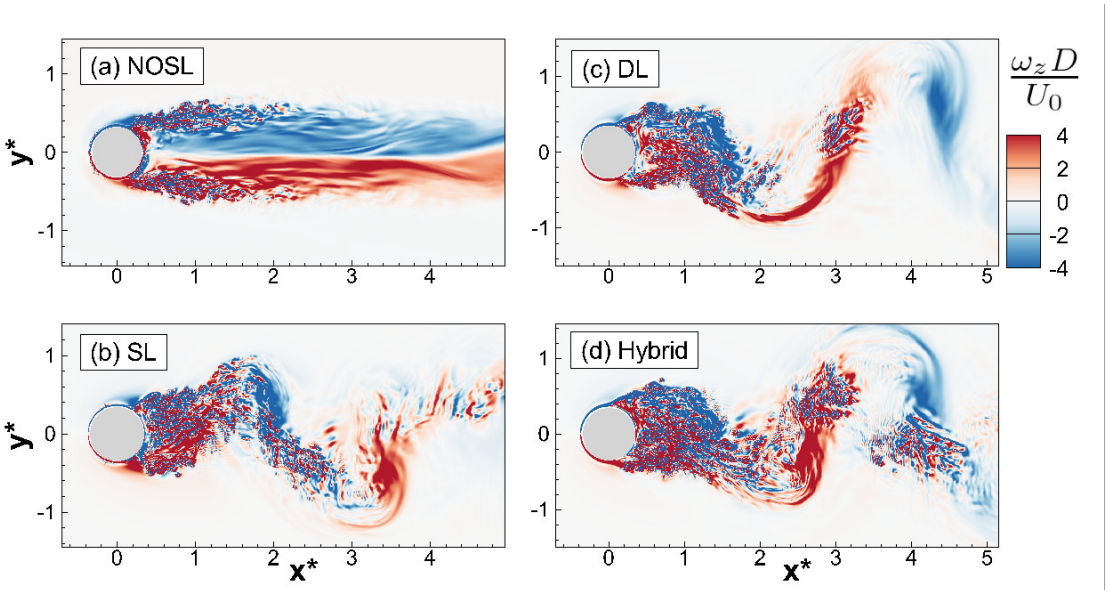

Figure 2.10: Spatial organization of vertical vorticity ω_z in the horizontal plane $z^* = 0.25$ at time $t^* = 75.8$: (a) **NOSL**, (b)**SL**, (c) **DL**, and (d)**Hybrid**.

The results of previous sections on the mean velocity show that the behavior of **DL** resembles **SL** and **Hybrid**. Figure 2.10(c) depicts contours of ω_z in the horizontal plane $z^* = 0.25$ in the drag-law case. The corresponding ω_z contours for the other BCs , which are included for comparison in fig. 2.10, demonstrate that **DL**, **Hybrid** and **SL** cases are qualitatively similar in terms of vortex dynamics.

2.4.2 Unstratified wake

We have seen that, for all BCs considered here, there are coherent wake vortices in low-Fr_c flow past a conical obstacle, and they take the form of unsteady Kármán vortices, shed from the body, in the **SL** case. Both body curvature and baroclinicity have been advanced

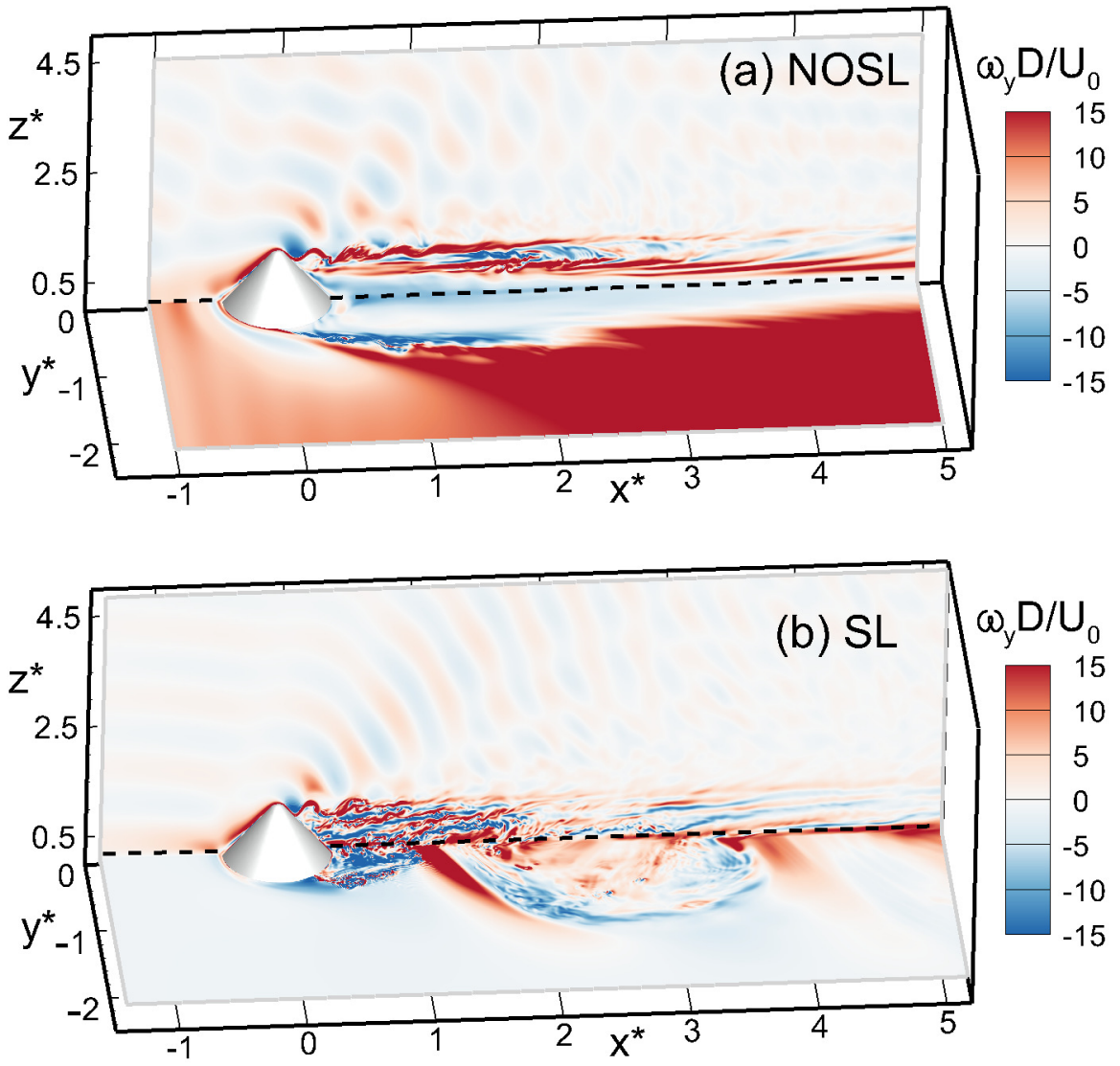

Figure 2.11: Comparison of spanwise vorticity (ω_y) between cases with different BCs: (a) **NOSL** and (b) **SL**. Instantaneous contours of ω_y are depicted on a vertical plane ($y^* = 0$) and a horizontal plane ($z^* = 0.13$). The black dotted line represents the intersection between the vertical and the horizontal plane.

in the past as potential origins of the wake vorticity. To exclude the effect of baroclinicity, an unstratified counterpart (**SL-UN**) has been simulated with the slip BC. Vorticity can be induced by solely body curvature, and is proportional to the tangential slip velocity of the flow at the obstacle (Leal, 1989; Legendre et al., 2009). To demonstrate curvature-

induced vorticity, consider free-slip flow past a circular shear-free cylinder of radius a in polar coordinates (r,θ). Since $u_r = 0$ and $\tau_{r\theta} = 0$ at $r = a$, it follows that $\partial u_\theta/\partial r = u_\theta/a$ and $\omega_z = (\partial u_\theta/\partial r + u_\theta/r)_{r=a} = 2u_\theta/a$. Here, u_θ represents the surface tangential velocity. As elaborated below, the unstratified counterpart is qualitatively different from the stratified cases. In particular, although curvature alone does give rise to vorticity, lee vortices with size comparable to the body do not form in the wake.

Figure 2.12(a) shows that, for case **SL-UN**, flow separation in the vertical centerplane ($y^* = 0$) occurs at $x^* = 0.35$ and $z^* = 0.3$. This is in contrast to the near-apex separation in the corresponding stratified case **SL** (left column of fig. 2.5). Figure 2.12(b) shows that separation is also delayed in the horizontal ($z^* = 0.066$) plane where it occurs close to the rear stagnation point. The flow remains attached to the sloping and curved geometry in **SL-UN** for a long distance before separation because of the following reasons: (a) absence of viscous loss of momentum at the boundary, and (b) lack of a lee wave and its imposition of an adverse pressure gradient on the boundary flow. It is worth noting that, in previous work on unstratified flow past a 3D obstacle with a no-slip BC, e.g. Garcia-Villalbaa et al. (2009), flow separation at the obstacle occurs substantially upstream relative to **SL-UN** and there is a large recirculation zone followed by a turbulent wake. The recirculating flow at the junction of the bottom and central lee of the obstacle generates a narrow wake that develops a sinuous instability in the horizontal plane. Figure 2.12(b) and (c) show the streamwise and spanwise velocity, respectively, in a horizontal plane $z^* = 0.066$. Here, this narrow region of attached low-velocity fluid in the lee can be noticed along with the subsequent sinuous instability.

The three components of vorticity are shown in fig. 2.12(d-f) on a horizontal plane. The location of the plane at $z^* = 0.066$ is sufficiently below the apex so as to include the separated flow in the lee of the obstacle. There is vertical vorticity at the body in fig. 2.12(d) owing to its curvature in the horizontal plane. However, the wake behind the body is narrow and does not exhibit the large lee vortices seen in the stratified cases. This observation confirms

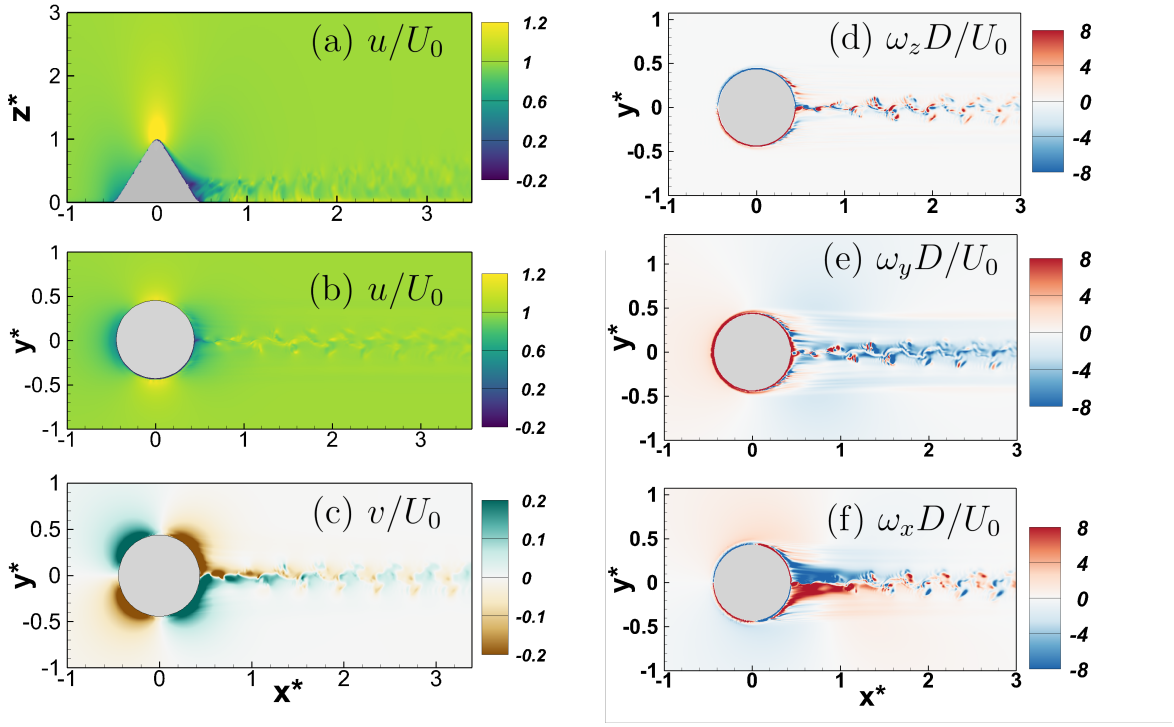

Figure 2.12: Flow in case **SL-UN** is shown at $t^* = 101$. Left column shows normalized velocity components on different planes: (a) streamwise velocity on the vertical centerplane, ($y^* = 0$), (b) streamwise velocity on a horizontal plane ($z^* = 0.066$), and (c) lateral velocity on the same horizontal plane shown in (b). Right column shows normalized vorticity components on this horizontal plane, $z^* = 0.066$: (d) vertical vorticity, (e) spanwise vorticity and (f) streamwise vorticity.

that curvature alone, without baroclinicity, is insufficient for the emergence of large lee wake vortices that have been observed in geophysical flows.

2.4.3 Sources of vorticity

The vorticity transport equation, obtained by employing the curl operator on eq. (2.2), is as follows:

$$\frac{\partial \omega_i}{\partial t} + u_j \frac{\partial \omega_i}{\partial x_j} = \omega_j \frac{\partial u_i}{\partial x_j} + \mathcal{E}_{ij3} \frac{\partial b}{\partial x_j} + \nu \frac{\partial^2 \omega_i}{\partial x_j^2} + \mathcal{E}_{ikm} \frac{\partial}{\partial x_k} \left[\frac{\partial}{\partial x_j} \left(\nu_{sgs} \frac{\partial u_m}{\partial x_j} \right) \right] . \tag{2.8}$$

On the right hand side (r.h.s.) of Eq. (2.8), the first term represents vortex stretching/tilting and the second term is the baroclinic torque. The third and fourth terms are molecular diffusion and the modeled subgrid diffusion, respectively; both are lumped together into a single diffusion term in the results.

Figure 2.13 shows the streamwise evolution of $y-z$ plane-integrated values of enstrophy components (ω_x^2, ω_y^2 and ω_z^2) in fig. 2.13(1a-c), vortex stretching in fig. 2.13(2a-c), vortex tilting in fig. 2.13(3a-c), diffusion term (includes viscous diffusion and the contribution from eddy diffusivity) in fig. 2.13(4a-c), and baroclinic torque in fig. 2.13(5a-b). In row 3 of fig. 2.13, the vortex tilting term (t_x, t_y, t_z) is shown for each vorticity-component equation, for example, t_z denotes the vortex tilting term in the ω_z equation computed as $\omega_x \partial w/\partial x + \omega_y \partial w/\partial y$. Similarly, in row 4 of fig. 2.13, the diffusion term (d_x, d_y, d_z) is shown for each vorticity-component equation. The absolute value of each term in the vorticity equation is taken before computing the area integral. This allows estimation of their relative importance; the sign does not matter for this analysis. In **SL-UN**, the enstrophy components are limited to the obstacle with negligible values in the lee. Fluid can flow over the obstacle since stratification, which diverts oncoming fluid sideways around the obstacle, is absent. Hence, the spanwise vorticity (ω_y) is much larger than ω_z. The component, ω_x, is generated by tilting of ω_y and ω_z. Owing to viscous dissipation, the magnitude of each vorticity component decreases eventually.

The **SL** case is strikingly different from **SL-UN** although the same boundary conditions are in play. Each vorticity component increases in magnitude from its upstream zero value as the fluid flows past the obstacle. Figure 2.13(1a) shows that that there is significant enstrophy in both horizontal components, not just ω_y. Baroclinic torque (absent in **SL-UN**) is a source of both horizontal components and, as shown by fig. 2.13(5a), it exceeds other sources of vorticity. Note, that the range of the vertical axis is larger for row 5 (baroclinic torque), relative to the rows showing the other sources. The vortex tilting term (t_z) and vortex stretching term ($\omega_z \partial w/\partial z$) in rows 3 and 2 of fig. 2.13(a), respectively, are also substantial. Thus, the

simulations demonstrate that baroclinic torque produces horizontal vorticity which is tilted and stretched to give ω_z, in accord with the lee-vortex mechanism proposed by Smolarkiewicz and Rotunno (1989). Vortex tilting reduces in magnitude with increasing downstream distance, which lowers the magnitude of ω_z relative to the other components as shown in fig. 2.13(1a). Furthermore, the vortex tilt/stretch terms are isotropic with no directional preference for any particular component suggesting that these terms are operative at smaller scales of motion.

Baroclinic torque generated by density anomalies in the horizontal is also dominant in **NOSL** shown in fig. 2.13(5b). However, unlike **SL**, the magnitude of ω_y far exceeds the other components as seen in fig. 2.13 (1b). The reason is that the bottom boundary boundary layer, which injects spanwise vorticity into the flow, persists over the entire streamwise extent, while the wake vorticity, which is the primary source of the other vorticity components, is dissipated by viscosity.

2.5 Summary and Discussion

Four numerical simulations are performed, with focus on two main cases, namely **NOSL** (no-slip BC used across all boundaries) and **SL** (slip BC used on all boundaries). The other two cases are described as follows : case **Hybrid**, undertaken with slip flat bottom and no-slip obstacle and case **DL** wherein a quadratic drag-law BC is adopted on all boundaries. The no-slip BC allows the formation of a boundary layer which separates and sheds vorticity into the wake. Significant changes occur in the structure of the lee vortices and wake when the BC is changed. For instance, wall friction in the no-slip case suppresses unsteadiness of flow separation leading to a steady attached lee vortex. In contrast, when the bottom wall is made shear-free, unsteady separation leads to a vortex street in the near wake and the enhancement of turbulence. The recirculation region is shorter and the wake recovery is substantially faster in the case of slip BC. Turbulent kinetic energy (TKE) in the lee is bottom intensified in

the case of slip BC while, for the no-slip BC, it is concentrated in a shear layer between the recirculating wake and the free stream. The sources of lee vorticity are also examined in this study for each choice of BC. The sloping sides lead to horizontal gradients of density at the obstacle, which create vorticity through baroclinic torque. Independent of the type of BC, the baroclinic torque dominates. Vortex stretch and tilt are also substantial. An additional unstratified ~~case~~ free-slip case (**SL-UN**) is simulated and the wake is found to be thin without large wake vortices. Thus, stratification is necessary for the formation of coherent lee vortices of the type seen in geophysical wakes. A drag law is often employed in numerical models of geophysical flows that do not resolve the boundary layer. Application of a quadratic drag law (analogous to partial slip) leads to wake dynamics qualitatively similar to that found for the slip BC.

Both no-slip and slip BCs have been employed in past studies of stratified flow past an isolated obstacle. No-slip is the physically correct BC. However, when the computational grid is too coarse to resolve the physical boundary layer, application of the no-slip BC results in an incorrect numerical boundary layer. As an alternative, geophysical wakes at high Reynolds number have been simulated with a slip BC or by the imposition of a drag law which can be viewed as a partial-slip boundary condition.

The stratified flow at $Fr_c = 0.2$ exhibits flow blocking upstream of the obstacle, streamlines that are diverted to go around rather than over the obstacle, an accelerated downslope jet, flow separation followed by recirculation, a lee wave, and wake vortices with organized ω_z in the lee. Many of these flow features are substantially altered by the type of BC. Notably, the lee vortices in **NOSL** take the form of an attached counter-rotating vortex pair with little unsteadiness in most of the recirculation region behind the body while, in **SL**, **DL** and **Hybrid**, counter-rotating vortices are shed off the body to form a Kármán vortex street. **SL**, **DL** and **Hybrid** exhibit lateral flapping of the wake which periodically transports fluid with higher streamwise momentum to the centerline and, consequently, the mean value of centerline defect

velocity decreases substantially faster in the near wake relative to **NOSL**. At the selected $Re_D = 15,000$, bottom friction evidently exerts a strong constraint on the wake that reduces unsteadiness near the body in **NOSL**. It is only further downstream (x/D of this location increases with increasing depth) that the wake develops a sinuous barotropic instability.

The lee wake vortices show vertical variability in size. Independent of the BC, their horizontal size is proportional to the local diameter ($d(z)$) of the conical obstacle. The frequency of the vortex shedding that occurs in **SL**, **DL** and **Hybrid** does not vary with vertical location in the simulated cases. Spectra of streamwise (u) and lateral velocity (v) in the near-wake region of **SL** show discrete peaks at the vortex shedding mode, quantified as $St = fD/U \approx 0.24$. Although there is no discrete peak in the near-wake region of **NOSL**, farther downstream there is a peak in the v-spectrum at $St = fD/U \approx 0.5$ which is visually apparent as a sinuous instability of the wake in the horizontal plane.

The boundary layers on the flat and sloping bottom are resolved in **NOSL**. Therefore, a laboratory experiment conducted with the present obstacle geometry and $Re_D = 15,000$ and $Fr_c = 0.2$ would be expected to match the results of **NOSL** and not **SL**, **DL** or **Hybrid**. Indeed, for similar parameters of $Fr_c = 0.2$ and $Re_D = 13,700$, Hunt and Snyder (1980) report a quasi-steady recirculation zone containing an attached counter-rotating vortex pair with some irregular unsteadiness in the wake.

At the moderate Re of the present simulations, the boundary layer is laminar and it imposes a wall shear (τ_w) that is steady in time and has a drag coefficient of ≈ 0.02. Geophysical flows are at high Re with a turbulent boundary layer and a lower C_D, and a drag-law BC is often used to represent the boundary layer. The **DL** case in our study is undertaken with $C_D = 0.0025$, and gives results similar to **SL** and **Hybrid**.

Boundary-layer vorticity, curvature of the body and baroclinicity have been advanced as potential generators of the lee wake vortices. An unstratified simulation (**SL-UN**) is conducted to rule out baroclinicity as a generator of vorticity. In **SL-UN**, the flow remains

attached over a much larger region, the wake that emerges is narrow, and large organized lee vortices are absent. Unstratified simulations with no-slip BC have not been conducted here, since there are prior laboratory experiments and simulations with the no-slip BC of the unstratified configuration. The prior studies show vortical structures different from the present lee vortices: a standing horseshoe vortex and periodic shedding of hairpin vortices at low Re_D (Acarlar and Smith, 1987) which changes to intermittent shedding of vortex patches at high Re_D (Garcia-Villalbaa et al., 2009). Therefore, we conclude that, independent of the choice of BC, unstratified flow does not demonstrate lee wake vortices of the type observed in geophysical wakes or in stratified-flow laboratory models of said wakes.

All components of the vorticity are prevalent in the flow as shown by the streamwise evolution of the squared magnitude (enstrophy) of each vorticity component. Owing to BL vorticity, the spanwise vorticity (ω_y) dominates the other two components upstream and downstream of the hill in the no-slip case. However, the increase in vorticity at the obstacle is similar among the different BCs. Instantaneous streamlines shows opposite-signed vertical motion in the aft and lee as the fluid moves past the obstacle leading to the horizontal density gradients which are necessary for the baroclinic torque to be operative in the vorticity balance. Sources in the equation for each vorticity component are quantified and it is found that the baroclinic torque (operative only in the balances for horizontal vorticity components) is dominant, independent of the BC type. Vortex stretch and tilt are also substantial. The simulation result, namely, that horizontal vorticity is produced by the baroclinic torque and tilted into the vertical, supports the lee-vortex mechanism proposed by Smolarkiewicz and Rotunno (1989).

Turbulence is quantified through the TKE. The lateral meanders of the wake in **SL** lead to high TKE in the wake. In **NOSL**, there is a zone of TKE that originates in the vertical shear layer between the fluid in the recirculation zone and the flow above associated with the lee wave and the separating downslope jet.

Acknowledgements

This chapter, in full, is a reprint of the material as it appears in “The wake of a three-dimensional underwater obstacle: effect of bottom boundary conditions”, P. Puthan, M. Jalali, J. L. Ortiz-Tarin, K. Chongsiripinyo, G. Pawlak and S. Sarkar, *Ocean Modeling*, 149, 2020. The dissertation author is the primary investigator and author of this paper.

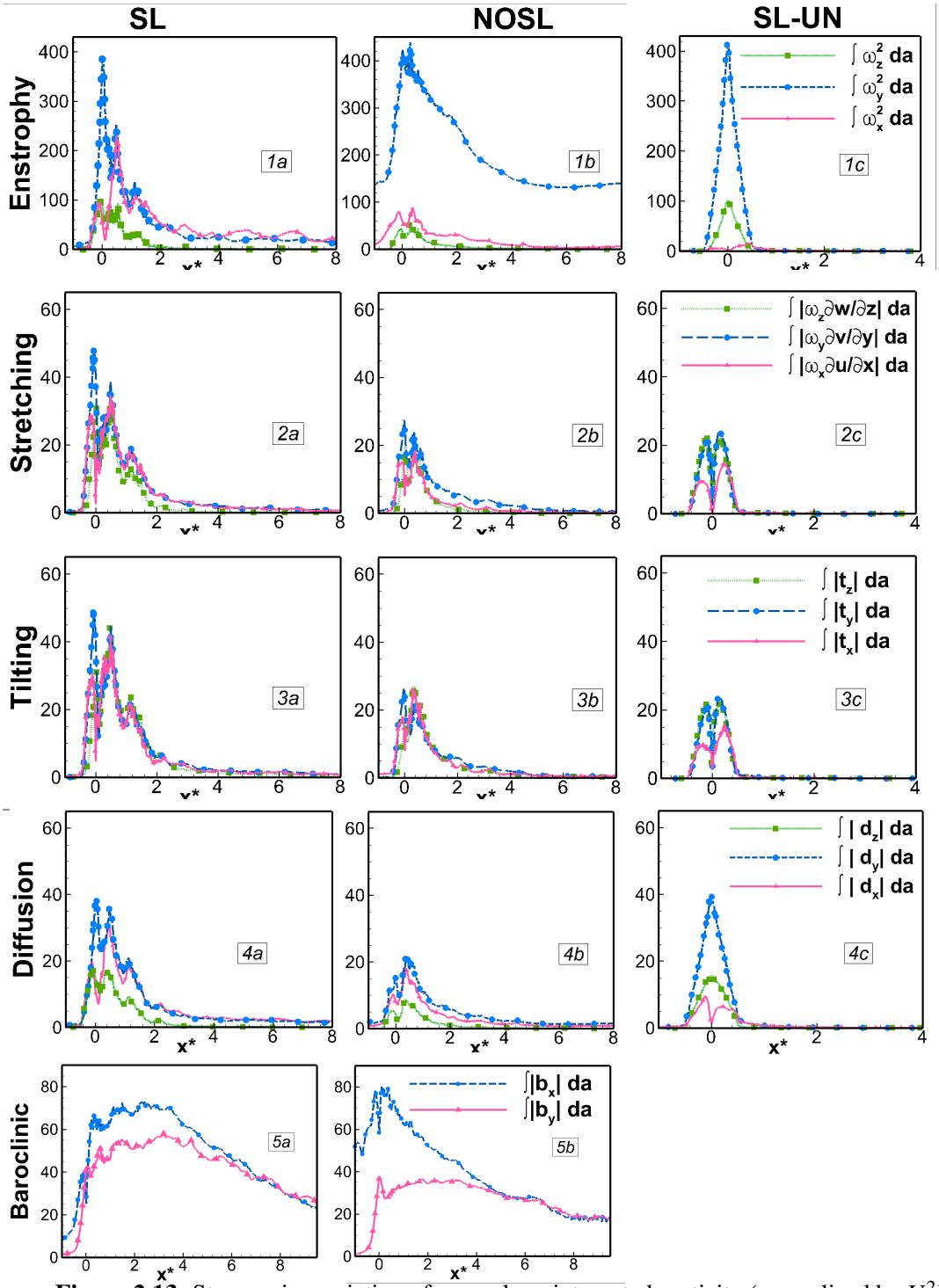

Figure 2.13: Streamwise variation of $y-z$ plane-integrated vorticity (normalized by U_0^2) and vorticity budget terms represented in eq. (2.8) (also normalized by U_0^2) at $t^* = 101$. Columns are (a) **SL**, (b) **NOSL**, and (c) **SL-UN**. Row 1 (top) shows the three components of squared vorticity (enstrophy). Row 2 shows the vortex stretching term, row 3 the vortex tilting term, row 4 the lumped diffusion term, and row 5 the baroclinic torque. In each figure of rows 2-5, terms in the ω_x, ω_y and ω_z equations are represented by green, blue and pink lines, respectively.

Chapter 3

Tidal synchronization of lee vortices in geophysical wakes

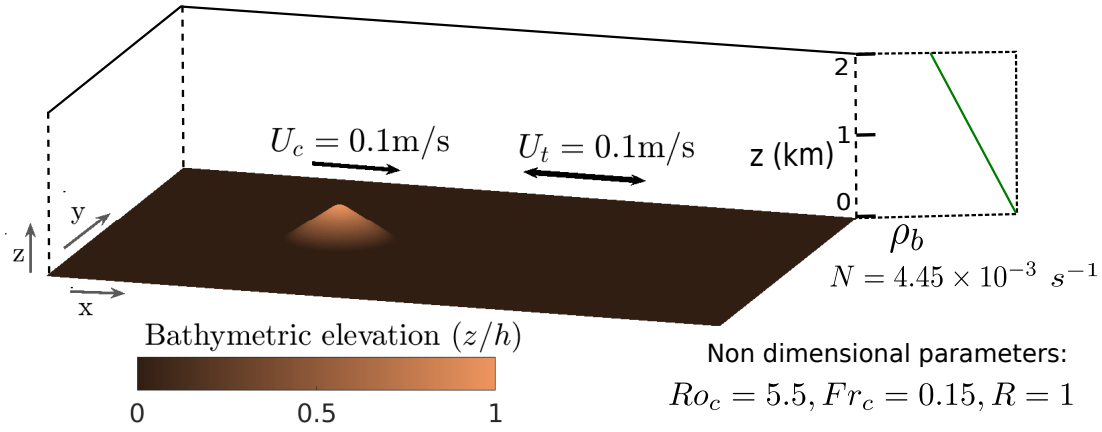

Figure 3.1: Model setup : A stratified tidally-modulated current encounters a conical obstacle located at $x = 0$.

Ocean currents are seldom steady. They often consist of high and low frequency components. In this chapter, wake vortices in tidally modulated currents past a conical hill in a stratified fluid are investigated using large-eddy-simulation. The vortex shedding frequency is altered from its natural steady-current value leading to synchronization of wake vortices with the tide. The relative frequency (f^*), defined as the ratio of natural shedding frequency ($f_{s,c}$) in

a current without tides to the tidal frequency (f_t), is varied to expose different regimes of tidal synchronization. When f^* increases and approaches 0.25, vortex shedding at the body changes from a classical asymmetric Kármán vortex street. The wake evolves downstream to restore the Kármán vortex-street asymmetry but the discrete spectral peak, associated with wake vortices, is found to differ from both f_t and $f_{s,c}$, a novel result. The spectral peak occurs at the first subharmonic of the tidal frequency when $0.5 \leq f^* < 1$ and at the second subharmonic when $0.25 \leq f^* < 0.5$.

3.1 Introduction

Steep underwater bathymetry in the deep ocean is a site of enhanced turbulence, mainly attributed to internal waves but potentially also to lee eddies. An example of steep topography is Luzon strait, where highly energetic internal tides (Alford et al., 2015) at the semi-diurnal M2 frequency and fast tidally modulated currents at submerged three-dimensional hills (Pinkel et al., 2012) have been observed. Additionally, barotropic tides are responsible for the separation of transient lee eddies from obstacles, such as headlands (Signell and Geyer, 1991; Pawlak et al., 2003; MacKinnon et al., 2019) and submerged topography (Girton et al., 2019). These lee eddies (or lee vortices) are coherent patches of vertical relative vorticity (ω_z). Vortex dynamics has received considerably less attention than internal waves in the literature on tide-topography interaction.

The flow behind underwater obstacles is observed to resemble either a von Kármán wake, as noted in the lee of small islands and/or in near-equatorial locations (see Wolanski et al., 1984; Kimura et al., 1994; Hasegawa et al., 2004; Chang et al., 2019) or a Rossby wake (Chen et al., 2015; Vic et al., 2015), where rotation, as measured by the inertial frequency (f), induces asymmetry in the strength of cyclonic and anticyclonic eddies shed from the topography. Most numerical studies have focused on Rossby wakes in a steady current U_c

(Dietrich et al., 1996; Dong and McWilliams, 2007; Perfect et al., 2018; Srinivasan et al., 2018), where vertical vorticity ω_z injected into the wake has near-inertial values. On the other hand, von Kármán wakes are characterized by higher vortical Rossby numbers ($Ro_\omega \gg 1$, where $Ro_\omega = \omega_z/f$). The spatio-temporal behavior of vortices at higher Ro_ω is significantly different from Rossby wakes and has received little attention, especially in the presence of tidal modulation.

A steady current sheds wake vortices off an obstacle at a distinct frequency $f_{s,c}$ which, by analogy with bluff-body wakes, is often estimated as $f_{s,c} \propto U_c/D$ by prescribing the Strouhal number $St_c = f_{s,c}D/U_c$. For unstratified vertical-cylinder wakes, $St_c = 0.273 - 1.11Re_D^{-1/2} + 0.482Re_D^{-1}$ (Williamson and Brown, 1998). At the $Re_D = 20,000$ of this study, the estimate is $St_c = 0.265$ which changes by less than 1% at larger Re_D. In unstratified flow, a 3D hill with sloping sides does not shed vertical-vorticity lee eddies. Instead, there is a standing horseshoe vortex and periodic hairpin vortices at low Re_D (Acarlar and Smith, 1987) which become indistinct at higher Re_D (Garcia-Villalbaa et al., 2009). Stable stratification with $Fr_c < O(1)$, which constrains the flow to go around rather than above the obstacle, is necessary for lee eddies in 3D-hill geometries (Hunt and Snyder, 1980).

Excursion number (Ex_t) quantifies the advection time scale D/U_t with respect to the tidal period. For wake vortices, a new but related parameter, the relative frequency $f^* = f_{s,c}/f_t$, is useful. The parameter f^* is related to Ex_t as $f^* = f_{s,c}/f_t = 2\pi St_c Ex_t/R$. For example, when Ex_t is 0.47 and St_c is 0.27, f^* is close to 0.8 for equal mean and tidal velocity components ($R = 1$).

Observations by Black and Gay (1987) and Signell and Geyer (1991) indicate eddies are formed at specific phases in a tidal cycle leading to the term 'phase-eddies'. Denniss et al. (1995) observed that small oscillations at the diurnal frequency in the current generates eddies at the same frequency in the lee of Bass Point, Australia. A similar phase-locking phenomenon was observed by Chang et al. (2019) on the lee side of Taiwan's Green Island. Ship-based

experiments and ADCP data showed eddies of $Ro_\omega \sim 20$ shed at near-M2 frequencies.

Alterations to the shedding frequency due to tidal synchronization can lead to significant temporal changes in bottom drag, turbulence and mixing. These changes must be accurately parametrized for their inclusion in GCMs. When the natural shedding frequency is comparable to or smaller than the tidal frequency, a central question remains unanswered: how does the tidal component of the flow influence flow separation and eddy shedding frequency? Thus motivated, we numerically study how variation of f^* affects wake characteristics. Section 3.2 introduces the numerical model, while the spatial organization of vortices and the tidal synchronization phenomenon are discussed in Section 3.3 and Section 3.4, respectively.

3.2 Model Setup

3.2.1 Simulation parameters

In the computational model, a barotropic current $U_b = U_c + U_t \sin(2\pi f_t t)$ encounters an axisymmetric conical obstacle (fig. 3.1) of height h and base diameter D. The values of $Ro_c = 5.5$ and $Fr_c = 0.15$, which are kept constant, correspond to weak rotation and strong stratification. Weak rotation ($Ro_c > O(1)$) is characteristic of flow-topography interactions past $O(1\,\text{km})$ obstacles, especially in near-equatorial locations (Liu and Chang, 2018; Rudnick et al., 2019). Strong stratification ($Fr_c \ll 1$), which is typical of deep-ocean submerged topography, favors the formation of coherent lee vortices (MacCready and Pawlak, 2001). Tidal and mean currents of equal magnitude are considered so that $R = U_t/U_c = 1$.

The relative frequency $f^* = f_{s,c}/f_t$ ranges between 0.1 and 1 in the parametric study. The objective is to examine vortex dynamics when the natural vortex shedding frequency $f_{s,c}$ in a steady current is comparable to or smaller than the tidal frequency f_t. The relationship, $f^* = 2\pi St_c Ex_t/R$ simplifies for the present value of $St_c = 0.265$[1] and $R = 1$ to a simple

[1] To confirm the value of St_c, an additional simulation of a steady current past the conical obstacle is performed

proportionality: $f^* = 1.66 Ex_t$. Thus, f^* between 0.1 and 1 leads to Ex_t between 0.06 and 0.6, values of relevance to oceanic flows (Signell and Geyer, 1991; Edwards et al., 2004; Musgrave et al., 2016). For a given tidal frequency, larger values of f^*, equivalently Ex_t, are associated with larger background velocity and smaller obstacles.

The parameters and results are discussed in non-dimensional form for ease of applicability to a wide range of specific oceanic examples with similar non-dimensional parameters. For concreteness, consider the following specific example of dimensional values. The conical obstacle is of height $h = 150$ m and diameter $D = 500$ m. The tidal amplitude and mean current are both are set to 0.1 m/s, within the range of wake observations by MacKinnon et al. (2019). The inertial frequency is set to its value at 15° N latitude, yielding $Ro_c = 5.5$. The buoyancy frequency of $N = 4.45 \times 10^{-3}$ s^{-1} leads to $Fr_c = U_c/Nh = 0.15$.

We note that stratified tidally-modulated wakes have not been studied in previous experiments or simulations. However, in unstratified fluid, a cylinder in a current having oscillatory modulation has been investigated (Barbi et al., 1986; Griffin and Hall, 1991; Konstantinidis and Balabani, 2007; Konstantinidis and Liang, 2011), albeit at lower Reynolds numbers. Experiments of Barbi et al. (1986), later confirmed by simulations, have demonstrated "locking" of wake vortices to an external forcing frequency (f_t) when f_t is near $2f_{s,c}$. These previous studies have differences (unstratified fluid, cylinder in contrast to a sloped hill, lower *Re*) with this work. Nevertheless, we will explore the possibility of lock-on in geophysical hill wakes.

3.2.2 Numerical method

Large-eddy-simulation (LES) is employed to solve for the velocity u_m ($m = 1,2,3$ are in the x, y and z directions, respectively), pressure p and density ρ. The density is further

in the absence of tidal modulation and keeping $Ro_c = 5.5$ and $Fr_c = 0.15$. At heights (up to $z^* \approx 0.8$) with distinct shedding of coherent wake vortices, it is found that $St_c = 0.265$.

decomposed into the reference density ρ_0, background density $\rho_b(z)$ and deviation ρ'. The LES involves solving the 3D Navier-Stokes equations under the Boussinesq and f-plane approximation. The equations for conservation of mass, momentum and density are given as follows :

$$\frac{\partial u_m}{\partial x_m} = 0\,, \tag{3.1}$$

$$\frac{\partial u_m}{\partial t} + \frac{\partial (u_n u_m)}{\partial x_n} - f\varepsilon_{mn3}(u_n - U_b\delta_{n1}) = -\frac{1}{\rho_0}\frac{\partial p'}{\partial x_m} - \frac{g\rho'}{\rho_0}\delta_{m3} + \frac{\partial \tau_{mn}}{\partial x_n} + F_b(t)\delta_{m1}\,, \tag{3.2}$$

$$\frac{\partial \rho}{\partial t} + \frac{\partial (u_n \rho)}{\partial x_n} = \frac{\partial \Lambda_n}{\partial x_n}\,. \tag{3.3}$$

Here, p' represents the deviation of pressure from its background value in a stationary fluid in a rotating frame. The stress tensor τ_{mn} and density flux vector Λ_n are given by :

$$\tau_{mn} = (\nu + \nu_{sgs})\left(\frac{\partial u_m}{\partial x_n} + \frac{\partial u_n}{\partial x_m}\right) \quad , \quad \Lambda_n = (\kappa + \kappa_{sgs})\frac{\partial \rho}{\partial x_n}\,, \tag{3.4}$$

where ν_{sgs} is the subgrid viscosity and κ_{sgs} is the subgrid diffusivity. The subgrid viscosity ν_{sgs} is computed using the WALE model of Nicoud and Ducros (1999) and κ_{sgs} is set to ν_{sgs}. The forcing term $F_b(t) = 2\pi f_t U_t \cos(2\pi f_t t)$ sustains the barotropic tidal component.

The computational domain is 9.5 km in the streamwise (x) direction, 3.8 km in the spanwise (y) direction and 2 km in the vertical (z) direction. For convenience, height h and diameter D are used to normalize vertical and horizontal distances: $x^* = x/D$, $y^* = y/D$ and $z^* = z/h$. The base of the obstacle is centered at the origin. The domain extends from $x = -4D$ upstream to $x = 15D$ downstream. In the lateral direction, the domain extends from $y = -4D$ to $y = 4D$. To resolve the wake turbulence, $1536 \times 1280 \times 322$ grid points are used in the x, y and z directions, with stretching in x and z. The quadratic drag-law BC for the bottom stress is prescribed on the flat bottom and obstacle, following Rapaka and Sarkar (2016). For density, the no-flux BC is imposed to keep the system adiabatic. All the simulations have been run for

at least 50 cycles, with the exception of the $f^* = 1$ case which was run for 25 tidal cycles.

3.3 Overall flow characteristics

In the absence of tidal flow, the body-generated lee waves are steady at Froude numbers of $O(0.1)$ as shown in experiments (Hunt and Snyder, 1980; Dalziel et al., 2011) and numerical simulations (Ding et al., 2003; Puthan et al., 2020). However, tidal oscillation leads to transient lee waves (Bell, 1975). Vortex dynamics is modifed, for instance, from organized eddy trains to trapped eddy pairs past elongated islands (Wolanski et al., 1984), and periodic phase eddies (Signell and Geyer, 1991). In this section, the velocity and vorticity fields (fig. 3.2) for the case $f^* = 1$ are used to illustrate the salient flow characteristics at three different time instants: $T_1 = 9.4T$, $T_2 = 9.75T$ and $T_3 = 10T$ where T denotes the tidal period.

Figure 3.2a shows a developing lee wave field at $t = T_1$, visualized by u/U_c at the mid-centerplane $y^* = 0$. The low-level jet at the topographic apex generates steepened isopycnals and there is a hydraulic jump. There is significant isopycnal deformation along the entire obstacle height. The wake is illustrated by a horizontal cut of u/U_c (fig. 3.2b) at the same instant. The recirculation region extends out to $x^* = 1$, beyond which the wake grows laterally and there are large velocity fluctuations associated with enhanced near-field turbulence. A locally adverse streamwise pressure gradient induces flow separation and lee vortices. Two coherent opposite-signed vortices are seen behind the body at $t = T_1$ (fig. 3.2c). Vortex formation involves streamwise flow reversal, followed by lateral flapping in the wake, as in a von Kármán wake. During T_1 to T_2, the tide-associated pressure force acts in the upstream direction to decrease the far-field velocity to zero. For the lower-speed fluid in the lee, the same pressure force is able to locally advect high-vorticity fluid upstream. For instance, the large anticyclonic vortex in panel *d* was driven in the $-x$ direction during T_1 to T_2 and deflected in the $+y$ direction by the body. Additional cyclonic vorticity is also generated from the

roll-up of the shear layer formed between the locally upstream flow and the obstacle sides. This mechanism results in the formation of two vortex dipoles, one on each lateral side of the obstacle. During the subsequent acceleration phase and the re-emergence of downstream velocity, the dipoles separate from the obstacle and move downstream (fig. 3.2e).

It is evident that the near-body vortex pattern, in particular the dipole at each side, differs significantly from the alternate shedding of monopoles from each side in a Kármán vortex street. Indeed symmetric, antisymmetric and asymmetric near-wake modes were observed by Barbi et al. (1986), although in unstratified fluid and for a cylinder, in a current with along-flow sinusoidal perturbations. Here, at $f^* = 1$, a dipole forms at the body in each tidal cycle. However, the dipole disintegrates within a short distance after interaction with opposite-signed vorticity, and is not seen in the far wake. Clearly, investigation of wake vortex dynamics over a range of f^* values is warranted, and will be the focus of the next section.

3.4 Temporal oscillations in the wake

Figure 3.2(c-e) qualitatively showed that tidal oscillation influences vortex shedding from the body. The vortex dynamics at the body and further downstream in the wake are quantified for the $f^* = O(1)$ regime by plotting the vertical vorticity (ω_z) at 8 phases (fig. 3.3a-h) for the $f^* = 5/6$ case and velocity spectra in (i) and (j). Since the tidal period is shorter than the natural vortex-shedding period, completion of the Strouhal shedding cycle to form a full vortex pair is not possible. During the phase of downstream tide, which precedes the sequence that begins in fig. 3.3a, an asymmetric attached vortex pair is observed similar to that shown in fig. 3.2c. As the barotropic velocity decelerates to zero at $t = 11.75T$ (not shown), wake vorticity is advected upstream and a secondary dipole begins to separate in the +y direction. A fraction of negative (anticyclonic) vorticity from the primary recirculation zone is isolated and forms the coherent patch close to the centerline at $x = 2$ in fig. 3.3a ($t = 12T$). At this instant,

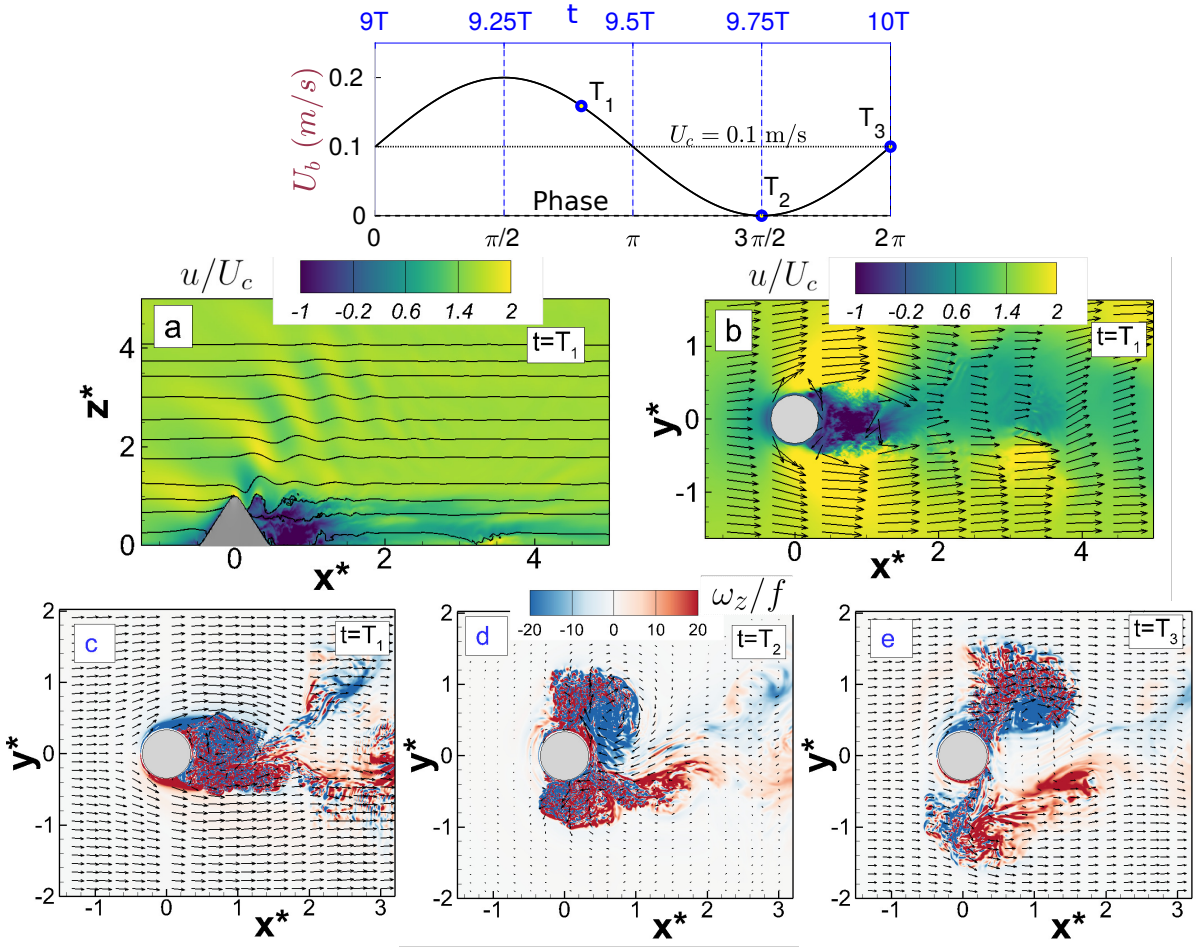

Figure 3.2: Flow visualization for the $f^* = 1$ case: (a) Streamwise velocity in the vertical $x-z$ plane at $y^* = 0$ and $t = T_1$; (b) Streamwise velocity in the horizontal $x-y$ plane at $z^* = 0.25$ and $t = T_1$; (c-e) Vertical vorticity in the horizontal $x-y$ plane at $z^* = 0.25$ and at three time instants T_1, T_2 and T_3. Header shows the barotropic velocity $U_b(t)$.

the dipole and anticyclonic vortex are well developed. Note that Ro_ω for these vortices is as large as 16-20. By $t = 12.25T$ (fig. 3.3b), the anticyclonic vortex has advected downstream and a new Strouhal pair begins to form in the lee of the obstacle. By $t = 12.5T$ (fig. 3.3c), the secondary dipole observed at $t = 12T$ has largely disintegrated, while the anticyclonic vortex remains coherent and continues to move downstream.

Between $t = 12.75T$ and $13T$ (fig. 3.3d,e), a new secondary dipole is generated in the -y direction including a portion of positive vorticity from the primary Strouhal vortex.

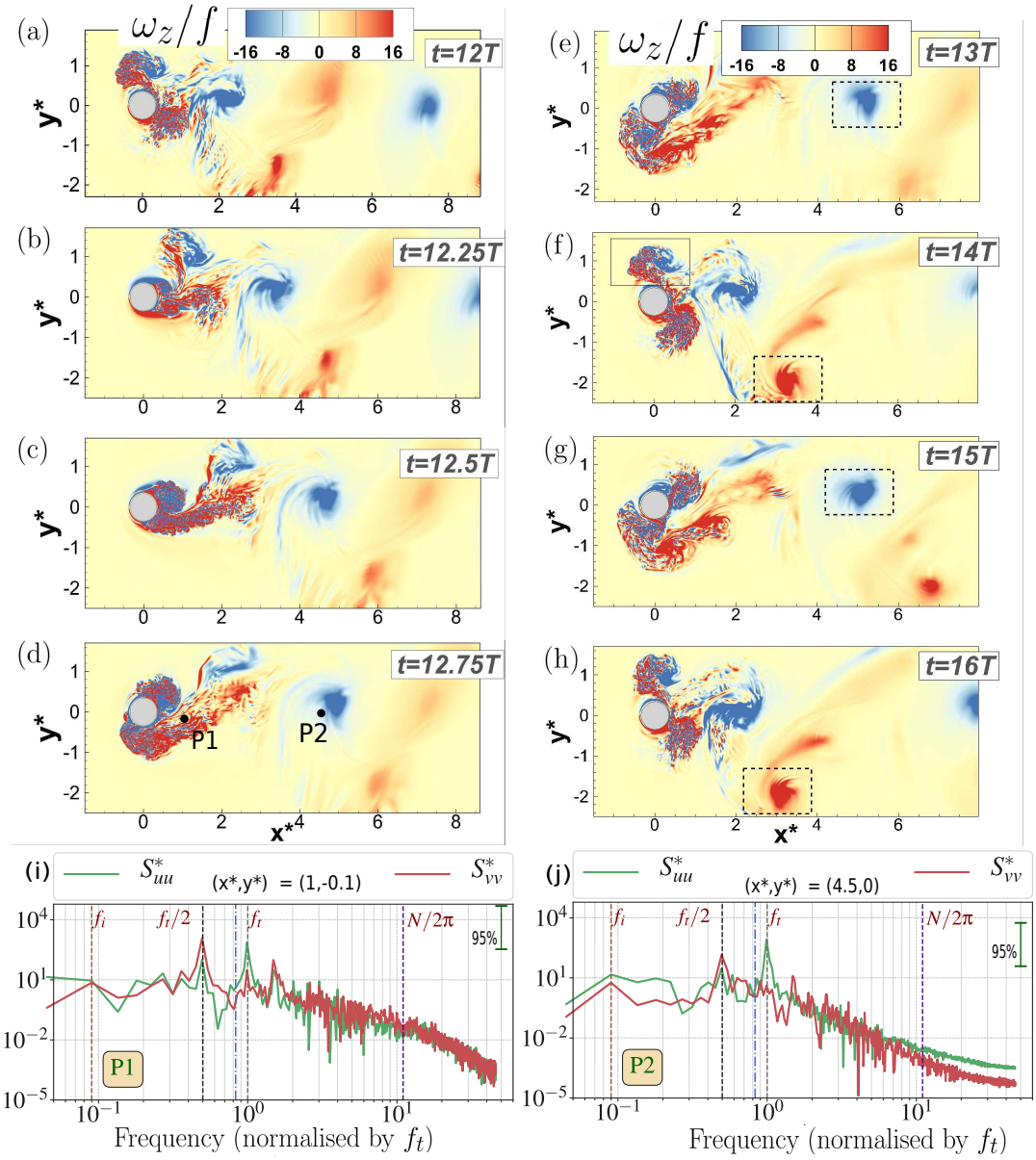

Figure 3.3: Eddy formation as depicted by the normalized vertical vorticity (ω_z/f) in the $f^* = 5/6$ case: (a-d) Development of eddies during the 12^{th} tidal cycle; (e-h) Consistent formation of dipoles at the body during each following tidal cycle. (i,j) Normalised streamwise velocity spectra $S^*_{uu} = S_{uu}/U_c^2$ and spanwise velocity spectra $S^*_{vv} = S_{vv}/U_c^2$ at locations P1 and P2, respectively. The locations of P1 and P2 are marked in (d) and their coordinates are given in the header of (i) and (j), respectively. The blue dash-dotted line at frequency of $5f_t/6$ denotes the natural shedding frequency.

Analogous to what was observed for the vortex with negative ω_z generated in the previous cycle, a portion of the positive vorticity separates and forms a coherent patch that subsequently

advects downstream, as highlighted by the dashed box in fig. 3.3f. By $t = 14T$ (fig. 3.3f), the anticyclonic vortex formed in the prior tidal cycle (was shown at $t = 13T$ by the dashed box) has moved out of the computational domain. In the next cycle, $t = 14T$ (fig. 3.3f), a new secondary dipole is again formed in the positive y-direction and an anticyclonic vortex is observed to move downstream, repeating the sequence. This recurring pattern, involving disintegration of the near-body dipole and formation of a persistent anticyclonic and cyclonic vortex on opposite sides during successive tidal cycles, accounts for the far-field wake-vorticity pattern. Comparison of ω_z at intervals of $2T$ in fig. 3.3 reveals the recurring pattern. Opposite-signed vortices in the wake thus occur with the time offset of a tidal cycle so that a complete Strouhal pair is formed over two tidal cycles.

The appearance of coherent wake vortices has consequences on the energy spectra shown in fig. 3.3(i,j). Spectra of streamwise and spanwise velocity were recorded at 2 spatial probes, P1 at (x^*, y^*, z^*)=(1,-0.1,0.25) and P2 at (x^*, y^*, z^*)=(4.5,0,0.25), which are marked in fig. 3.3d. While there is a spectral bump at the inertial frequency f, the dominant peak is at f_t in S^*_{uu} (green curve) and its first subharmonic ($f_t/2$) in S^*_{vv} (red curve). The subharmonic corresponds to the previously discussed completion of a wake-vortex cycle in two tidal cycles. This result of a peak at the subharmonic is robust over the entire height of the obstacle (from near the bottom to $z^* \approx 0.8$) where coherent wake vortices are distinct. The S^*_{vv} and S^*_{uu} spectra are broad-banded at the probes owing to smaller-scale turbulence.

An important result, illustrated by fig. 3.3, is the locking of the wake-vortex frequency to the first subharmonic of the tidal frequency when $f^* = 5/6$. To delineate differences with the natural shedding frequency ($f_{s,c}$), we define the following quantity: f_s, which denotes the frequency of wake vortices *observed* in the simulations and $St = f_s D/U_c$ as the corresponding Strouhal number. When $f^* = f_{s,c}/f_t = 5/6$, the value of f_s/f_t is 0.5.

We now examine the velocity spectra for all simulated cases. Figure 3.4(a-f) shows normalized v-spectra at location P2 computed from the flow history over several tidal cycles.

For example, 40 tidal cycles of data are used at $f^* = 1/10$, 42 at $f^* = 1/6$, and 16 at $f^* = 1/2$. To compute spectra, a time record with a small uniform time step (e.g. $f_t \Delta t = 0.025$ for the case with $f^* = 1/10$) was created from the simulation data whose non-uniform step for time advance is much smaller. By definition, $f^* = 1/10$ and $f^* = 1/6$ correspond to natural vortex shedding being much slower than the tidal oscillation frequency, i.e. large obstacles and slow flows. Since f_s and f_t are widely separated, vortex shedding is unaltered from its natural no-tide value of $f_{s,c}$ so that f_s/f_t coincides with f^*. At these small values of f^*, the excursion length of the fluid over a tidal cycle is small. Therefore, the strength of the vortices produced over a single cycle is small and also the tidal vortices do not migrate into the wake. Since the accumulated effect of tidal vorticity on wake dynamics is small, wake vortices are seen at the natural frequency, $f_{s,c}$. Figure 3.4(a,b) shows a strong peak in S^*_{vv} at $f_t/10$ for case $f^* = 1/10$, and at $f_t/6$ for case $f^* = 1/6$. In the $f^* = 1/3$ case, the wake dynamics are more complex. The near wake has a symmetric mode owing to tidal dipoles. The separation vorticity that is not destroyed in the near field, subsequently organizes into a sequence of Strouhal vortices in the far wake (location P2) displaying a frequency of $f_t/4$ (fig. 3.4c). This pattern is evident in the $f^* = 0.25$ and $f^* = 0.42$ cases as well and leads to a spectral peak at $f_t/4$ (shown for $f^* = 0.42$ in fig. 3.4d).

In the cases with $f^* = 1/2$ and 1, the values of f_s/f_t lock-on to $1/2$ (fig. 3.4 e,f), similar to case $f^* = 5/6$ discussed in fig. 3.3. The observed lock-on of wake-vortex frequency to $f_t/2$ and $f_t/4$ can be understood as follows. A current without tides produces a Kármán wake with lateral meanders that possess the following spatio-temporal symmetry: $u(x,y,z,t) = u(x,-y,z,t+T_s/2)$, where $T_s = 1/f_s$ is the time period of wake vortices. A superposed tidal oscillation induces temporal periodicity $u(x,y,z,t) = u(x,y,z,t+nT)$, where $n = 1,2,..$ denotes the number of tidal cycles, and additionally a lateral symmetry $u(x,y,z,t) = u(x,-y,z,t)$ since the entire flow is equally forced by the tide. Thus, the tide imposes $u(x,y,z,t) = u(x,-y,z,t+nT)$. The injection of near-wake vorticity by fast tidal oscillation averages out over $T_{s,c}$ until f^*

increases to about 0.25, at which point the wake is affected. Specifically, the period of vortices in the downstream wake is modified such that $nT = T_s/2$, or equivalently $f_s/f_t = 1/2n$ so that not only the symmetry of the tidal oscillation, $u(x,y,z,t) = u(x,-y,z,t+nT)$, is maintained but also the spatio-temporal symmetry of the Kármán wake, $u(x,y,z,t) = u(x,-y,z,t+T_s/2)$, is reinstated. Thus, the wake-vortex frequency synchronizes with the tidal frequency by becoming its subharmonic. To achieve synchronization, near-wake vorticity shed near the body at each tidal cycle adjusts to establish the spatial asymmetry of the Kármán vortex street as was demonstrated earlier for $f^* = 5/6$. The results here show a preference for *tidal synchronization* to $f_t/2$ ($n = 1$) or $f_t/4$ ($n = 2$), with the specific value selected so that it is close to but not larger than $f_{s,c}$.

Figure 3.4g summarizes the overall behavior in a plot of f_s/f_t against f^*. At low f^*, the tidal oscillation is much too fast to affect the wake vortices, f_s remains equal to $f_{s,c}$, and f_s/f_t increases linearly with increasing f^*. The situation changes when f^* reaches 0.25. Between $f^* = 0.25$ and $f^* = 0.5$, the wake vortices synchronize to $f_t/4$, and eventually to $f_t/2$ for $0.5 \leq f^* < 1$. Equivalently, the observed St(blue curve in fig. 3.4g) deviates from its natural value of St_c in the cases exhibiting tidal synchronization. The value of St_c serves as an upper limit on St. The frequency locking to $f_t/2$ is prevalent over a larger range of f^* values. Such $f_t/2$ tidal synchronization to the M2 tide with a period of 12.42h would result in wake vortices at a period of 24.84h, which could be misinterpreted as the K1 tide (23.92h) in observations. It is thus necessary to distinguish the subharmonic of M2 from the diurnal frequency in observational data on flow-topography interactions.

3.5 Conclusions

The interaction of a tidally modulated current, $U_b = U_c + U_t \sin(2\pi f_t t)$, with a conical obstacle having base diameter D is examined on an f-plane. The wake of a stratified tidally

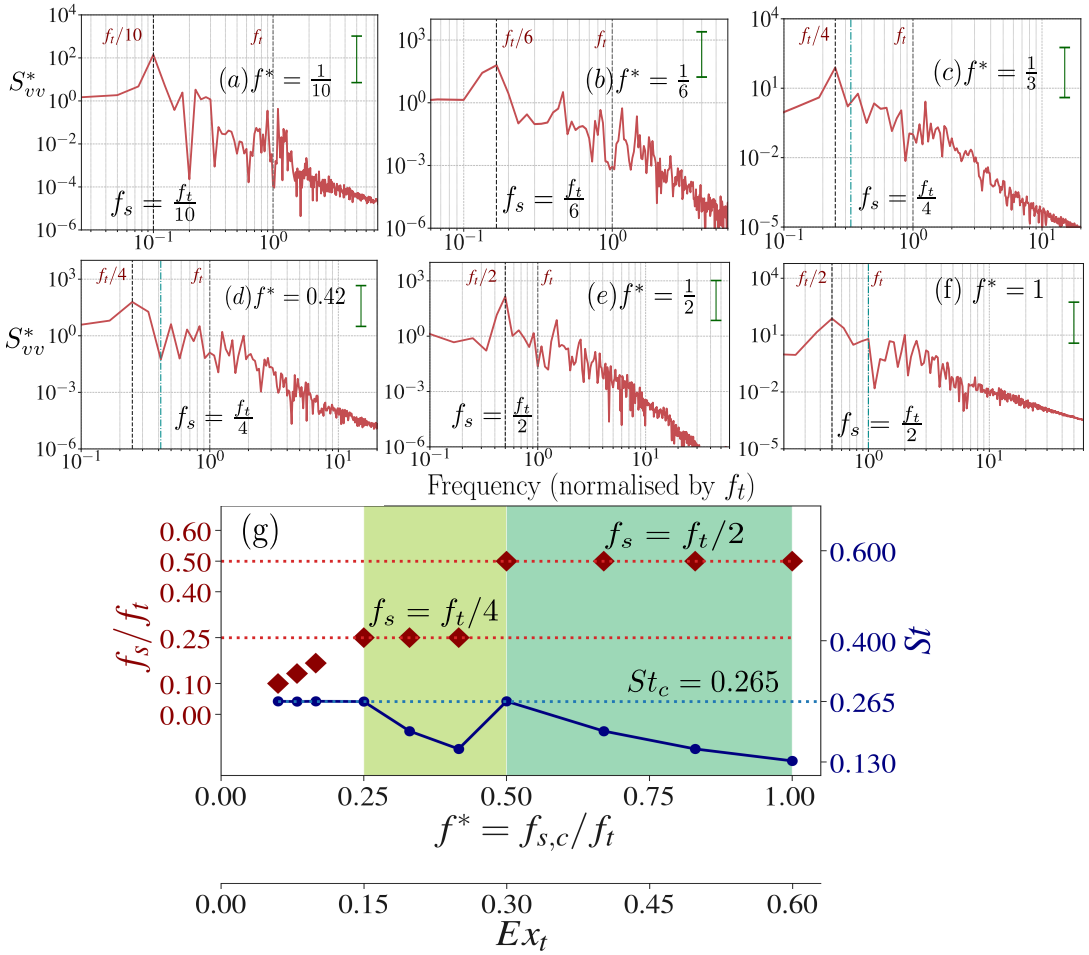

Figure 3.4: Tidal synchronization in all simulated cases. (a-f) Spectra of spanwise velocity (S^*_{vv}) at P2 shown for various f^*. (g) The observed value of normalized wake-vortex frequency f_s/f_t (♦) and observed Strouhal number St (•) are plotted against f^*. Here, $St_c = 0.265$ corresponds to natural shedding without tides. The shaded region represents the parameter space with tidal synchronization. The green bar in (a)-(f) shows the 95% confidence interval of the spectrum.

modulated current has received little attention relative to a uniform, strongly stratified steady current where coherent lee vortices are formed downstream. It is worth noting that the configuration of these coherent lee vortices is qualitatively different from the horseshoe and hairpin vortices formed in an unstratified environment. These lee vortices are shed at a constant shedding frequency $f_{s,c}$ which is $\propto U_c/D$ to form a Kármán vortex street in the steady-current case of a stratified wake. The wake changes qualitatively in response to tidal modulation,

parameterized here by the relative frequency $f^* = f_{s,c}/f_t$ which is varied between 0.1 and 1. When f^* approaches about 0.25, instead of the typical asymmetric shedding of vortex monoples, vortices separate laterally from the obstacle from each side during every tidal cycle to form periodic vortex dipoles. These dipoles are unstable and break down within few diameters of the obstacle, as described for $f^* = 5/6$. A Kármán vortex street with asymmetrically placed vortices develops downstream, but with frequency f_s in the wake altered from $f_{s,c}$. The tidal oscillations alter the temporal wake evolution, which may also have significant ecological implications through their effect on the retention of water and nutrients.

When $0.5 \leq f^* \leq 1$, wake vortices appear at the first subharmonic of the tidal frequency, i.e the wake synchronizes to $f_t/2$. However, when f^* exceeds 0.25 but is less than 0.5, synchronization to $f_t/4$ is observed. The periodicity and lateral symmetry imposed by the tidal forcing on the near wake is different from the spatio-temporal symmetry of a Kármán vortex street. As a result of tidal synchronization, the spatio-temporal symmetry of a Kármán wake is re-established while respecting the temporal periodicity of the tide by modifying the wake-vortex frequency to $f_t/(2n)$ $(n = 1, 2)$. While $f_t/2$ is the preferred frequency of wake vortices for cases with $0.5 \leq f^* \leq 1$, the value of $f_t/4$ is the preferred frequency when $0.25 \leq f^* < 0.5$. It is interesting that tidal oscillations that are faster than natural shedding act to slow down the observed shedding frequency from its natural value through synchronization to a tidal subharmonic. The larger tidal period in the regime of $f^* > 1$, not examined here, allows for wake vortices at the natural frequency $f_{s,c}$. Exploration of the interaction of these wake vortices with the tide is deferred to future work.

Acknowledgements

This chapter, in full, is a reprint of the material as it appears in "Tidal synchronization of lee vortices in geophysical wakes", P. Puthan, S. Sarkar and G. Pawlak, *Geophysical review*

letters, 48, 2021. The dissertation author is the primary investigator and author of this paper.

Chapter 4

High drag states in tidally modulated stratified wakes

Large eddy simulations (LES) are employed to investigate the role of time-varying currents on the form drag and vortex dynamics of submerged 3D topography in a stratified rotating environment. The current is of the form $U_c + U_t \sin(2\pi f_t t)$, where U_c is the mean, U_t is the tidal component and f_t is its frequency. A conical obstacle is considered in the regime of low Froude number. When tides are absent, eddies are shed at the natural shedding frequency $f_{s,c}$. The relative frequency $f^* = f_{s,c}/f_t$ is varied in a parametric study which reveals states of high time-averaged form drag coefficient. There is a two-fold amplification of the form drag coefficient relative to the no-tide ($U_t = 0$) case when f^* lies between 0.5 and 1. The spatial organization of the near-wake vortices in the high drag states is different from a Kármán vortex street. For instance, the vortex shedding from the obstacle is symmetric when $f^* = 5/12$ and strongly asymmetric when $f^* = 5/6$. The increase in form drag with increasing f^* stems from bottom intensification of the pressure in the obstacle lee which is linked to changes in flow separation and near-wake vortices.

4.1 Introduction

Rough bottom topography in the abyssal ocean contributes significantly to enhancement of drag and turbulent dissipation. Egbert and Ray (2000, 2001) estimate that up to 1 TW of power is lost *in-situ* from tide-topography interactions in the abyssal ocean. When abyssal flow encounters rough topography, energy is lost in two ways: (1) through skin friction resulting from tangential stress at the boundary and (2) via pressure/form drag resulting from normal stress. Energy loss from friction is usually small, with estimates in the $O(0.02\ \mathrm{mW/m^2})$ or approximately 7 GW on a global scale (Jayne and Laurent, 2001), accounting for less than 1% of the 1 TW estimate of Egbert and Ray (2000, 2001). Recent studies of Zhang and Nikurashin (2020) and Klymak (2018) highlight the crucial role played by multiscale topography in extracting momentum (through topographic form stress) from the background flow and maintaining a dynamic balance in the abyssal ocean. Thus, form drag is often the primary mechanism of energy extraction from the barotropic tide, especially at steeper topographies (McCabe et al., 2006; Howritz et al., 2021).

In situ measurements in literature show that the loss of momentum associated with form drag is enhanced by obstacles in the coastal ocean such as headlands (Edwards et al., 2004; Magaldi et al., 2008; Warner et al., 2012; Warner and MacCready, 2014) and continental shelves (Nash and Moum, 2001; Wijesekera et al., 2014). However, observational studies of form drag estimates from the abyssal ocean are limited. Lack of information on the magnitude and spatial distribution of form drag presents a challenge for form drag parameterizations in global climate models (GCMs). Numerical studies can play an important role in bridging this gap. Warner and MacCready (2009) performed numerical simulations with the hydrostatic ROMS model of a non-rotating tidal flow past a Gaussian headland to examine different components of form drag. They showed that while the normalized separation drag (the average drag coefficient) increased with an increase in the aspect ratio of the headland, it does not

depend on the tidal excursion or the headland size. In the present work, we examine form drag in tidally modulated flow past an underwater obstacle. Turbulence resolving simulations enable us to study the time varying flow past obstacles without compromising on the accuracy of their representation. The characterization of flow separation and pressure distribution on the obstacle allows us to link underlying physical mechanisms to any changes in the observed form drag.

Form drag on an obstacle is dependent on the ambient stratification. When a steady current encounters a 3D ridge, the flow transitions to a state of high drag when the Froude number reduces below 1, e.g. Epifanio and Durran (2001); Vosper et al. (1999). In situ tidal measurements of form drag are challenging and there are few such observations, e.g. Voet et al. (2020), who infer pressure from density measurements using the hydrostatic approximation. Additionally, tide induced unsteadiness may lead to changes in flow separation and distribution of lee vorticity. For example, tidal currents create transient lee eddies (or lee vortices) in wakes behind headlands (Pawlak et al., 2003; Callendar et al., 2011; MacKinnon et al., 2019) and submerged topography (Girton et al., 2019). Complexity in the impinging flow, variable stratification and irregular bathymetry at these sites present a challenge in elucidating the role of lee eddies. To examine the role of tides in flow separation and form drag, we perform turbulence-resolving simulations of an oceanic wake past a conical hill generated by a tidally modulated flow. The background flow may be expressed as $U_b = U_c + U_t \sin(\Omega_t t)$, where U_c and U_t are the mean and tidal components and $\Omega_t = 2\pi f_t$ is the tidal frequency (in rad/s).

In this chapter, we address the questions pertaining to momentum loss of abyssal currents during flow-topography interactions at the obstacle and the associated wake-vorticity distribution. The motivation for this work is two-fold. We explore possible states of large form drag owing to changes in pressure distribution in the lee and determine the qualitative changes to the vorticity distribution in the near wake in each state. Section 4.2 introduces the parameter space and lists the cases performed in the study. A brief introduction to form stress and an

overview of previous literature related to form drag is provided in section 4.3. Section 4.4 elucidates the changes in form drag on varying f^* and section 4.5 elucidates the underlying changes to flow separation. The paper concludes with a brief summary in section 4.6.

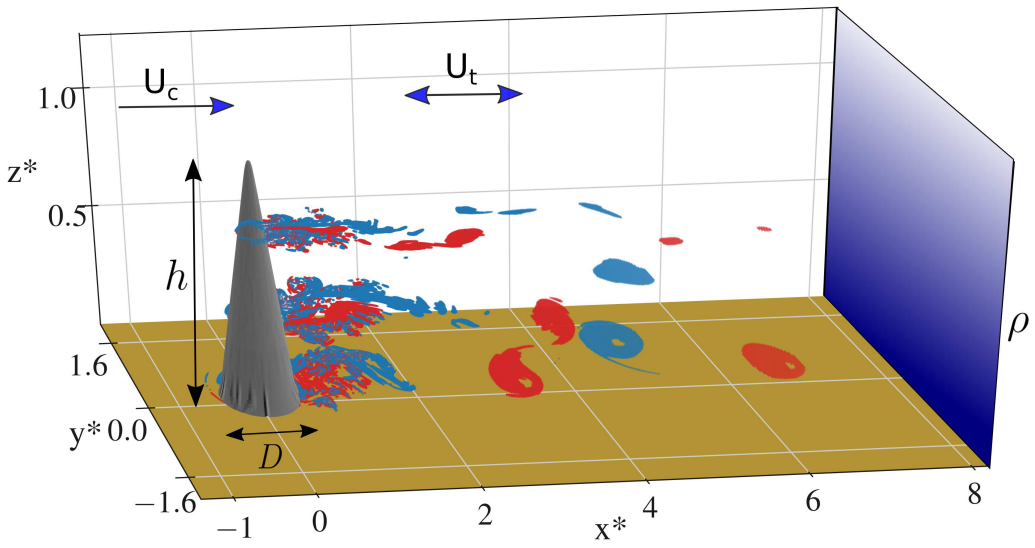

Figure 4.1: The numerical model setup is shown for the following model problem: a tidally modulated current encounters a conical obstacle in a stratified environment. The vortex shedding pattern in three horizontal planes for case $f^* = 2/15$ is represented using isosurfaces of vertical vorticity corresponding to $\omega_z/f = \pm 10$.

4.2 Simulation parameters

A regime of weak rotation and strong stratification is considered in the study. Inertial effects on the wake are weak in the lee of abyssal hills and headlands at length scales of O(1km) near the equator (Rudnick et al., 2019; Liu and Chang, 2018). These flows may be classified under the high Rossby number regime ($Ro_c > 1$). The inertial frequency is set to its value at $15^\circ N$ such that $Ro_c = 5.5$. Much of the topography in the abyssal ocean is subject to flow conditions with $Fr_c \ll 1$ e.g. Nikurashin and Ferrari (2010). To this end, we consider a topographic Froude number Fr_c of 0.15 where the flow is predominantly around the obstacle, creating coherent vortices as observed in geophysical wakes (Perfect et al., 2018).

Table 4.1: Different cases in this study: The relative frequency $f^* = f_{s,c}/f_t$ is varied among 9 cases. Four regimes with different patterns of wake vortices are observed and are discussed with representative cases shown in the table. The values of Re_D, Fr_c and Ro_c are fixed at 20000, 0.15 and 5.5 respectively.

Regime	**Case**	**Category**	**Far wake shedding frequency(f_s)**	**Near wake vortex shedding pattern**
1	$f^* = \infty$	No tides	$f_{s,c}$	Kármán vortex street
2	$f^* = 2/15$	$f^* < 1/4$	$f_{s,c}$	Vortex pulses + Kármán vortex street
3	$f^* = 5/12$	$1/4 \leq f^* < 1/2$	$f_t/4$	Symmetric twin dipoles
4	$f^* = 5/6$	$1/2 \leq f^* \leq 1$	$f_t/2$	Strong asymmetric shedding

Tidal modulations are added to the mean flow. We consider tidal velocities of amplitude equal to the mean current, so that $R = U_t/U_c = 1$. The relative frequency $f^* = f_{s,c}/f_t$ is varied from 0.1 to 1 in a parametric study with nine cases to examine the variations in vortex dynamics and form drag. Equivalently, Ex_t is varied from 0.06 to 0.6 (assuming $St_c = 0.265$), values of relevance in the ocean (Signell and Geyer, 1991; Edwards et al., 2004; Musgrave et al., 2016). At a constant tidal frequency f_t e.g. the M2 tide, larger f^* values are associated with obstacles of smaller length scales.

Different regimes of tidal synchronization were observed by Puthan et al. (2021b), wherein the lee vortices in the far wake were found at frequencies $f_{s,c}$, $f_t/4$ or $f_t/2$. These regimes are listed in table 4.1. Regime 1 consists of a single case ($f^* = \infty$) with no tidal modulations in the background flow (i.e. $R = 0$). In regime 2-4, R equals 1 and multiple cases are explored within each regime at discrete f^* values. As listed in the second column of table 4.1, one case is chosen to illustrate each regime: $f^* = 2/15, 5/12$ and 5/6 cases, for regimes 2, 3 and 4, respectively. Each regime has a distinctive near-wake vortex shedding pattern (listed in the 5th column of table 4.1). The differences in the vortex shedding at the hill play a crucial role in changing the topographic pressure distribution, motivating our study of role of f^* on the separation of vortices at the obstacle and its influence on form drag.

4.3 Form drag in oscillatory flows

Flow-bathymetry interactions result in pressure differences across abyssal obstacles, which manifests as form drag. Recent measurements at Palau estimated large form drag acting on the tidal and mean components of the flow at very low Froude numbers (Voet et al., 2020). The pressure deviation p may be represented as:

$$p = p_d + (x - x_0)\frac{\partial p_\infty}{\partial x} \tag{4.1}$$

where, $\partial p_\infty/\partial x = -\rho_0 dU_b/dt = -\rho_0 U_t \Omega_t \cos(\Omega_t t)$ is the pressure gradient driving the barotropic current U_b and p_d is the dynamic pressure. The drag force due to form drag is computed as

$$F_D = -\int p\delta_{1j} n_j dA \tag{4.2}$$

Using eq. (4.1), eq. (4.2) may be expanded as

$$F_D = -\int p_d \delta_{1j} n_j dA + \rho_0 \forall \frac{\mathrm{d}U_b}{\mathrm{d}t} \tag{4.3}$$

The first term on the right-hand side of eq. (4.3) includes contribution from two sources : (a) the separation drag associated with flow separation at the obstacle (F_D^S) and (b) the added mass (F_D^A) (Lamb, 1930; Keulegan and Carpenter, 1958). The drag associated with added mass is approximated in literature (e.g. Morison et al., 1950) using the relation

$$F_D^A = C_a \rho_0 \frac{\mathrm{d}U_b}{\mathrm{d}t} \forall \tag{4.4}$$

where, C_a is the added mass coefficient. The second term on the right-hand side of eq. (4.3) represents the Froude-Krylov force (F_D^{FK}) associated with the oscillating pressure gradient p_∞ (Yu et al., 2018). The sum of the added mass force (F_D^A) and the Froude-Krylov force (F_D^{FK}) is

referred to as inertial drag (F_D^I).

$$F_D^I = F_D^{FK} + F_D^A = \rho_0 \frac{\mathrm{d}U_b}{\mathrm{d}t} \forall + C_a \rho_0 \frac{\mathrm{d}U_b}{\mathrm{d}t} \forall \tag{4.5}$$

Therefore, the total drag force in eq. (4.3) can now be written as (e.g. Warner and MacCready, 2009) :

$$F_D = F_D^S + F_D^A + F_D^{FK} = F_D^S + F_D^I \tag{4.6}$$

Warner and MacCready (2009) concluded that the net contribution of inertial drag vanishes when averaged over a tidal cycle. Therefore, its contribution is estimated using eq. (4.5), and removed from F_D to compute the separation drag. The separation drag is assumed to be in-phase with U_b while the inertial drag variability has a phase difference of $\pi/2$ with respect to U_b (Morison et al., 1950).

A similar drag force decomposition was proposed by Lighthill (1986), wherein the inviscid inertial drag is estimated from potential flow theory. However, the force decomposition of Lighthill (1986) has limitations. Sarpkaya (2001) argued that the force decomposition of Lighthill (1986) might exclude the effects of viscosity on the added mass. His results also demonstrate that the added mass coefficient C_a is time-dependent. He asserted that the subtraction of the ideal inertial force (calculated from potential flow approximation) from the total form drag, leaves behind a force that consists of both the separation drag *and* an 'acceleration-dependent' inertial force. However, the contribution from inertial drag is negligible in the time-averaged value of F_D, when the average is computed over a large time duration (spanning multiple tidal cycles) in a statistically stationary flow (Sarpkaya, 2001). Thus the approximations of Warner and MacCready (2009) can serve as a theoretical basis to aid the interpretation of the present results by providing an adequate estimate of the separation drag. In other words, the time-mean of the form drag is representative of the separation drag

F_D^S.

In the next section, we examine the time-averaged mean, phase averaged and root-mean-squared (RMS) values of F_D defined below:

$$\text{Mean drag: } \langle F_D \rangle = \frac{\int_0^{nT} F_D dt}{nT}$$

$$\text{Phase averaged drag: } \langle F_D \rangle_\phi = \frac{\sum_{k=0}^{n} F_D(\Omega_t T k + \phi)}{n}$$

$$\text{RMS drag: } \langle F_D \rangle_{rms} = \sqrt{\frac{\int_0^{nT} (F_D - \langle F_D \rangle)^2 dt}{nT}}$$

Here, T is the tidal period, $\phi = \Omega_t t$ is the tidal phase and n is the number of tidal cycles. The value of n is larger than 6 for all cases.

4.4 Pressure anomalies in the wake

In a low Fr_c environment, the encounter of a steady current with a 3D obstacle forces a significant volume of fluid to navigate laterally. This laterally driven flow separates and wake eddies are formed in the lee. The form stress increases as a result. To examine the origin of form stress, a thorough characterization of the dynamic pressure p_d is crucial. The form drag is computed as the sum of the surface integral of p_d and the Froude-Krylov force, as shown in eq. (4.3). Note that the surface integral of p_d is inclusive of the added-mass component of inertial drag. In section 5a, the dynamic pressure field is examined in the wake and on the obstacle. Changes in eddy shedding and form stress are illustrated and quantified over the flow regimes listed in table 4.1. Estimates of F_D and their values relative to $f^* = \infty$ (no-tide) case, are provided in section 5b.

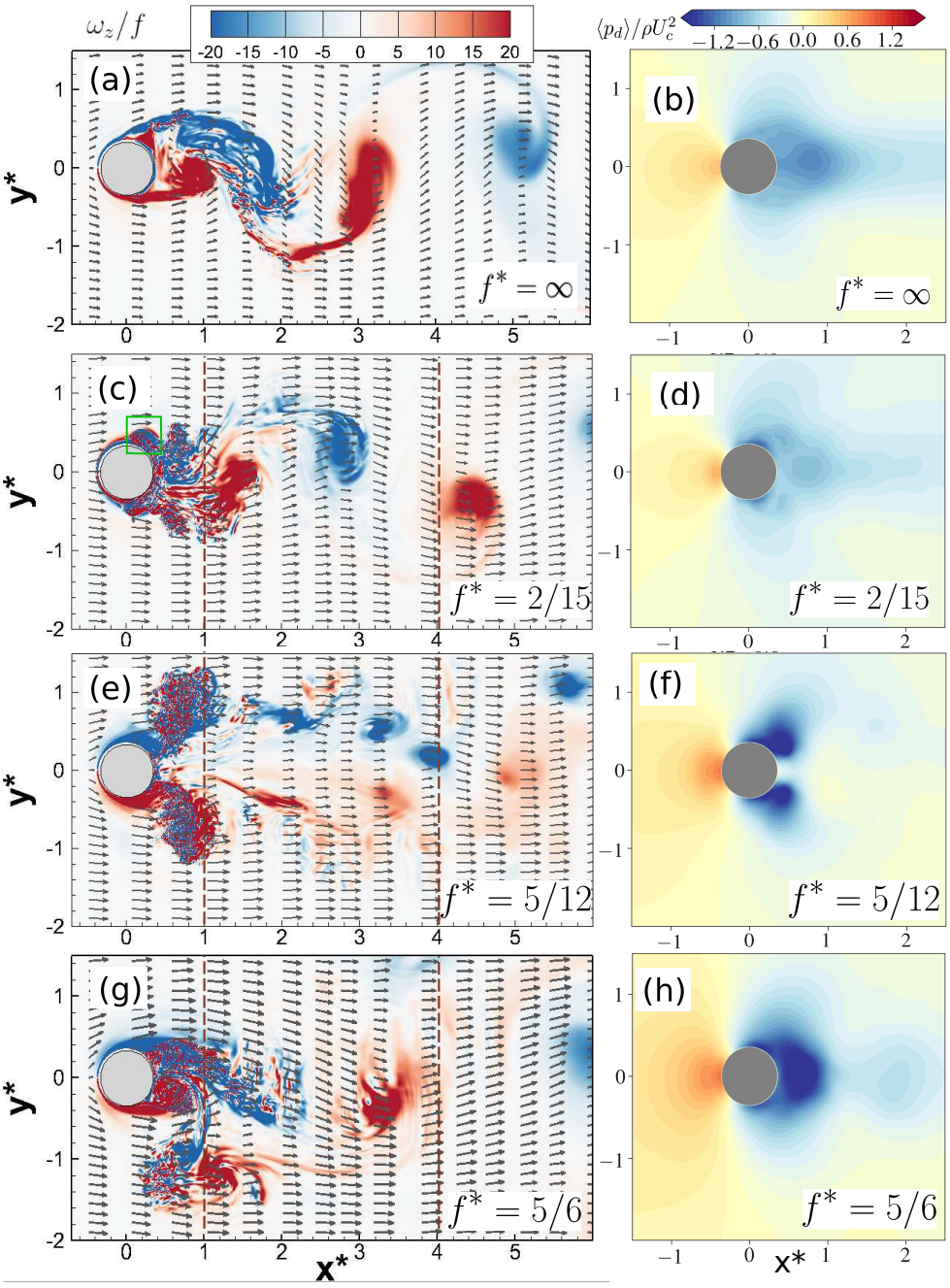

Figure 4.2: Instantaneous contours of normalized vertical vorticity (ω_z/f) and time-averaged pressure ($\langle p_d \rangle/\rho_0 U_c^2$) in the horizontal plane $z^* = 0.25$: (a,b) $f^* = \infty$, (c,d) $f^* = 2/15$, (e,f) $f^* = 5/12$ and (g,h) $f^* = 5/6$. In the tidally-modulated cases, the contours of vorticity are plotted at the maximum velocity phase ($\Omega_t t = \pi/2$).

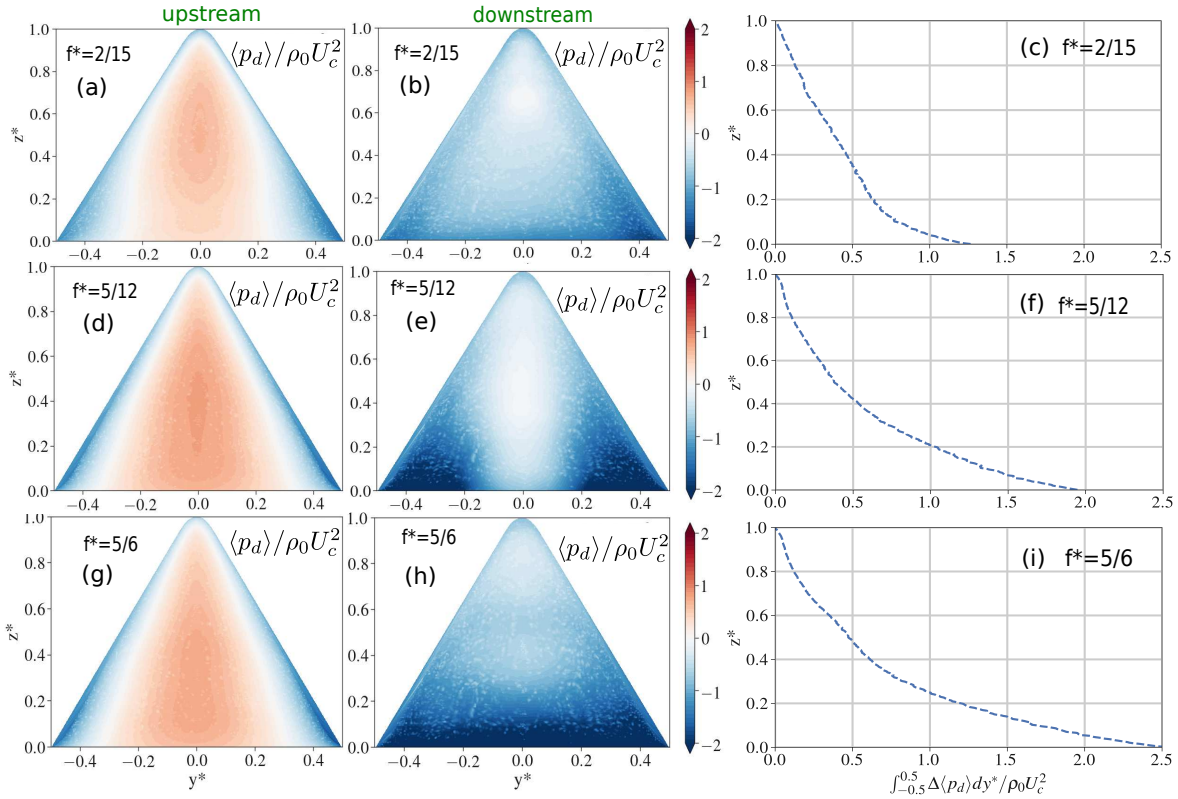

Figure 4.3: Distribution of mean pressure ($\langle p_d \rangle / \rho_0 U_c^2$) on the upstream and downstream faces of the topography : (a,b) $f^* = 2/15$, (d,e) $f^* = 5/12$ and (g,h) $f^* = 5/6$. The difference between upstream and downstream normalized pressure ($\Delta\langle p_d \rangle / \rho_0 U_c^2$) is integrated along y^* and plotted in the last column for each case: (c) $f^* = 2/15$, (f) $f^* = 5/12$ and (i) $f^* = 5/6$.

4.4.1 Mean pressure distribution

Figure 4.2(a,c,e,g) show qualitative differences in the vortex shedding patterns amongst the cases $f^* = \infty, 2/15, 5/12$ and 5/6. On the right (fig. 4.2b,d,f,h) the contours of mean dynamic pressure field are plotted. For $f^* = \infty$, shear layers elongate and separate from each side, rolling up into two attached vortices of opposite sign in the lee. With time, the attached eddies start to oscillate and eventually break off alternately to form the vortex street in fig. 4.2a. The eddy which remains attached briefly, possesses a low pressure core which decays radially outward from the vortex center (not shown). The near-wake vertical vorticity values are as large as $20f$, which is in agreement with observations of high Ro_c wakes (Chang et al., 2019; MacKinnon et al., 2019).

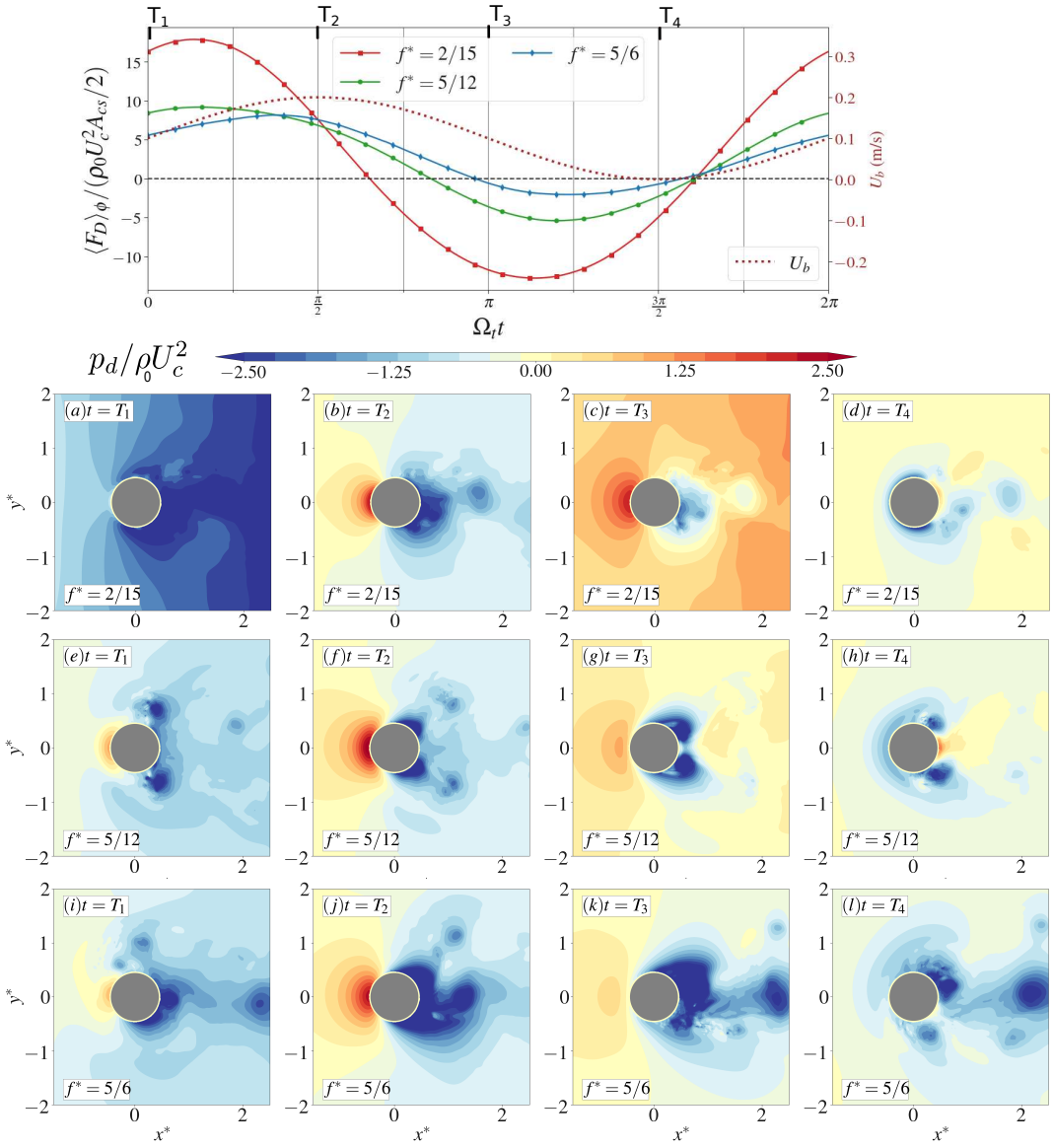

Figure 4.4: Header: Variation of normalized phase-averaged drag force ($\langle F \rangle_\phi$) with tidal phase $\Omega_t t$, plotted for $f^* = 2/15, 5/12$ and 5/6 cases. The barotropic velocity U_b is represented by the dotted line in the header. The instantaneous contours of dynamic pressure p_d are shown at four phases T_1, T_2, T_3 and T_4 (marked on the header) for cases $f^* = 2/15 (a-d), f^* = 5/12 (e-h)$ and $f^* = 5/6 (i-l)$ at $z^* = 0.02$. The projection of obstacle area in the streamwise direction is denoted as A_{cs}.

When $f^* = 2/15$, the lateral elongated shear layers are absent (fig. 4.2c). Instead, at this instant, the anticyclonic (negative ω_z) vortex remains attached to the obstacle as the cyclonic (positive ω_z) vortex moves into the wake (see VortXY_JPO_fstar_2_15.mov). The

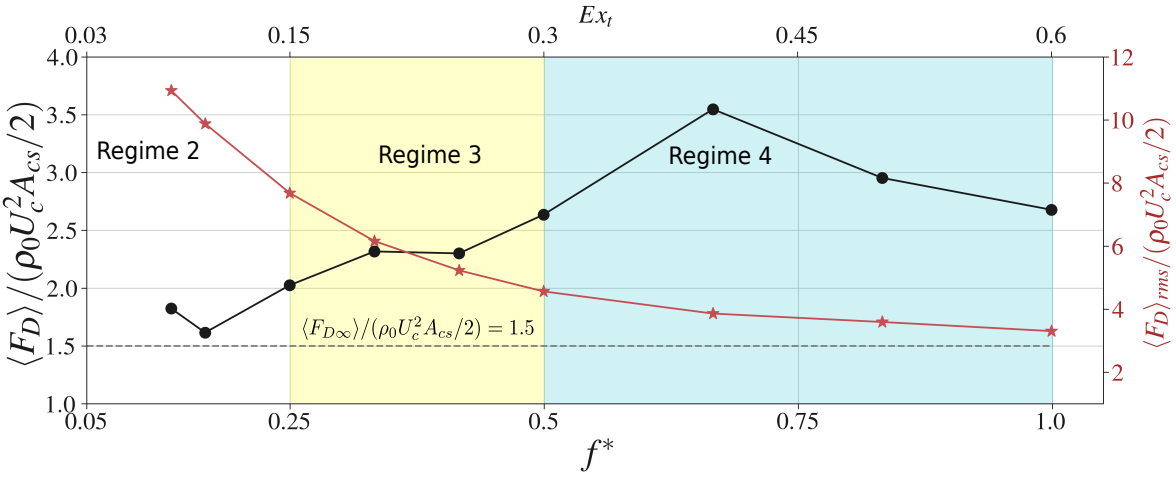

Figure 4.5: Variation of mean drag force ($\langle F_D\rangle$) and its root-mean-squared value ($\langle F_D\rangle_{rms}$) with f^*. The gray-dashed line denotes the normalised mean drag in the $f^* = \infty$ (no-tide) case (represented as $\langle F_{D\infty}\rangle$).

anticyclonic vortex grows in size from repeated small pulses of vorticity (green box) created every tidal cycle. These pulses form on the lateral sides of the obstacle at the location of flow separation. The attached vortex is shed at a slower frequency of $f_{s,c}$ (Puthan et al., 2021b). Since $f_t \approx 7.5 f_{s,c}$, the eddy remains attached while its circulation increases as the small pulses coalesce over 7.5 tidal cycles. Beyond $x^* = 1$, the staggered arrangement of vortices resembles a Kármán vortex street. The magnitude of mean dynamic pressure $\langle p_d\rangle$ is similar between the $f^* = \infty$ and $2/15$ cases (fig. 4.2b,d). A key difference with respect to the $f^* = \infty$ case is the presence of low pressure regions on the lateral sides of the obstacle in $f^* = 2/15$ (fig. 4.2d), created by these vortex pulses.

The organization of vertical vorticity (ω_z) and mean pressure ($\langle p_d\rangle$) for $f^* = 5/12$ and 5/6 are strikingly different from a Kármán vortex street generated by a steady current. At $f^* = 5/12$, a symmetric arrangement of vortices is present in the near wake, attached to the obstacle (fig. 4.2e). However this configuration is not stable and gives way to a distorted antisymmetric pattern of vortex fragments farther downstream. The timing of symmetric twin vortices is phase locked to the barotropic flow, elucidated further in section 4.5.2.

Figure 4.2g provides a snapshot of wake when $f^* = 5/6$. The cyclonic vortex remains

attached to the obstacle lee at this instant and grows in size during the tidal acceleration phase. Contours of mean pressure reveal regions of large pressure drop in the lee for the $f^* = 5/12$ and $f^* = 5/6$ cases (fig. 4.2f,h). For $f^* = 5/12$, two laterally offset low pressure zones lie symmetrically with respect to $y^* = 0$ while for $f^* = 5/6$, the low pressure region extends to cover the entire rear of the obstacle ($x^* > 0$). To discern the pressure anomalies along the vertical extent of the obstacle, the distribution of mean pressure field $\langle p_d \rangle$ *on* the hill is plotted in fig. 4.3.

Figure 4.3(a,d,g) and fig. 4.3(b,e,h) show the pressure distribution on the upstream and downstream faces of the obstacle, respectively. Each row in fig. 4.3 corresponds to a different case. The panels of fig. 4.3(c,f,i) contrast the difference between the upstream and downstream pressure values ($\Delta\langle p_d \rangle$) integrated along y^* among the three cases. The distribution of pressure on the upstream face is similar in all three tidally modulated cases. However, the differences in flow separation change the pressure distribution on the downstream face. The eddy shed from the obstacle has a larger horizontal length scale at the boundary as f^* increases. This forced eddy is characterized by the presence of a low pressure core.

In all cases, $\Delta\langle p_d \rangle$ is bottom intensified. In their steady-current simulations, MacCready and Pawlak (2001) noted "a tendency for drag on the lower half of the ridge to be greater than that on the upper half". In the present tidally modulated cases, the bottom intensification progressively increases from $f^* = 2/15$ to $5/6$. For example, consider the laterally integrated mean pressure at height $z^* = 0.2$ (fig. 4.3c,f,i). Its value increases from 0.6 at $f^* = 2/15$ to 1 at $f^* = 5/12$. For the $f^* = 5/6$ case (fig. 4.3h,i), the near-bottom integrated $\Delta\langle p_d \rangle$ is up to five times larger than its value at $z^* = 0.5$. A similar bottom-intensified pressure difference is also observed for $f^* = 5/12$, though for this case it is confined to the lateral sides of the abyssal hill (fig. 4.3e,f). Even for $f^* = 2/15$ (fig. 4.3b,c), a twofold increase in pressure drop is observed near the bottom relative to the upper half of the obstacle.

The eddy shedding (fig. 4.2) and pressure anomalies (fig. 4.3) in the $f^* = 2/15$, 5/12 and 5/6 cases are characteristic of the regimes 2, 3 and 4 which they represent. An examination of the pressure variability within a tidal cycle is the next step towards revealing the underlying mechanisms governing enhancement of drag at the obstacle base.

Figure 4.4 shows snapshots of instantaneous normalized pressure $p_d/\rho_0 U_c^2$ in the horizontal plane $z^* = 0.02$ (close to the bottom boundary) for $f^* = 2/15$, 5/12 and 5/6 cases. Four time instants T_1, T_2, T_3 and T_4 are chosen at tidal phases $\Omega_t t = 0, \pi/2, \pi$ and $3\pi/2$, respectively, for the snapshots. The variation of the phase-averaged form drag $\langle F_D \rangle_\phi$ and the barotropic current U_b are plotted in the header.

Consider the case $f^* = 5/6$ (from regime 4). At $t = T_1$, the accelerating fluid impinges on the obstacle, creating high pressure upstream and a low pressure zone downstream (fig. 4.4i). Owing to the asymmetry in flow separation, the low pressure region is dominant between $y^* = -0.5$ and 0. As the barotropic velocity increases, the region of low pressure enlarges downstream in fig. 4.4j, associated with the lee eddy formation illustrated in fig. 4.2g. The simultaneous increase in upstream pressure heightens the pressure anomaly between the fore and lee. As the barotropic flow decelerates between T_2 and T_3, the upstream pressure recedes concomitantly while the low pressure in the lee is sustained at $t = T_3$ (fig. 4.4k). The lee eddy remains attached at this instant preserving the low pressure zone. The low pressure region continues to exist at the downstream face between $y^* = 0$ to 0.5 at T_4 (fig. 4.4l). With the formation of persistent anticyclonic and cyclonic vortices on opposite sides during successive tidal cycles, the low pressure in the lee is maintained, albeit subject to lateral oscillations (see Pressure_JPO_fstar_5_6.mov). The outcome is an elevated mean drag.

For case $f^* = 5/12$, the pressure drop downstream of the obstacle is symmetric owing to the nature of the vortex shedding for this case. The low pressure region begins to form immediately after the lateral separation of the eddies at $t = T_1$ on both sides of the obstacle lee (fig. 4.4f). While the barotropic current remains above its mean value U_c between $t = T_1$

and T_3, the vortices continue to grow larger on either side of the hill (elaborated further in section 4.5 and fig. 4.7). The pressure drop across the hill increases concurrently in fig. 4.4f and fig. 4.4g. At the zero velocity phase ($t = T_4$), the recirculating fluid at low pressure accelerates upstream relative to the barotropic flow. A region of positive dynamic pressure (fig. 4.4h) is identified at this instant near $x^* = 0.5$ and $y^* = 0$, while the pressure upstream at the obstacle centerplane ($x^* = -0.5$ and $y^* = 0$) drops below zero momentarily. The eddy-induced low pressure zone remains attached at $x^*, y^* = (0.5, \pm 0.5)$. This configuration is reset to fig. 4.4e as the background flow gains momentum in the next cycle.

The instantaneous dynamic pressure p_d has contributions from two sources: the added mass and flow separation (see eq. (4.3)). When the tidal frequency is larger, the added mass component increases owing to its dependence on the tidal acceleration magnitude $U_t \Omega_t$. This is likely to occur when $f^* = 2/15$ as corroborated by normalised p_d in fig. 4.4a-d. At T_1, the tidal acceleration reaches its maximum value and the dynamic pressure $p_d/\rho_0 U_c^2$ drops below -2.5 over a large region in the obstacle lee (fig. 4.4a). Similarly, at the phase of maximum tidal deceleration ($t = T_3$), $p_d/\rho_0 U_c^2$ exceeds 2.5 over a large region upstream of the obstacle (fig. 4.4c). At instances of zero acceleration ($t = T_2$ and T_4), the dynamic pressure is purely associated with flow separation. At T_2, the low pressure region in the lee (fig. 4.4b) is generated due to the attached eddy in fig. 4.2c, while the high p_d upstream is generated by the impinging current. On the contrary, at T_4, the pressure anomalies in the obstacle centerplane are marginal (fig. 4.4d). At the lateral sides of the obstacle, a weak pressure drop is observed, attributed to the vortex pulses discussed earlier. The tidal period is smaller than the natural eddy shedding time scale by a factor of 7.5 for this case. This constrains the size of the attached eddy to a small vortex pulse, which has a correspondingly weak effect on the pressure drop.

The temporal variability of p_d directly affects the variation in form drag as illustrated by the phase-averaged form drag $\langle F_D \rangle_\phi$ in the header of fig. 4.4. The form drag exhibits large modulation in the $f^* = 2/15$ case. Also, the phase difference between $\langle F_D \rangle_\phi$ and U_b

exceeds $\pi/4$. Recall that the inertial drag has a phase difference of $\pi/2$ with U_b. Therefore, it is possible that instantaneous inertial drag contributions are important in this case. To confirm this, we follow the procedure of Warner and MacCready (2009) to estimate the ratio of inertial drag to separation drag for our obstacle geometry. We assume that the magnitude of F_D^S is equal to the bluff-body drag estimate of $\rho_0 A_{cs} U_c^2/2$ and that $C_a = 1$ in eq. (4.4) (for explanation, see pg. 2979 of Warner and MacCready (2009)). For the conical obstacle, and taking $R = U_t/U_c = 1$,

$$\frac{|F_D^I|}{|F_D^S|} = \frac{2\pi}{3Ex_t} \approx \frac{3.5}{f^*}, \tag{4.7}$$

where the second equality follows from $f^* = 1.66Ex_t$ from section 4.1. As f^* increases, the inertial component of form drag decreases. Separation drag becomes more prominent relative to inertial drag. This makes sense because at larger $f^* = f_{s,c}/f_t$, the tidal acceleration is weaker which causes the magnitude of inertial drag to decrease. Thus the phase difference between $\langle F_D \rangle_\phi$ and U_b is smaller than $\pi/2$ in $f^* = 5/12$ and 5/6.

4.4.2 States of high drag

From the preceding text, it is clear that the pressure anomalies on the obstacle change significantly owing to tidal oscillations. Here we demonstrate that tidal oscillations lead to high levels of instantaneous and mean drag. The ratio of inertial drag to separation drag is inversely related to f^* as shown in eq. (4.7). It varies from a value of approximately 4 at $f^* = 5/6$ to 25 at $f^* = 2/15$. Clearly the contribution of inertial drag exceeds the separation drag within the tidal cycle, especially for low f^* cases. Figure 4.4 showed that normalised $\langle F_D \rangle_\phi$ in $f^* = 2/15$ reached values of up to 16 during the tidal cycle just after $t = T_1$ and dropped rapidly below -10 near T_3. On the other hand, $\langle F_D \rangle_\phi$ has a smaller variance over the tidal cycle in $f^* = 5/12$ and 5/6. In these two cases, large eddy cores in the lee generate zones

of low pressure with high magnitude which remain at the obstacle periphery throughout the tidal cycle (fig. 4.4e-l). The longer residence time of the attached low pressure zone enhances the separation drag F_D^S. The deviation of $\langle F_D \rangle_\phi$ from its mean value is also much smaller. The values of $\langle F_D \rangle_\phi$ lie between -5 and 8 for this case.

Quantifying the mean and RMS values of F_D is key in this comparative analysis. The time averaged value, namely $\langle F_D \rangle$, offers a diagnosis of high-drag states by nearly eliminating the contribution from inertial drag and providing an estimate of the separation drag F_D^S. Parametrization of separation drag is important owing to its ability to extract energy from the flow. To this end, the normalized $\langle F_D \rangle$ and $\langle F_D \rangle_{rms}$ are plotted in fig. 4.5 as a function of f^*. The normalized form drag or the drag coefficient is $\langle F_D \rangle / (\rho_0 U_c^2 A_{cs}/2)$ where A_{cs} is the projected obstacle area in the streamwise direction. The value of form drag coefficient in the $f^* = \infty$ case is 1.5. In the tidally modulated cases, the mean form drag coefficient generally increases with increasing f^*. The larger size and longer residence time of the attached wake eddy contribute to the intensification of the pressure drop and its sustenance near the foot of the abyssal hill (fig. 4.3h,i). As a result, a large increase in $\langle F_D \rangle$ (relative to $\langle F_{D\infty} \rangle$). is observed in regimes 3 and 4. The mean drag coefficient exceeds 3.5 in regime 4, and its average value is 3, signifying a two-fold increase in form drag with respect to the steady case in regime 1. In regime 3, there is a 60% increase in average form drag relative to $\langle F_{D\infty} \rangle$. In comparison, only a marginal increase of $\langle F_D \rangle$ is seen in regime 2. On the other hand, the RMS drag, $\langle F_D \rangle_{rms}$ is strongly influenced by inertial forces. The RMS drag decays rapidly as f^* increases, from a large value of 11 at $f^* = 2/15$ to 3.2 at $f^* = 1$. This monotonic decay is attributed to a reduction in the inertial drag associated with the tidal acceleration.

To ascertain the magnitude of form drag relative to the drag associated with the frictional bottom boundary layer (BBL), consider regime 4. The mean form drag $\langle F_{D\infty} \rangle = 3\rho_0 U_c^2 A_{cs}/2$. Assuming a coefficient of bottom friction (C_f) of approximately 0.002 based on previous studies (e.g. McCabe et al., 2006), the mean frictional drag ($\langle F^{BBL} \rangle$) is of the order

$C_f \rho_0 U_c^2 A_b/2$, where A_b is the projected area of the hill on the horizontal plane. Therefore, the ratio of mean form drag to frictional drag is

$$\frac{\langle F_{D\infty} \rangle}{\langle F^{BBL} \rangle} = \frac{3A_{cs}}{C_f A_b} \approx 300 \tag{4.8}$$

Therefore, it is important to account for the form drag of 3D underwater obstacles when parametrising bottom drag, especially when tidal oscillations are present. The interplay between form drag and spatio-temporal organisation of the lee eddies deserves attention. To this end, vortex dynamics are explored in the next section.

4.5 Vortex dynamics

Investigations of cylinder wakes created by homogeneous non-rotating flow, have often been used to add to our understanding of vortex dynamics in oceanic wakes (Chang et al., 2019). However, density stratification and planetary rotation influence the wake significantly. For example, Lin and Pao (1979) presented a detailed review of internal wave radiation and the emergence of thin lee vortices when $Fr_c < 1$. With the addition of rotation, Dong et al. (2006) showed manifestations of barotropic, baroclinic and centrifugal instabilities in the wake. The recent study of Puthan et al. (2021b) showed that vortices in the far wake occur at frequencies coinciding with tidal subharmonics. Form drag is directly related to flow separation and near wake vortices. We discuss these facets and also the vertical organization of lee vortices in this section.

4.5.1 Vertical structure of lee vortices

Figure 4.6a,c show contours of ω_z on horizontal planes at four different heights in the wake for $f^* = 5/12$ (regime 3) and 5/6 (regime 4). Velocity spectra at spatial probes chosen

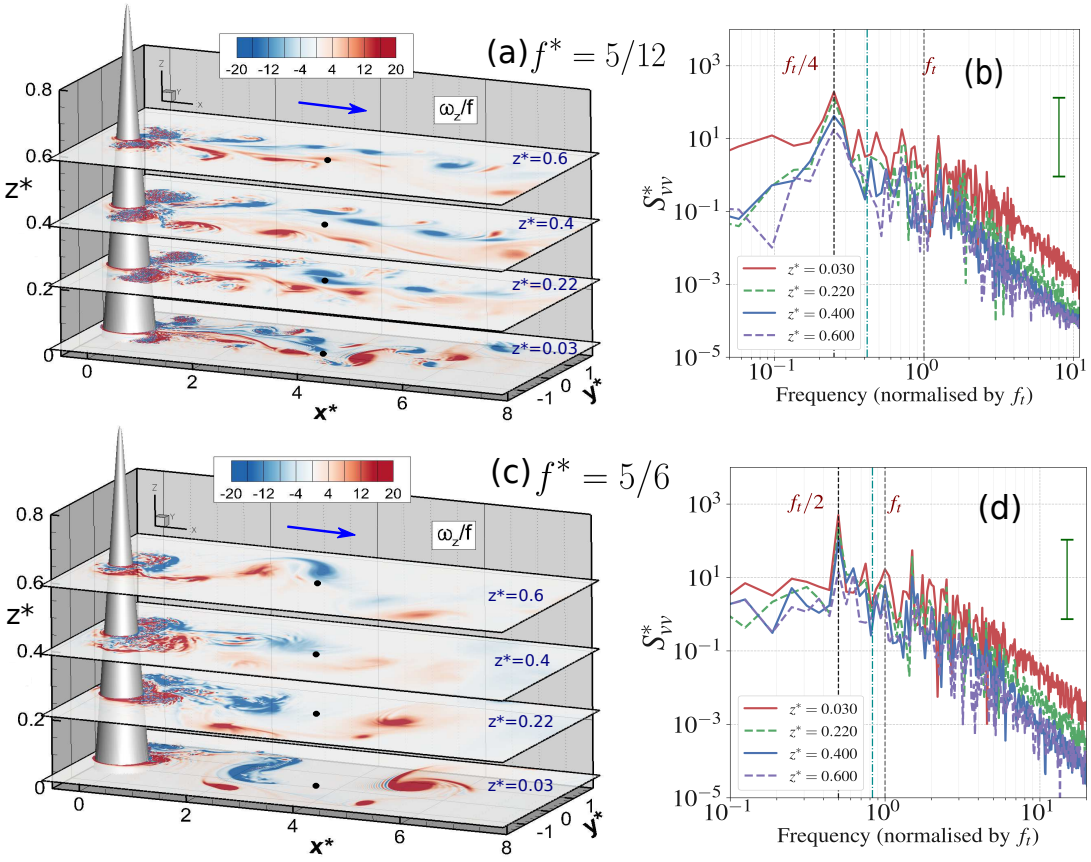

Figure 4.6: Eddy formation is depicted by the normalized vertical vorticity (ω_z/f) in four horizontal (x-y) planes : (a) $f^* = 5/12$ and (c)$f^* = 5/6$. (b,d) Spectra of spanwise velocity $S^*_{vv} = S_{vv}/U_c^2$, plotted at four probes (black dots in a,c respectively) chosen at different vertical heights located at $x^* = 4$ and $y^* = 0$. The green bar in (b,d) shows the 95% confidence interval of the spectrum.

at these vertical heights are shown in fig. 4.6b,d. Let $z^*_{div} \approx 1 - (U_c + U_t)/Nh = 0.7$ be an approximate estimate of the dividing vertical height, below which the fluid is driven laterally around the obstacle (Sheppard, 1956; Drazin, 1961). The four vertical heights in fig. 4.6 are chosen such that $z^* < z^*_{div}$.

For $f^* = 5/12$ (fig. 4.6a), laterally symmetric dipoles, attached to the obstacle, form along its vertical extent. Farther in the wake beyond $x^* = 2$, discrete eddies remain scattered and disorganized. At this stage, these eddies do not exhibit the spatial configuration of a Kármán vortex street.

For the case of $f^* = 5/6$ (fig. 4.6c), the coherent vortices are larger and their shedding is asymmetrical. A region of both negative and positive vorticity remains attached to the topography along its vertical extent. Beyond $x^* = 1$, a large cyclonic (positive) vortex is followed by a large anticyclonic (negative) vortex at $z^* = 0.03$ and 0.22. These two vortices are found to be aligned vertically up to a height of $O(U_t/N)$. Similar aligned vortices were also observed in the $f^* = 5/12$ case, albeit smaller in diameter and more scattered. A possible explanation may stem from the vortex separation being initiated by the tidal forcing. To illustrate this, the spectra of spanwise velocity (S^*_{vv}) are plotted at different vertical heights for $f^* = 5/12$ and $f^* = 5/6$ cases in fig. 4.6b,d. The frequency of lateral oscillations from S^*_{vv} is used to ascertain the vortex shedding frequency. Vortices are shed at the same instant during the tidal cycle along the vertical extent of the obstacle (not shown). In addition, in the far wake at $z^* < z^*_{div}$, the vortices are observed at a uniform frequency of $f_t/4$ in $f^* = 5/12$ case and $f_t/2$ in $f^* = 5/6$ case. The timing of the flow separation may help align the vortices along the z direction up to a vertical length scale permitted by the background stratification. At elevations above z^*_{div}, the transient lee waves interfere strongly with the coherent structures in the wake (see Puthan et al., 2020). Near wake turbulence creates small-scale patches of vorticity in both cases, up to two diameters away from the obstacle. However, we emphasize that their instantaneous presentation is qualitatively different from a classical Kármán vortex street over the vertical extent of the hill.

4.5.2 Symmetric eddy dipoles

The symmetric twin dipoles shown previously in fig. 4.2e are created through a sequence of events presented in fig. 4.7. A locally adverse streamwise pressure gradient (shown in fig. 4.4e,f) develops on either lateral side of the obstacle. While the barotropic flow remains positive, as in fig. 4.7a, two opposite-signed vortices form in the recirculation zone and grow in size until the velocity approaches zero. As the tide-associated pressure

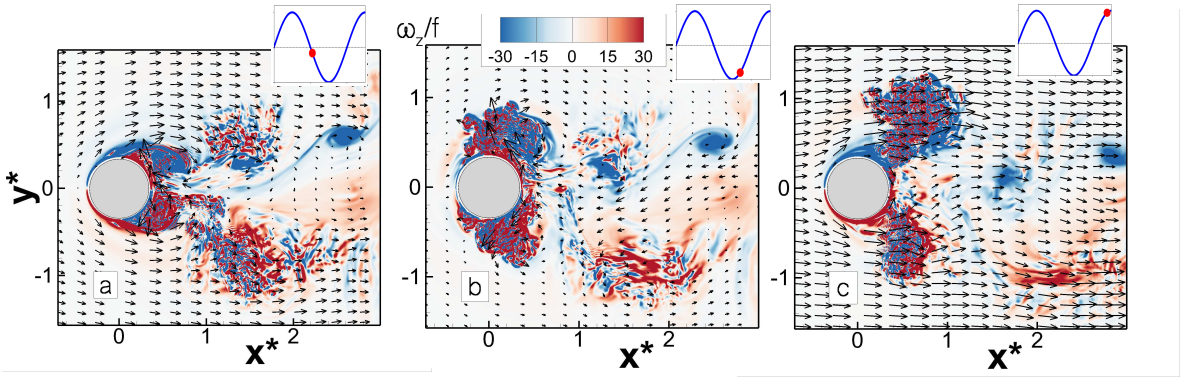

Figure 4.7: Normalized vertical vorticity (ω_z/f) at three different phases of a tidally perturbed wake at $f^* = 5/12$: (a) $t/T = 18.52$, (b)$t/T = 18.85$ and (c) $t/T = 19.19$.

gradient changes sign at the zero velocity phase, the high vorticity fluid accelerates upstream relative to the background flow on both lateral sides. During this event, additional vorticity of opposite sign is generated from shear when this fluid is near the obstacle. For example, the attached anticyclonic eddy in fig. 4.7a accrues positive vorticity in fig. 4.7b during its deflection to the $+y$ direction. Thus twin dipoles form symmetrically on either lateral side of the obstacle. During the subsequent acceleration phase, the dipoles gain enough momentum to advect downstream (fig. 4.7c). At the same instant, a new vortex pair starts to grow near the separation points, completing a full cycle of oscillation.

The formation of the symmetric vortices are phase locked to the tidal cycle. Note that the positive vorticity generated by the upstream flow (directed to the $+y$ direction) in the previous tidal cycle (located at $x^*, y^* = 1.5, 0.5$) in fig. 4.7a, decays in the present tidal cycle, as shown in fig. 4.7b,c. The vortices also lose their lateral symmetry beyond $x^* = 1.5$. Tidal forcing aids in the symmetrical placement of vortices up to an excursion distance of U_t/f_t, or equivalently, $x^* = 1.57$ for this case. Beyond $x^* = 1.57$, a staggered and distorted pattern of vortices occurs (see fig. 4.2e). Deviation of the wake vortex frequency f_s from the tidal frequency f_t occurs in this region, as elaborated in the next section.

4.5.3 Temporal variation of vorticity

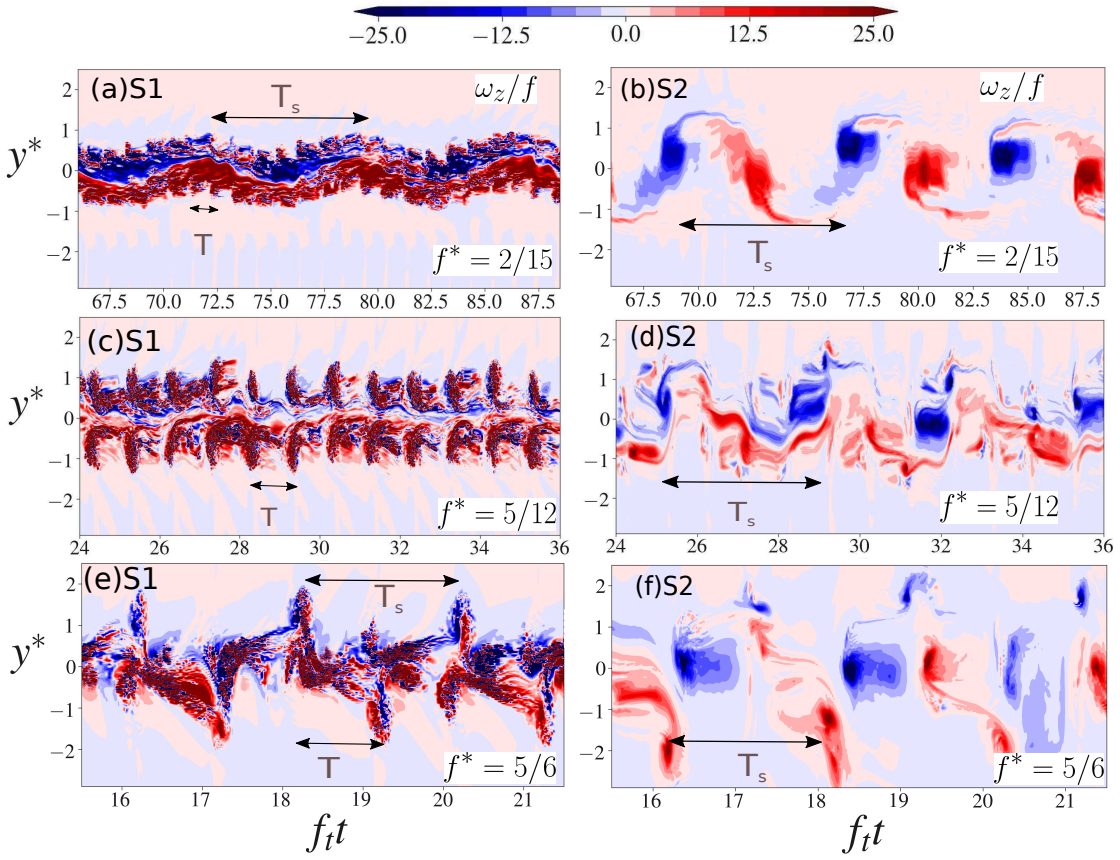

Figure 4.8: Time evolution of vertical vorticity (ω_z/f) is depicted by a $y-t$ Hovmöller diagram, at stations S1 (at $x^*, z^* = 1, 0.25$) and S2 (at $x^*, z^* = 4, 0.25$) for three cases : (a,b) $f^* = 2/15$, (c,d) $f^* = 5/12$ and (e,f) $f^* = 5/6$. Here, T is the tidal period and T_s is the time period of far wake vortices. Note that the range of $f_t t$ decreases from the top to the bottom row. The stations S1 and S2 are indicated by brown dashed lines in fig. 4.2.

Hovmöller diagrams of normalized vorticity in fig. 4.8 demonstrate clearly that transitions of the vortex frequency vary from the near to the far wake between regimes 2 to 4. Space-time ($y-t$) contours of vertical vorticity are plotted at two stations: S1 in the near wake and S2 in the far wake (see dashed lines in fig. 4.2c,e,g). In fig. 4.8a, the signature of the tidal frequency is observed in the vortex pulses spaced over one tidal period (T) for $f^* = 2/15$. These pulses are arranged in the form of a slowly varying large-scale sinuous (antisymmetric) mode. The sinuous mode evolves into a row of opposite-signed vortices at S2 (fig. 4.8b). The

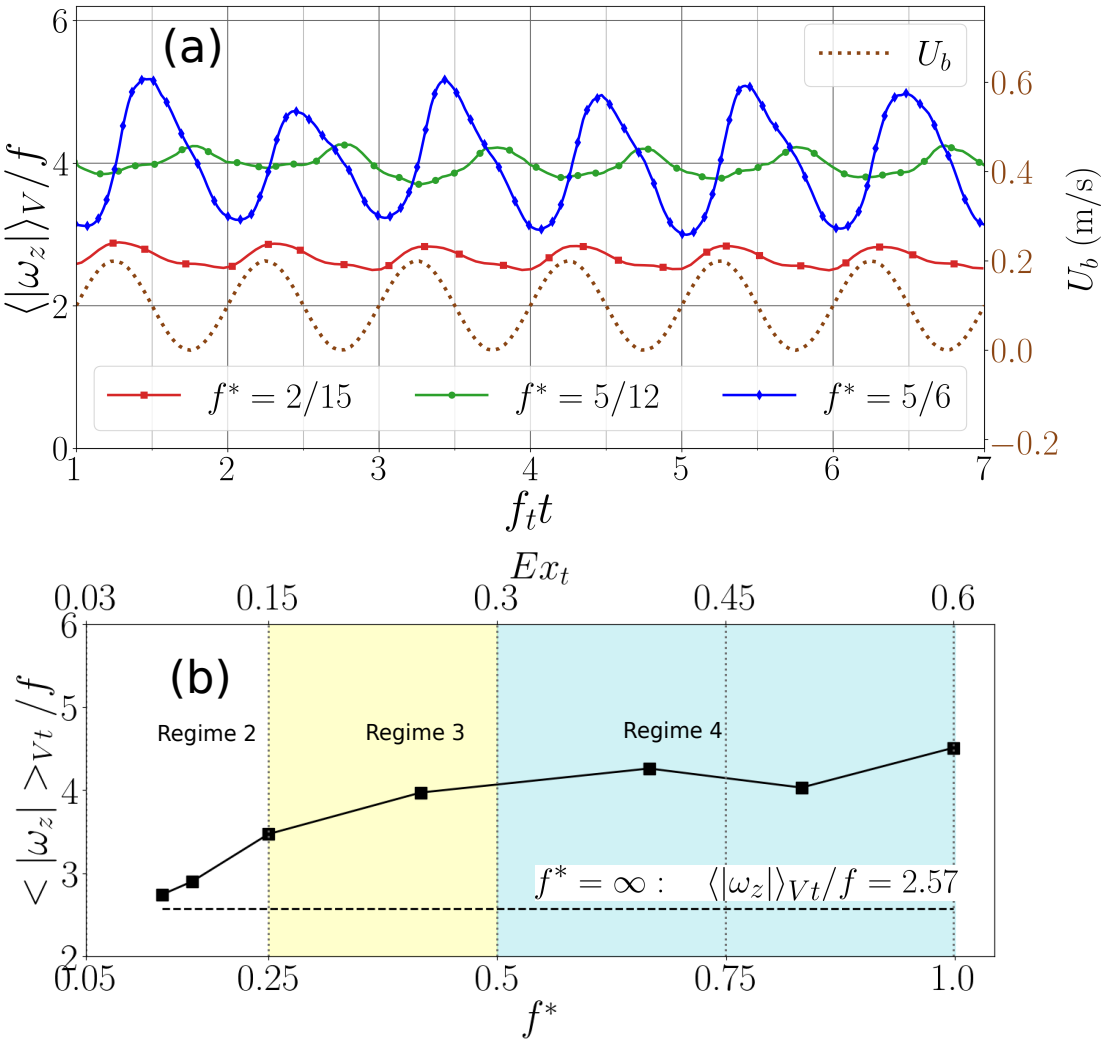

Figure 4.9: (a) Volume-averaged vertical vorticity $\langle|\omega_z|\rangle_V = \int_0^V |\omega_z| dV/V$ plotted as a function of time for $f^* = 2/15, 5/12$ and 5/6 cases. (b) Variation of time averaged $\langle|\omega_z|\rangle_V$ shown as a function of f^*.

signature of the individual vortex pulses disappears at S2 leaving large-scale coherent vortices separated by the time period, T_s. The vortex period (T_s) in the far wake aligns with the natural shedding period of the obstacle wake, $T_{s,c}$.

Case $f^* = 5/12$ exhibits a laterally symmetric vortex pattern at S1, depicted in fig. 4.8c. These vortex structures repeat every tidal cycle. The unstable symmetric mode transitions into an antisymmetric downstream wake made up of coherent vortices in fig. 4.8d. These vortices are separated by $T_s = 4T$, demonstrating the tidal synchronization noted in Puthan

et al. (2021b). Thus the wake vortex frequency is modified to $f_t/4$. In other words, during every tidal cycle the symmetric vortices feed their vorticity into a larger vortex downstream, formed every four tidal cycles.

In the $f^* = 5/6$ case, the wake is strongly asymmetric in the lateral direction at S1 (fig. 4.8e). Large vortex lobes repeat once every two cycles and extend laterally. The lateral extent stretches farther at S2 relative to the previous two cases, as seen in fig. 4.8f. The wake width is as large as 4.5D (extending from $y^* \approx -2.5$ to $y^* \approx 2$), compared to $3D$ and $2.2D$ for $f^* = 5/12$ and $2/15$. A temporally distorted wake is observed at S2 in the $f^* = 5/6$ case, wherein the larger patches of negative vorticity are observed near the center while smaller vortices of same sign are laterally offset by approximately $2D$ from the centerplane. The space-time plot reveals thin filaments of positive vorticity in the temporal frame, in the far wake of $f^* = 5/12$ and 5/6 cases. The far wake eddy frequency coincides with $f_t/2$ for $f^* = 5/6$.

To explore the time evolution of eddy vorticity injected into the wake, the absolute value of ω_z is volume averaged over a domain encompassing the hill and extending to a distance of $8D$ into the wake. Figure 4.9a shows the temporal evolution of normalized volume-averaged vorticity $\langle|\omega_z|\rangle_V/f$. The dotted line shows the variation in the barotropic velocity. For the $f^* = 2/15$ case, $\langle|\omega_z|\rangle_V$ varies in phase with U_b. The pulses of vorticity which form during the maximum velocity phase of every tidal cycle are likely responsible for the small increases of $\langle|\omega_z|\rangle_V$ from its mean value. At $f^* = 5/12$, $\langle|\omega_z|\rangle_V$ increases at the low-velocity phase during every tidal cycle. During the shedding of symmetric vortices, the low velocity phase is accompanied by additional vorticity from shear layer roll-up at the obstacle (fig. 4.7). The result is an increase of $\langle|\omega_z|\rangle_V$ near the zero-velocity phase. On the other hand, larger variations from the mean occur in $\langle|\omega_z|\rangle_V$ values when $f^* = 5/6$.

Time averages of $\langle|\omega_z|\rangle_V/f$ are plotted over a range of f^* values in fig. 4.9b. Net vorticity added by the tides is not significant when f^* lies below 0.2 (fig. 4.9b). Above this

threshold, a gradual increase is noticed in $\langle|\omega_z|\rangle_{Vt}$ until it reaches a value of 4 at $f^* = 5/12$ and does not increase appreciably beyond that. This may be explained as follows. Over a tidal cycle, high vorticity fluid in the obstacle vicinity is advected by a distance of U_cT. This fluid migrates into the wake permanently if U_cT exceeds $O(D)$. In other words, the tidal flow adds vorticity to the wake when $U_cT/D > O(1)$. Simplifying using the relation $f^* = 1.66Ex_t$ (from section 4.1) this condition is equivalent to $f^* > O(0.25)$. At larger $f^* = f_{s,c}/f_t$, the vortices have sufficient time to separate from the obstacle before the deceleration of barotropic current.

4.6 Discussion and conclusions

LES were undertaken to examine the wake created by a stratified tidally modulated flow (U_b) in the presence of weak background rotation. The barotropic flow U_b has a mean component U_c, and a tidal component U_t of equal strength. Since the Froude number Fr_c is small, the near bottom flow is forced to separate laterally from the obstacle. As a result, coherent eddies of the nature observed in the ocean (e.g Pawlak et al., 2003; MacKinnon et al., 2019), form in the lee. We find that the flow exhibits four regimes, based on vortex patterns, as summarized in table 4.1. In the first regime where tides are absent, lee vortices separate from the obstacle at a constant frequency $f_{s,c}$ and form a Kármán vortex street downstream. In the next three regimes, the arrangement of vortices is altered by the tidal flow. Changes in flow separation, accompanied by bottom-intensified pressure differences on the obstacle, are responsible for states of high drag in the tidally modulated cases, especially regime 4. The effect of tidal oscillations is characterized by varying the relative frequency parameter ($f^* = f_{s,c}/f_t$) from $1/10$ to 1. Three of the nine cases are chosen, namely, $f^* = 2/15, 5/12$ and $5/6$ from regimes 2, 3 and 4, respectively, to illustrate the results. At $f^* = 2/15$ (regime 2), vortex pulses which occur every tidal cycle, feed vorticity into a larger eddy in the recirculation zone. These larger eddies form a Kármán vortex wake downstream. At $f^* = 5/12$ (regime 3),

laterally symmetric eddy dipoles are shed in the near wake. The lateral symmetry is controlled by the tidal flow up to a streamwise distance of U_t/f_t. Beyond this location, the vortices partially break down or merge to create a disorganized wake downstream. This event is accompanied by a change in the wake vortex frequency from f_t to $f_t/4$. At $f^* = 5/6$ (regime 4), strong asymmetric shedding at a frequency of $f_t/2$ is observed in the entire wake. The wake is laterally wider in comparison to the other regimes.

The timing of the shed vortices is strongly influenced by the barotropic tidal oscillation. When $|\omega_z|$ is volume-averaged over the wake, its temporal variation is affected by the tidal oscillation. At $f^* = 2/15$, the temporal evolution is in phase with tides owing to the formation of vortex pulses. On the other hand, at $f^* = 5/12$, the temporal evolution is out of phase with the tidal oscillation. Excess vorticity is added to the wake from the lateral motion of recirculating fluid and the attendant shear-layer roll-up during the low-velocity phase. Changes in flow separation also lead to variations in pressure along the streamwise direction of the obstacle. The difference between the mean pressure field fore and aft of the hill ($\Delta\langle p_d \rangle$) is bottom intensified in cases $f^* = 5/12$ and 5/6. At $f^* = 5/12$, the intensification is laterally offset from the centerline due to the impinging of the recirculating fluid on the obstacle centerline near the zero-velocity phase.

The normalized form drag, i.e. drag coefficient, obtained by integrating the pressure field over the obstacle surface area, varies amongst these cases. Form drag has two components, namely, the inertial and the separation drag. The separation drag is the dissipative part of form drag. The mean drag (averaged over several cycles) which is associated with the separation drag (Sarpkaya, 2004; Warner and MacCready, 2009), generally increases with increasing f^*. The bottom intensified values of $\Delta\langle p_d \rangle$ (associated with large eddies) and the longer eddy residence time in the lee contribute to approximately a two-fold increase of mean drag coefficient in regime 4 relative to its value in the no-tide case. High drag states are also present in regime 3, wherein approximately a 60% increase is observed in mean drag coefficient

relative to the no-tide case. Therefore, for a continuous distribution of topographic scales in the abyssal ocean, obstacles with $1/4 \leq f^* \leq 1$ can preferentially remove momentum from the background tidally modulated flow. The inertial drag force (associated with the magnitude of tidal acceleration) is dominant in regime 2, causing large variance of form drag within the tidal cycle in the $f^* = 2/15$ case. Since the inertial component of drag decreases with increasing f^*, so does the RMS drag. The rapidly varying pressure gradient associated with tidal forcing in $f^* = 2/15$ restricts the size of the lee eddy and diminishes the pressure anomalies during the zero-velocity phase of the tidal cycle. This leads to lower mean form drag relative to regimes 3 and 4.

Warner and MacCready (2009) investigated a coastal headland in a purely tidal flow and did not find a significant effect of the excursion number (equivalently f^*) on separation drag. Deviations of the present findings (regarding excursion number effects) from their results may be attributed to a difference in geometry (submerged conical obstacle) or the presence of a mean current in this study. The drag coefficient associated with mean form drag normalized using the obstacle frontal area in regime 4 is 3. Converting this to a value based on the obstacle plan area, the drag coefficient takes a value of approximately 0.6, substantially larger than the drag coefficient associated with the frictional bottom boundary layer of $O(10^{-3})$ estimated in previous work (e.g. Dewey and Crawford, 1988). Thus, form drag owing to wakes of steep obstacles dominates frictional drag in tidally modulated currents.

Acknowledgments

This chapter, in part, is under consideration for publication and it may appear in *Journal of Physical Oceanography*. P. Puthan, S. Sarkar and G. Pawlak, High drag states in tidally distorted stratified wakes. The dissertation author is the primary investigator and author of this paper.

Chapter 5

Wake vortices and dissipation in tidally modulated abyssal hill wakes

Ocean flows are characterized by steady or low-frequency components along with oscillating components at tidal frequencies. In this chapter, LES simulations are employed to investigate the role of tidal modulations on vortex shedding and dissipation in the wake. The velocity ratio $R = U_t/U_c$ is varied from 0 to 1 by changing U_t, and Ω_t is chosen in the regime of tidal synchronization where previous studies report wake vortex frequency of $\Omega_t/2$. Simulation results show that frequency of shed vortices reduces gradually with increasing R, from its natural shedding frequency at $R = 0$ to $\Omega_t/2$ when $R = 0.2$. When R lies between 0.2 and 1, vortices are shed at $\Omega_t/2$. This process is controlled by the ratio of R and the excursion number, expressed as a tidal strength parameter $\overline{S}$. When $0.4 \leq \overline{S} \leq 2$, vortices are trapped in the wake during the tidal deceleration phase and hence do not have an opportunity to shed. This causes a single vortex shedding cycle to complete over two tidal cycles.

Elevated dissipation rates in the obstacle lee are observed in the shear layer, hydraulic jet region and the near wake. The regions of strong dissipation are spatially intermittent, with values exceeding $O(U_c^3/D)$ in the lee during the maximum velocity phase. At the crest of

the hill, the maximum velocity of the hydraulic jet varies linearly with $1+R$. The slope of this curve, known as velocity intensification factor (I), is 1.48. The maximum dissipation rate during the tidal cycle increases monotonically with increasing R in the lee of the hill. The normalized area-integrated dissipation rate in the hydraulic response region scales with the velocity ratio R as $E_0^*(1+R)^4$, where E_0^* is the normalized maximum dissipation rate in the absence of tidal oscillations. This parametrization works well in the regime of $0 \leq R \leq 1$, which governs a large fraction of realistic low Froude number geophysical wakes.

5.1 Introduction

Rough bottom topography in the abyssal ocean contributes significantly to the enhancement of drag and turbulent dissipation. Interaction of tidally modulated flows in the ocean with bottom topography leads to the generation of internal gravity waves (Sarkar and Scotti, 2017; Alford et al., 2011; Garrett and Kunze, 2007), lee waves (Legg, 2021; Cusack et al., 2017) and wake eddies (Signell and Geyer, 1991; Pawlak et al., 2003; Caldeira et al., 2005; MacKinnon et al., 2019; Zeiden et al., 2019). The baroclinic processes at the sites of internal wave generation are essential progenitors of dissipation and ocean mixing (Polzin et al., 1997; Ledwell et al., 2000; Wunsch and Ferrari, 2004). At steeper topographies such as the Hawaiian ridge (Aucan et al., 2006; Alford et al., 2014; Klymak et al., 2006) and Luzon Strait (Alford et al., 2011; Buijsman et al., 2012; Pinkel et al., 2012), there is direct wave breaking at the ridge with enhanced turbulence dissipation at the seafloor while at topographies with shallow slopes like Brazil Basin, wave-wave interactions cascade energy to high wave numbers and ultimately to turbulence (Laurent and Garrett, 2002). Recent measurements of MacKinnon et al. (2019) and Voet et al. (2020) show significant energy loss associated with vertically sheared wake eddies at the northern end of the Palau island chain. Although several numerical studies have quantified the dissipation associated with wave breaking and

wave-wave interactions, dissipation associated with wake eddies has not received sufficient attention.

Non-hydrostatic models are well known for their ability to capture reproduce non-linear mechanisms leading to turbulence cascade at energetic regions (e.g. Jalali and Sarkar, 2017). Simulations of three-dimensional (3D) topography with non-hydrostatic models are scant, e.g. Buijsman et al. (2014); King et al. (2009b). Numerical complications may arise while modeling multiscale topographies, adopting realistic background density profiles and employing intricate barotropic forcing in realistic scenarios, which makes 3D non-hydrostatic computations in realistic settings extremely expensive and impractical for studying the underlying mechanisms in-charge of baroclinic processes (Chalamalla et al., 2017). Therefore, flow simulations in idealized setups are important to understand and parameterize such processes. Turbulence resolving 3D simulations of idealized cases have been mainly limited to two-dimensional topography (Venayagamoorthy and Fringer, 2007; Jalali et al., 2014; Winters, 2015; Puthan et al., 2019) as pointed out by Lamb (2014); Sarkar and Scotti (2017).

In general, ocean flows are characterized by steady or low-frequency components along with oscillating components at tidal frequencies. Most numerical studies have focused on geophysical wake generated by either a steady current (Dietrich et al., 1996; Dong et al., 2006; Dong and McWilliams, 2007; MacCready and Pawlak, 2001; Perfect et al., 2020) or that generated by a pure-tidal flow (Signell and Geyer, 1991; Rapaka et al., 2013; Winters, 2015; Zhang et al., 2017; King et al., 2010; Jalali et al., 2017; King et al., 2009a; Holloway and Merrifield, 1999; Munroe and Lamb, 2005). Recent observations of stratified tidally-driven flow around islands (MacKinnon et al., 2019) and rough topographies (Girton et al., 2019) highlight the complex interactions between flow separation, topographically generated eddies and the internal waves. For example, Lamb and Dunphy (2018) and Shakespeare and Hogg (2019) reported interesting observations on changes in the momentum and energy fluxes of tidally forced internal waves in presence of a background current. Furthermore,

Warner and MacCready (2014) show that the dynamics around ridges that span both internal waves and eddy generation regimes are different from that of topographies which freely propagates internal waves. Ritchet et al. (2019) showed that mean current induced Doppler-shift of internal tide frequencies at critical latitude ($\sim 29^{\circ}$) caused a weaker enhancement of dissipation owing to parametric subharmonic instability (PSI). Recently Puthan et al. (2021b) performed a parametric study by varying the ratio between natural shedding frequency ($\Omega_{s,c}$) and tidal frequency (Ω_t) from 0.1 to 1 to illustrate the tidal synchronization of lee vortices behind a conical hill in a stratified flow. Thus it is evident that tidally modulated stratified flow over obstacles exhibits qualitative changes in internal wave energy flux, boundary layer turbulence and wake dynamics, relative to the classical case of steady flow past obstacles. In the ocean, tides and currents occur in conjunction. To examine the role of tides in flow separation and dissipation, we employ LES technique to simulate an oceanic wake past a conical hill generated by a tidally modulated flow. The conical hill has a height h of 150 m and base diameter D of 500 m. The background flow is $U_b = U_c + U_t \sin(\Omega_t t)$.

Eddy trains are often generated in the presence of strong mean flow. For example, in South China Sea, the magnitude of current can reach up to 0.5 m/s giving rise to a train of vortices (Yua et al., 2018). Intermittent eddy trains were also observed in the vicinity of Izu islands, generated by Kuroshio, the western boundary current in North Pacific (Isugachi et al., 2009; Liu and Chang, 2018), with eddy formation occurring during periods of stronger currents. To this end, we explore the regime of $U_t/U_c \leq 1$. The mean velocity U_c is fixed at 0.1 m/s while the tidal component U_t is varied from 0 to 0.1 m/s. For simplicity the ratio U_t/U_c is denoted as R, following the convention of Puthan et al. (2021b).

Other key elements that govern geophysical wakes are stratification (Hunt and Snyder, 1980; Perfect et al., 2020), rotation (Perfect et al., 2018; Srinivasan et al., 2018) and tidal forcing (Callendar et al., 2011; MacKinnon et al., 2019). These elements are influenced by three key non-dimensional variables, namely the topographic Froude number (Fr_c), the

Rossby number (Ro_c) and the excursion number (Ex_c). The topographic Froude number ($Fr_c = U_c/Nh$) governs the ability of a stratified flow to rise over the topography by navigating the energy barrier imposed by stratification. Here, N is the background buoyancy frequency. Most large scale ocean wakes are characterized by low Fr_c ($Fr_c \ll 1$) flows. Nonlinear effects such as upstream blocking (Winters and Armi, 2014), high mode internal waves (Klymak et al., 2010b) and enhanced turbulence downstream induced by lateral flow separation (Perfect et al., 2020; Buijsman et al., 2014) dominate in this regime.

The relative strength of the cyclonic and anticyclonic lee eddies is given by the Rossby number $Ro_c = U_c/fD$, where f is the inertial frequency. Observations of island wakes with length scales of $O(1\text{km})$ are characterized by high Rossby numbers ($Ro_c > 1$), especially near the equator (MacKinnon et al., 2019; Chang et al., 2019; Rudnick et al., 2019). The ratio of the barotropic tidal excursion to the topographic length, referred to as the excursion number, $Ex_c = U_c/\Omega_t D$ is also a measure of nonlinearity (Jalali et al., 2014; Rapaka et al., 2013). Longer excursion times provide enough time for the wake eddies to form before the tidal deceleration phase. Flows at $Ex_c \sim O(1)$ are common in the ocean (e.g. Musgrave et al., 2016) but beyond the purview of analytical models (Shakespeare and Hogg, 2019).

Tides play an important role in island wakes. Observations of Black and Gay (1987) showed formation of 'phase' eddies in the continental shelf of Great Barrier Reef. These eddies form at a specific phase during every tidal cycle. Denniss et al. (1995) and Chang et al. (2019) reported lee eddies shed past islands at the dominant tidal frequency. This phase-locking phenomenon, also referred to as tidal synchronization, was observed even when the tidal velocity amplitude is small relative to the mean flow. Simulations of Puthan et al. (2021b) demonstrate occurence of wake vortices at tidal subharmonics behind a conical hill at $Fr_c = 0.15$ and $R = 1$.

In this chapter, tidal synchronization is revisited in the context of varying strength of tidal oscillations. Specifically, the minimum value of U_t relative to U_c for onset of tidal

synchronization is of interest. In order to capture the physics of a class of flows in the ocean, tidal forcing in the presence of weak rotation and strong stratification is considered. Specifically, values of Ro_c, Fr_c and Ex_c are fixed at 5.5, 0.15 and 0.5 respectively, while the velocity ratio R is varied from 0 to 1. The results in section 5.3 are divided into two related topics. Firstly, the onset of tidal synchronization shall be explored in section 5.3.1. In section 5.3.2 and section 5.3.3, the key local dissipation hot-spots are discussed with focus on energy loss in the wake, intensification of velocity at the hydraulic jump and dissipation induced by the hydraulic jet. A simple parametrization for maximum dissipation rate in the hydraulic jump is proposed in section 5.3.3.

5.2 Theory

Consider the wake generated by a barotropic current of the form $U_c + U_t \sin(\Omega_t t)$ in an environment with rotation rate f and constant background buoyancy frequency N. The momentum equation is given as follows (Puthan et al., 2021b) :

$$\frac{\partial u_m}{\partial t} + \frac{\partial (u_n u_m)}{\partial x_n} - f\varepsilon_{mn3}(u_n - U_b\delta_{n1}) = -\frac{1}{\rho_0}\frac{\partial p}{\partial x_m} + U_t\Omega_t \cos(\Omega_t t)\delta_{m1} - \frac{g\rho'}{\rho_0}\delta_{m3} + \frac{\partial \tau_{mn}}{\partial x_n}, \tag{5.1}$$

When velocity ratio R is less than 1, U_c is assumed to be the dominant velocity scale and eq. (5.1) can be re-written in its non-dimensional form as :

$$\frac{\partial u_m^*}{\partial t^*} + \frac{\partial (u_n^* u_m^*)}{\partial x_n^*} - \frac{\varepsilon_{mn3}}{Ro_c}\left(1 - \frac{U_b}{U_c}\delta_{n1}\right) = -\frac{\partial p^*}{\partial x_m^*} + \frac{R}{Ex_c}\cos\left(\frac{t^*}{Ex_c}\right)\delta_{m1} - \frac{\rho^*}{Fr_c^2(h/D)}\delta_{m3} + \frac{1}{Re_c}\frac{\partial \tau_{mn}^*}{\partial x_n^*}, \tag{5.2}$$

The parameters in equations (5.1) and (5.2) are defined in table 5.1. The tidal forcing term in eq. (5.1) does not vary in space. Therefore, it does not add vorticity to the flow. However,

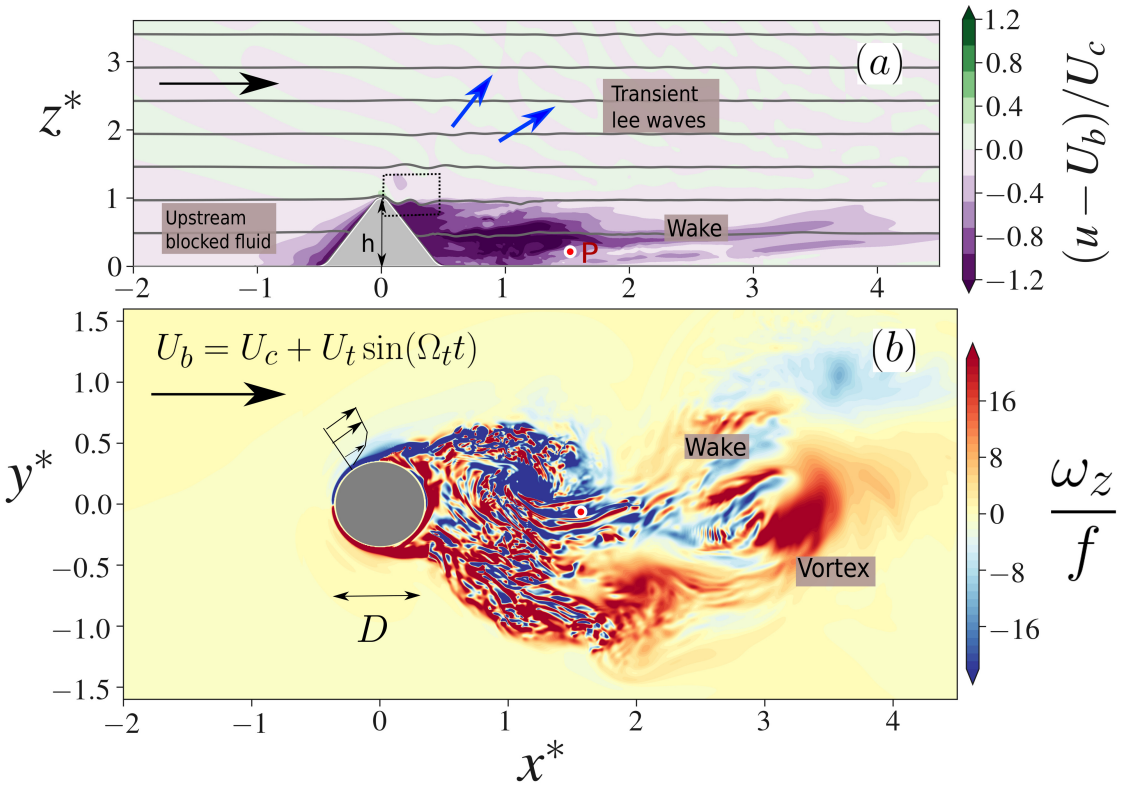

Figure 5.1: A snapshot of the simulated flow over a three-dimensional conical topography with the background velocity of the form $U_b = U_c + U_t \sin(\Omega_t t)$. Here the velocity scales are $U_c = 0.1$m/s and $U_t = 0.02$m/s, and the background stratification is $N = 4.45 \times 10^{-3}\text{s}^{-1}$. (a) Vertical cross-section ($y^* = 0$): A region of blocked fluid develops upstream and a wake develops downstream. A hydraulic jet forms near the apex of the topography (dotted box) and lee waves radiate above this hydraulically dominated zone. (b) Horizontal cross-section ($z^* = 0.25$): Contours of the normalized vorticity reveal boundary layer separation at the topography, turbulent near wake dominated by small scale features and a coherent lee vortex at $x^* = 3$.

change in momentum across the tidal phase can affect the spatial distribution of vorticity (e.g. Callendar et al., 2011). When an attached eddy forms in the recirculation region of the obstacle, the reversing pressure gradient associated with tidal deceleration can trap a coherent eddy, preventing it from advecting into the wake. The ability of the tidal forcing to exert control on the separation and advection of vortices in the streamwise direction is governed by the ratio of the tidal forcing term to the advection term in eq. (5.2). We define this parameter

as the tidal strength parameter ($\overline{S}$).

$$\overline{S} = \frac{R}{Ex_c} \tag{5.3}$$

In the $R \leq 1$ regime explored here, tidal oscillations can influence the shedding of vortices when $\overline{S}$ is $O(1)$. When $\overline{S} \ll 1$, the tide associated momentum loss is negligible. Therefore in the $\overline{S} \ll 1$ regime, the influence of tidal forcing on the shed wake vortices may be insignificant.

Table 5.1: Notation used in the model formulation and analysis of results.

x_m $(m = 1,2,3)$	= position vector (x,y,z)
h, D	= height and base diameter of the conical hill
t	= time
(x^*, y^*, z^*, t^*)	= $(x/D, y/D, z/h, tU_c/D)$
U_c, U_t	= mean and tidal velocity components
(u,v,w)	= streamwise, spanwise and vertical velocity components
(u^*, v^*, w^*)	= $(u/U_c, v/U_c, w/(U_c h/d))$
Ω_t	= tidal frequency in rad/s
$\Omega_{s,c}$	= natural vortex shedding frequency in rad/s
Ω_s	= observed wake-vortex frequency in rad/s
f	= inertial frequency in rad/s
$U_b = U_c + U_t \sin(\Omega_t t)$	= barotropic flow velocity
$(\omega_x, \omega_y, \omega_z)$	= streamwise, spanwise and vertical components of vorticity
ρ, ρ'	= density and density deviation
$\rho_{bg}(z), \rho_0$	= background density profile and reference density (resp.)
g	= gravitational acceleration
$N = \sqrt{\frac{-g}{\rho_0}\frac{\mathrm{d}\rho_{bg}}{\mathrm{d}z}}$	= Brunt-Väisäla frequency in rad/s
p	= pressure deviation from hydrostatic and geostrophic balance
p^*, ρ^*	= $p/\rho_0 U_c^2$, $\rho' / \left(-h\frac{\mathrm{d}\rho_{bg}}{\mathrm{d}z}\right)$
ν, κ	= kinematic viscosity and thermal diffusivity
ν_{sgs}	= subgrid scale eddy viscosity
τ_{mn}	= stress tensor
τ^*_{mn}	= $\tau_{mn}/(\nu U_c/D)$
$\mathcal{S}_{mn} = \frac{1}{2}\left(\frac{\partial u_m}{\partial x_n} + \frac{\partial u_n}{\partial x_m}\right)$	= rate of strain tensor
$\varepsilon = 2(\nu + \nu_{sgs})\mathcal{S}_{mn}\mathcal{S}_{mn}$	= dissipation rate
$\varepsilon^* = \varepsilon/(U_c^3/D)$	= normalized dissipation rate
$Re_c = U_c D/\nu$	= Reynolds number

5.2.1 Parameter space

we consider a tall obstacle in the presence of weak rotation. Therefore, the inertial frequency is set to its value at $15^{\circ}N$ such that $Ro_c = 5.5$ and the buoyancy frequency is set as $N = 4.45 \times 10^{-3}$ s^{-1} such that $Fr_c = 0.15$. The fluid upstream is partially blocked from traversing over the obstacle, which forces the fluid to separate laterally at depths below $O(U_c/N)$ from the crest (Hunt and Snyder, 1980; Baines, 1995). The tidal frequency is fixed such that $Ex_c = 0.5$, values of relevance in the ocean (Signell and Geyer, 1991; Edwards et al., 2004; MacKinnon et al., 2019). The velocity ratio R is varied from 0 to 1 by varying U_t, so that the barotropic flow is non-negative and creates a wake on the lee side of the obstacle (see MacKinnon et al., 2019, Fig 6). When $Ex_c = 0.5$, the tidal strength parameter ($\overline{S} = 2R$) ranges from 0 to 2. The dimensions of the hill are chosen such that $\Omega_{s,c}/\Omega_t$ is 5/6, which lies in the regime of tidal synchronization where shedding of vortices occurred at $\Omega_t/2$ as shown by Puthan et al. (2021b). However, in their simulation R is fixed at unity. In the real ocean, the tidal oscillations can vary over a wide range and these changes can influence generation of transient eddies (e.g. Yang et al., 2018). Thus we focus on the role of varying strength of tidal modulations (i.e. varying R) in emergence of transient eddies and the attendant dissipation in the wake. Additionally, the impact of tidal modulations on dissipation at the location of the downslope hydraulic jet shall be examined.

5.3 Results:

In a stably stratified flow over a 3D obstacle, the topographic Froude number governs the elevation above which fluid parcels may have sufficient kinetic energy to rise over the crest of the obstacle (Leo et al., 2016). In a steady background flow U_c, Sheppard (1956) proposed an expression for elevation (z_s) of this dividing streamline as $z_s = h - U_c/N$. This estimate agrees well for symmetric obstacles (Snyder et al., 1985). Tide-induced unsteadiness

in the barotropic flow may impose a temporal variability to z_s such that its normalized value becomes $z_s^*(t) = z_s(t)/h = 1 - U_b(t)/Nh$. When the instantaneous Froude number $U_b(t)/Nh$ lies below 1 throughout the tidal cycle, flow splitting is observed approximately at $z_s^*(t)$. Below $z^* = z_s^*$, the fluid parcels pass around the sides. The adverse pressure gradient initiates flow separation in these parcels, generating an unsteady wake with coherent vortices (fig. 5.1b). These fluid parcels are blocked in the upstream side (fig. 5.1a). On the other hand, fluid parcels with $z^* > z_s^*$ separate on the vertical plane near the crest, contributing to lee wave formation (Baines, 1995). A steady flow past periodic hills generates lee waves that do not vary in time (Gill, 1982). However, a time-dependent background flow generates transient lee waves, equivalent to an unsteady version of the classical lee wave problem shown by Bell (1975). Transient oceanic lee waves and an unsteady wake coexist here while extracting energy from the background geostrophic flow and transferring it to small scale turbulence (fig. 5.1). These features can generate 'hot-spots' of turbulent dissipation. Tidal synchronization may influence the temporal variability of wake dissipation and thus deserves attention in this context. Thus the motivation for this work is twofold. First, in section 5.3.1, we investigate the fluid driven around the hill, responsible for tidally modulated eddies. Second, in section 5.3.2 and section 5.3.3, we investigate the prominent dissipation 'hot-spots' downstream of the hill.

5.3.1 Onset of tidal synchronisation

Puthan et al. (2021b) showed that in a tidally modulated flow, when $R = 1$, downstream wake vortices are found at frequencies that differ from both the tidal frequency Ω_t and the natural shedding value $\Omega_{s,c}$. Instead, the frequency of the shed vortices coincided with $\Omega_t/2$ when $\Omega_{s,c}/\Omega_t = 5/6$. Puthan et al. (2021a) showed that the signature of the tidal subharmonic is ubiquitous in the entire wake at $\Omega_{s,c}/\Omega_t = 5/6$. Thus hereinafter, the terms 'wake vortex frequency' and 'vortex shedding frequency' are used interchangeably. Tidal synchronization can also occur when the tidal modulations are much weaker compared to U_c. To illustrate

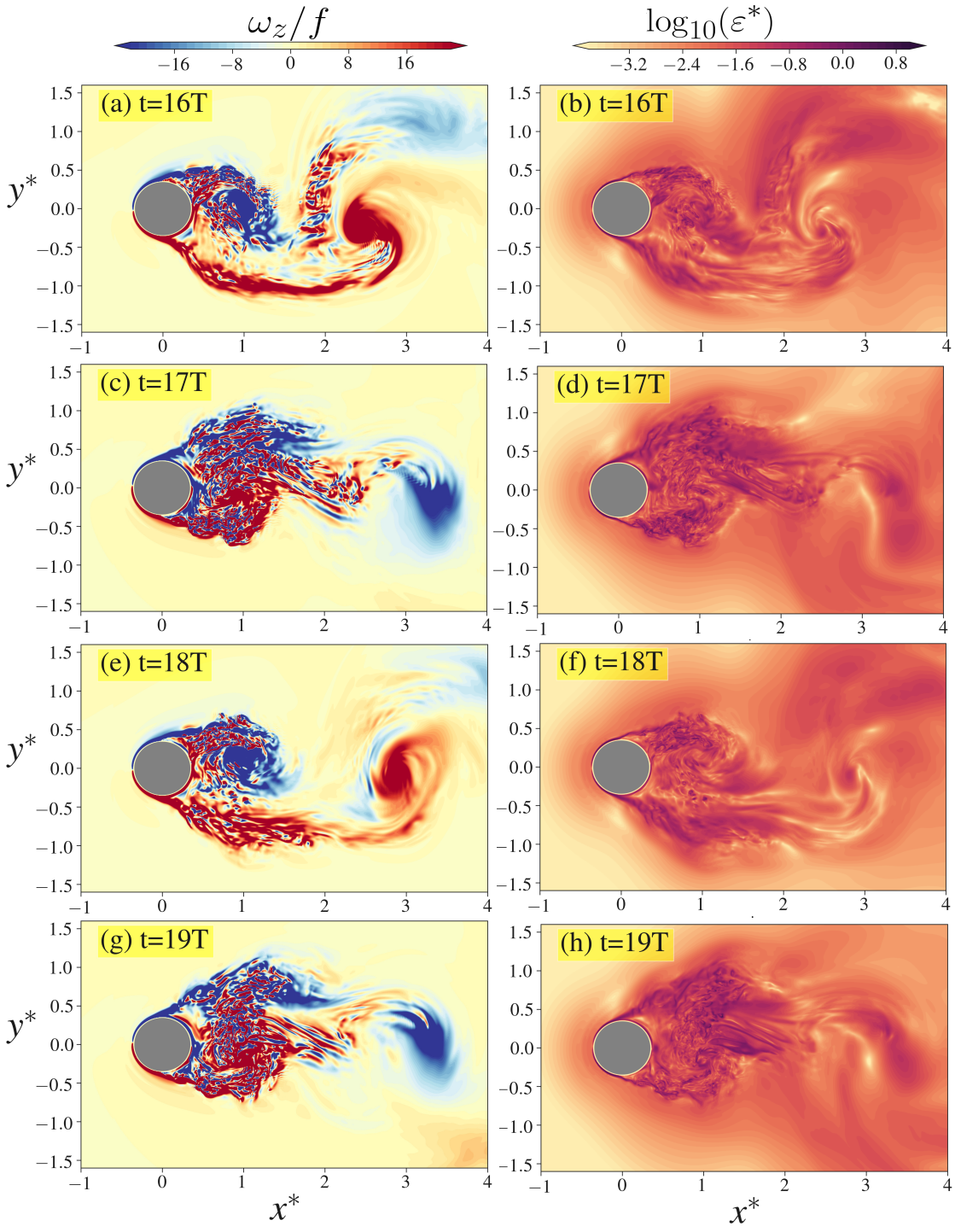

Figure 5.2: Instantaneous contour of normalized vertical vorticity (ω_z/f) and dissipation $\varepsilon^* = \varepsilon/(U_c^3/D)$ in the horizontal plane $z^* = 0.25$ for the case $R = 0.2$ at four time instants : (a,b) $t = 16T$, (c,d) $t = 17T$, (e,f) $t = 18T$ and (g,h) $t = 19T$.

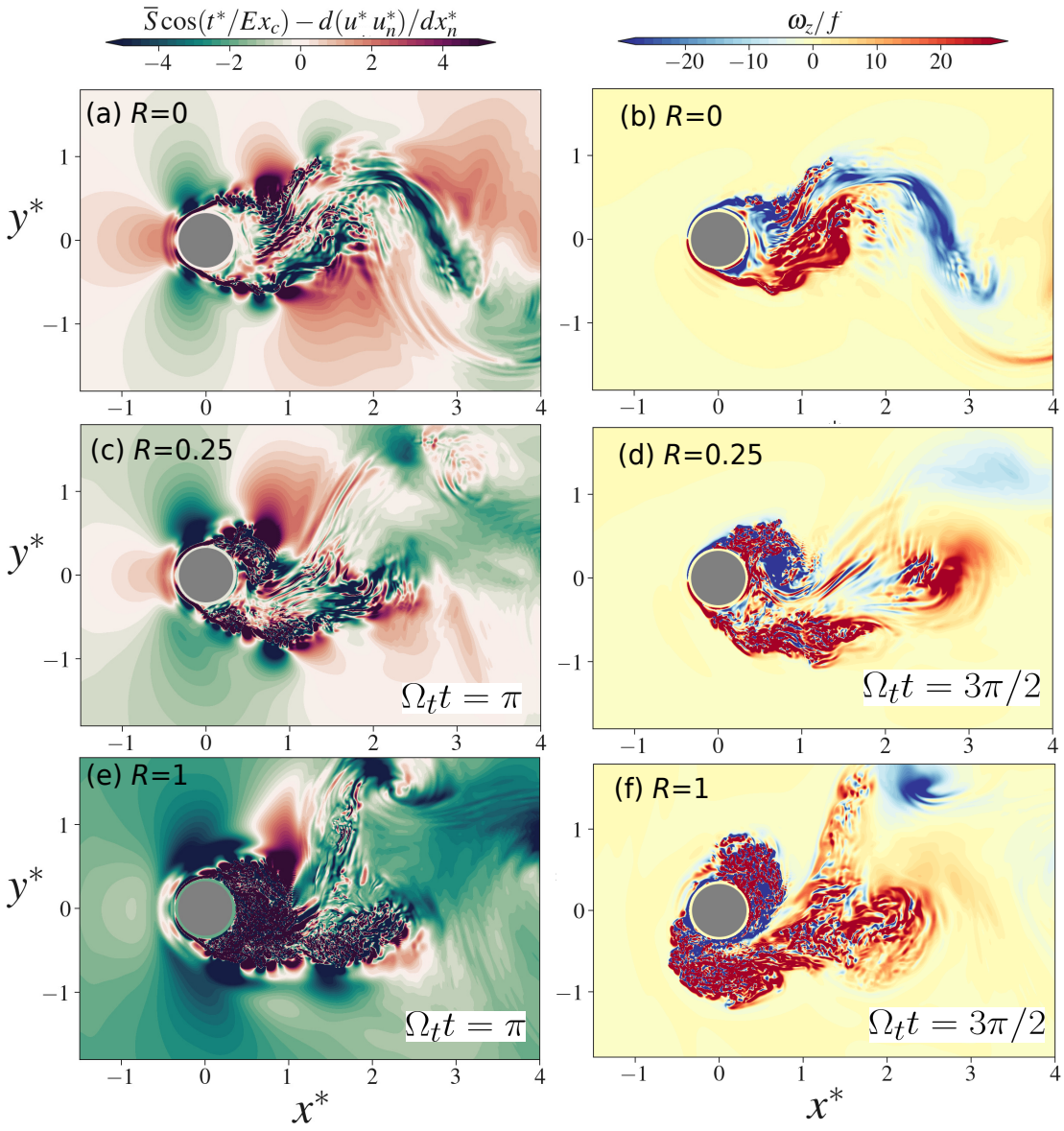

Figure 5.3: (Left) Net streamwise transport of momentum in the horizontal plane of $z^* = 0.25$ represented by $\overline{S}\cos(t^*/Ex_c) - d(u^*u_n^*)/dx_n^*$ (where $n = 1,2$) for cases (a)$R = 0.0$, (c) $R = 0.25$ at $\Omega_t t = \pi$ and (e) $R = 1$ at $\Omega_t t = \pi$. (Right) The normalized vertical vorticity ω_z/f in the horizontal plane of $z^* = 0.25$, is plotted for the same cases : (b)$R = 0.0$, (d) $R = 0.25$ at $\Omega_t t = 3\pi/2$ and (f) $R = 1$ at $\Omega_t t = 3\pi/2$.

this, contours of normalized vertical vorticity are plotted at $t = 16T, 17T, 18T$ and $19T$ in fig. 5.2a,c,e and g for the case $R = 0.2$. These time instants are chosen at the phase of maximum tidal acceleration ($\Omega_t t = 0$). The contour of normalized wake dissipation at each instant is plotted on the right (fig. 5.2b,d,f,h). The contours of vertical vorticity (ω_z) in fig. 5.2a show

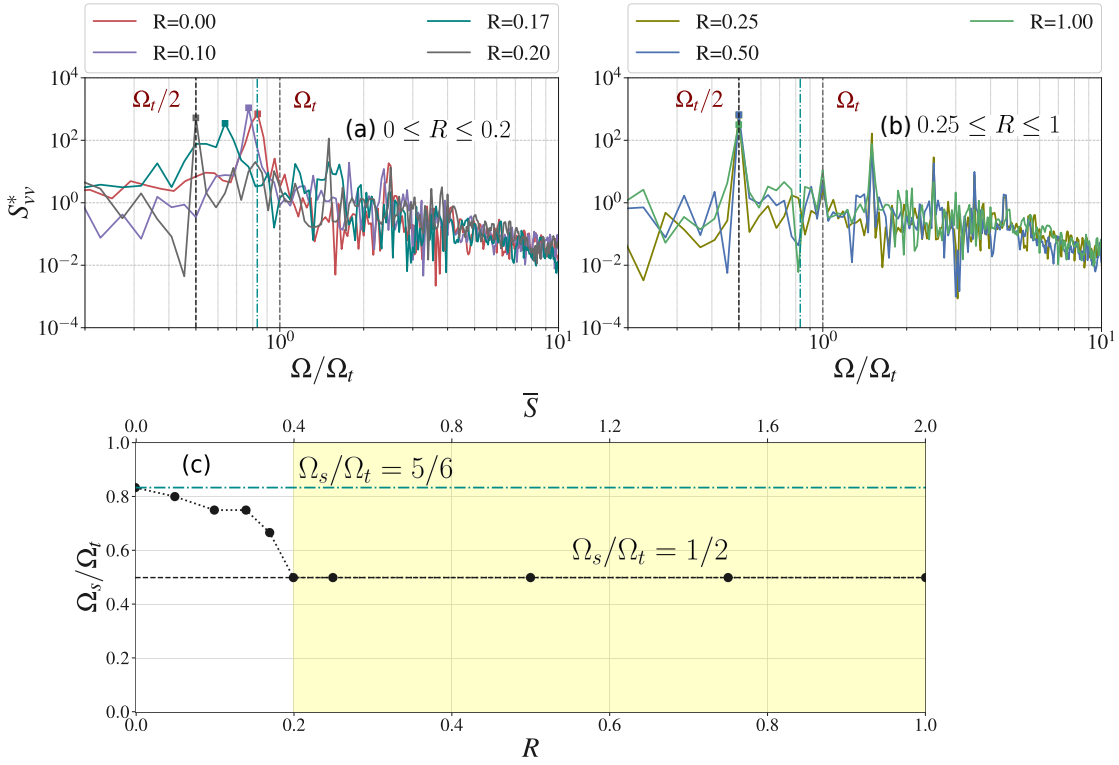

Figure 5.4: Normalized lateral velocity spectra $S^*_{vv} = S_{vv}/U_c^2$ at location P at $(x^*, y^*, z^*) = (1.5, 0, 0.25)$ (also marked in fig. 5.1) for multiple cases : (a) $R = 0, 0.05, 0.1, 0.17, 0.2$ and (b) $R = 0.2, 0.25, 0.5, 1$. The blue dash-dotted line at Ω/Ω_t = 5/6 denotes the natural shedding frequency $\Omega_{s,c}$. In (c), the observed value of normalized wake-vortex frequency Ω_s/Ω_t is plotted against R. The shaded region represents the parameter space where vortices are shed at $\Omega_t/2$.

the formation of shear layers on lateral sides of the hill during flow separation at $t = 16T$. The shear layer on the $+y$ side rolls up to form an anticyclonic (negative) vortex close to the centerline at $x^*, y^* = 1, 0$. The shear layer on the $-y$ side elongates and rolls up into a cyclonic (positive) vortex at $x^*, y^* = 2.5, -0.25$. The eddy formation occurs during the acceleration phase of the tidal cycle. The vertical vorticity ω_z for these vortices is as large as $20f$, a characteristic of high Rossby wakes (MacKinnon et al., 2019). Turbulent fluctuations are observed in the anticyclonic vortex during its formation behind the obstacle in the near wake. The snapshot of dissipation at this instant in fig. 5.2b reveals high values of normalized dissipation ε^* in the thin shear layer that stretches between the obstacle and the vortex. These

thin strips of enhanced dissipation are very common up to two diameters from the obstacle. After one tidal cycle (fig. 5.2c), a cyclonic vortex forms in the near wake (at $x^* = 1$). The anticyclonic vortex in the near wake at $16T$ migrates to $x^* = 3.5$ at $17T$. The small scale turbulent fluctuations near this vortex at $16T$ are no longer present at $17T$. Figure 5.2d also shows thin strips of dissipation concentrated at the shear layer. The dissipation rate exceeds U_c^3/D at this zone e.g. near $x^*, y^* = 1, 0.5$.

In the next cycle, $t = 18T$ (fig. 5.2e,f), a new anticyclonic vortex is formed at $x^* = 1$, while the cyclonic vortex formed during $t = 17T$ moves downstream. Eventually, this anticyclonic vortex reaches $x^* = 3.5$ at $t = 19T$ (fig. 5.2g), repeating the sequence. A recurrent pattern emerges where opposite-signed vortices in the wake occur over successive tidal cycles to form a Strouhal pair over two tidal cycles so that $\Omega_s = \Omega_t/2$. Tidal synchronization also modulates the dissipation rate in the wake as seen in fig. 5.2b,d,f,h. The spatially-intermittent hot-spots of dissipation in the near wake shift temporally with the lateral meanders of the shear layer.

In the absence of tidal oscillations, a Kármán vortex street evolves such that $u(x,y,z,t) = u(x,-y,z,t+T_s/2)$, where T_s is the shedding period. The tidal forcing induces a temporal periodicity and lateral symmetry in the flow given as $u(x,y,z,t) = u(x,-y,z,t) = u(x,-y,z,t+T)$. In order the restore the original spatio-temporal symmetry imposed by the vortex street, T_s must coincide with $2T$. Thus in fig. 5.2, vortices are shed over two tidal cycles. The above argument holds true when the tidal forcing is sufficiently strong to enforce temporal periodicity and lateral symmetry. In other words, the tidal strength parameter $\overline{S}$ in eq. (5.2) must be large relative to the advection term to control the spatial organization of vortices. For example, at $R = 0.2$, the accelerating background flow between $t = 15.75T$ and $t = 16.25T$ enables formation of a single anticyclonic vortex at $x^*, y^* = (1,0)$ in fig. 5.2a. During the deceleration phase, the tidal forcing removes sufficient momentum from the background flow to prevent release of the cyclonic vortex on the laterally opposite side of the obstacle. As a result, its sep-

aration is delayed to the acceleration phase of the next tidal cycle, which begins at $t = 16.75T$ (see supplement). To illustrate this, the difference between the momentum associated with tidal forcing and the advection term is computed and plotted in fig. 5.3a,c,e for $R = 0, 0.25$ and 1. The normalized vorticity field for the same cases are plotted in fig. 5.3b,d,f. For the cases $R = 0.25$ and 1, these contours are plotted at the phase of maximum tidal deceleration ($\Omega_t t = \pi$) in fig. 5.3c,e and at phase $\Omega_t t = 3\pi/2$ in fig. 5.3d,f. When $R = 0$, the tidal forcing term is absent. Therefore, advection of shed vortices into the wake occurs unimpeded throughout the shedding cycle (supplement). On the other hand at $R = 1$, the eddy in the recirculation zone experiences a strong tide-induced adverse pressure gradient (fig. 5.3e). This adverse pressure gradient is also observed adjacent to the shear layer at $x^* = 0$ and $y^* = -1, 0.5$. This pressure gradient prevents the attached eddy from separating and advecting downstream at this instant. Instead, the tide-induced pressure gradient is strong enough to drive the flow upstream at $\Omega_t t = 3\pi/2$ (fig. 5.3f), creating secondary dipoles (Puthan et al., 2021b).

For the case $R = 0.25$, the adverse pressure gradient is just sufficient to prevent the eddy from shedding at the obstacle boundary (fig. 5.3c,d). Unlike for $R = 1$ (see Puthan et al., 2021b), weak tidal modulations are incapable of generating a large local adverse pressure gradient that drives the flow upstream to create tidal dipoles at the minimum velocity phase $\Omega_t t = 3\pi/2$ (fig. 5.3d). Therefore, the eddy is retained in the recirculation zone until the next tidal acceleration phase commences.

Vortex synchronization of this kind is common in unstratified cylinder flows (e.g. Konstantinidis and Liang, 2011) when the tidal and natural shedding period are in close proximity. The velocity ratio R plays a crucial role in this process but has not been examined previously in a geophysical context. The minimum amplitude of tidal modulation required for onset of tidal synchronization is of interest and shall be investigated in fig. 5.4.

The spectra of time-series is computed from time evolution of spanwise velocity at location P in fig. 5.1a and plotted in fig. 5.4a,b. Figure 5.4a shows the velocity spectra for

cases with R ranging from 0 to 0.2 while fig. 5.4b shows the velocity spectra for cases with R ranging from 0.2 to 1. The dominant frequency is shown by the square marker. Notice the red curve in fig. 5.4a corresponding to $R = 0$. For this case, the dominant frequency coincides with the natural shedding frequency $\Omega_{s,c} = 5\Omega_t/6$. However, when R is increased, the dominant frequency peak shifts gradually towards $\Omega_t/2$ as R is increased from 0 to 0.2. To illustrate this trend, the *observed* wake vortex frequency Ω_s is plotted against R in fig. 5.4c. For cases with $R \geq 0.2$, the wake vortex frequency is synchronized to the tidal subharmonic $\Omega_t/2$ (fig. 5.4b). In the tidally synchronized cases (fig. 5.4b), spectral peaks are also observed at $3\Omega_t/2, 5\Omega_t/2$ and other higher harmonics owing to non-linear triadic interactions in the wake (Schmidt, 2020). During the transition of the wake vortex frequency from $\Omega_{s,c}$ to $\Omega_t/2$, the tidal strength parameter $\overline{S}$ varies from 0 to 0.4. Even weak tidal modulations at $\overline{S} = 0.1$ ($R = 0.05$) are capable of reducing the frequency of shed vortices from $\Omega_{s,c}$. However when $S \leq 0.28$ ($R \leq 0.14$), the deviation of Ω_s from $\Omega_{s,c}$ is less than 10%. A significant reduction in Ω_s is observed when $\overline{S}$ increases from 0.28 to 0.4. At this stage, the momentum loss associated with tidal forcing is sufficient to induce significant reduction to the frequency of wake vortices through the eddy trapping mechanism discussed in fig. 5.3. Between $\overline{S} = 0.4$ and $\overline{S} = 2$, the forcing-induced momentum loss allows only a single vortex to separate every tidal cycle. Thus Ω_s is permanently altered to $\Omega_t/2$.

5.3.2 Downstream dissipation rate

Stratified flows at lower Froude numbers are subject to upstream blocking (fig. 5.1a), allowing only fluid above the height of z_s^* from the bottom, to move over the topography (Hunt and Snyder, 1980). The flow at the ridge top accelerates downslope as a thin intensified jet, a signature of a limited hydraulic response at small topographic Froude numbers. Winters and Armi (2014) showed that near the crest, the active layer thickness decreases while the maximum local velocity increases. The jet compensates for the transport deficit in the blocked

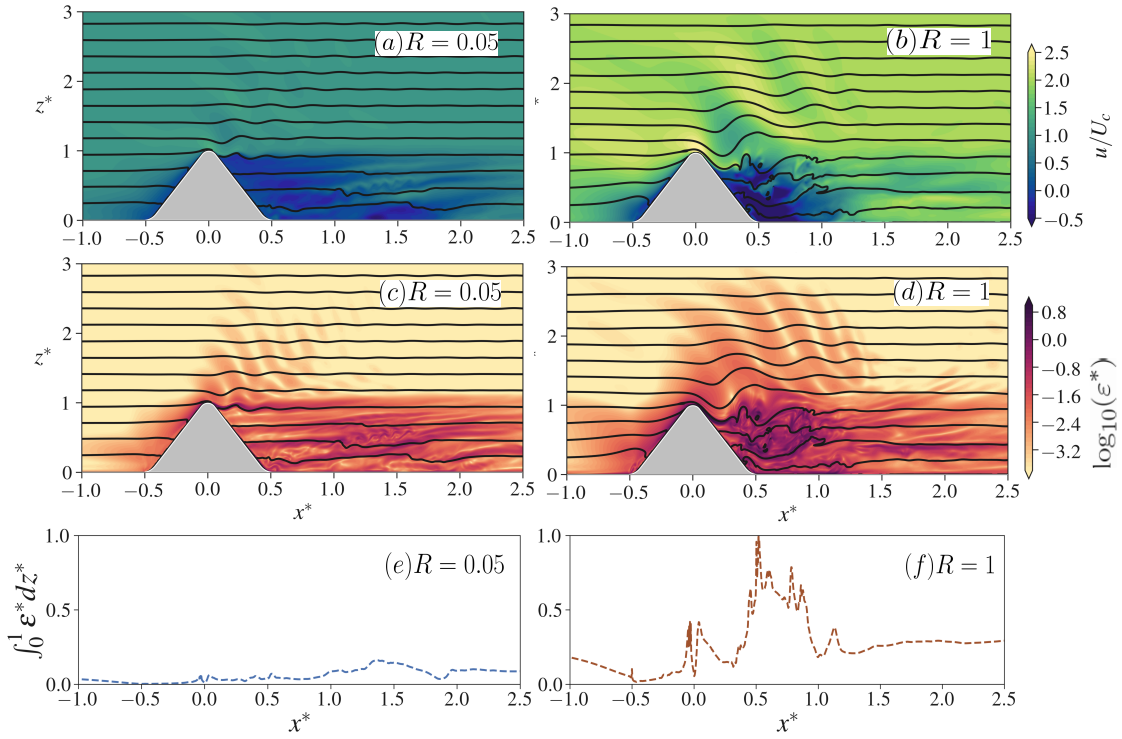

Figure 5.5: Snapshot of normalized streamwise velocity u/U_c and dissipation $\varepsilon^* = \varepsilon/(U_c^3/D)$ in $y^* = 0$ vertical plane at the maximum velocity phase $\Omega_t t = \pi/2$: (a,c) Case $R = 0.05$ and (b,d) Case $R = 1$. Their depth-integrated dissipation values are plotted in (e) and (f).

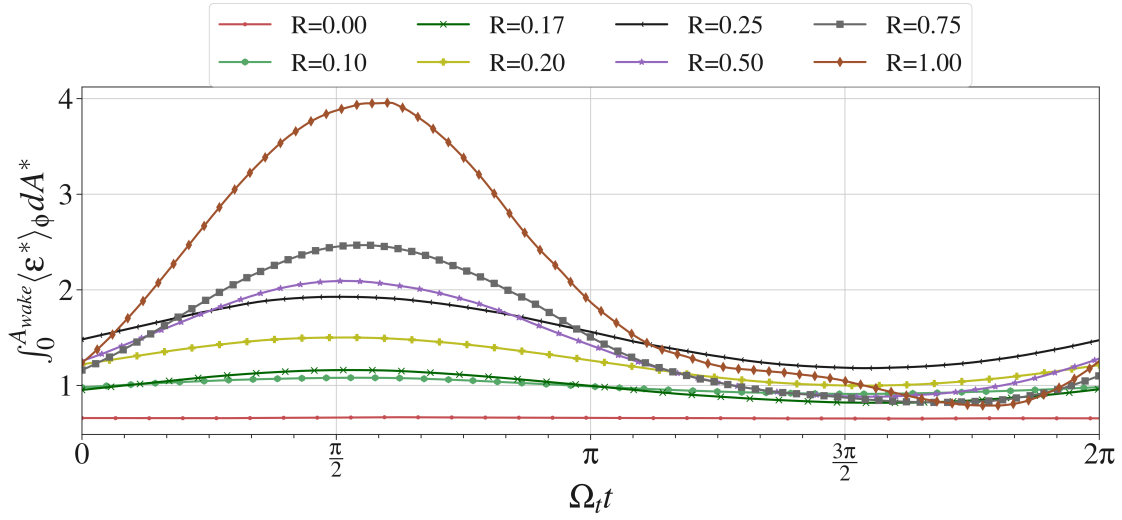

Figure 5.6: Phase-averaged dissipation $\langle \varepsilon^* \rangle_\phi$ in the $y^* = 0$ vertical plane integrated over the downstream wake region ($x^* > 0$ and $z^* < 1$), denoted as A_{wake}.

layer. This jet plunges below the crest on to the lee side. As a result, a zone of strong localised turbulence is formed (Winters and Armi, 2013, 2014). It is important to note that the mechanisms governing dissipation from breaking lee waves are different from those for hydraulic jet induced localized dissipation. The former occurs above the obstacle during wave propagation while the latter occurs in a localized region in the lee close to the crest of the hill. In the $Fr_c \ll 1$ regime, the radiating lee wave component may be small even though the turbulence is strong near the apex of the topography. Therefore, the prominent dissipation zones are located in the wake and the hydraulic response region. Dissipation in these regions shall be quantified and explored below.

Figure 5.5 shows snapshots of velocity and dissipation on the mid-center plane ($y^* = 0$) for cases $R = 0.05$ and $R = 1$. The instantaneous snapshots capture the velocity contours at the phase of maximum velocity ($\Omega_t t = \pi/2$) in fig. 5.5a,b. The barotropic velocity at this instant is at its maximum value of $U_t + U_c$. Klymak et al. (2010b) showed that time required for the first wavelength response of lee wave is $\Delta t = 2\pi/(N\alpha_s)$, where α_s is the topographic steepness parameter. Sufficient time is available for the lee waves to form if

$$\frac{\Delta t}{T} < 1 \quad \Rightarrow \quad \frac{\Omega_t}{N\alpha_s} < 1 \tag{5.4}$$

For the present study, $\Omega_t/N = (Fr_c/Ex_c)(h/D)$ is 0.09 and α_s is 0.3, so that the condition in eq. (5.4) holds true and sufficient time is available for multiple wavelengths of the lee wave to develop, as seen in fig. 5.5a,b.

The velocity amplitude of the hydraulic jet is dependent on the instantaneous Froude number ($Fr = U_b/Nh$). At phase $\Omega_t t = 0$ the barotropic velocity equals U_c. Therefore, the instantaneous Froude number Fr is same at both $R = 0.05$ and 1. During the acceleration phase, the barotropic velocity rises until it reaches its maximum at $\Omega_t t = \pi/2$. At this instant, the Fr is 0.157 for $R = 0.05$ case and 0.3 for $R = 1$ case. The downslope jet gains momentum during

this phase (supplement). A localized high velocity region develops at the crest. Figure 5.5a and b show the qualitative differences in the jet intensity during the maximum velocity phase in this region. For the $R = 0.05$ case (fig. 5.5a), the hydraulic jet induces a small deformation to the isopycnal near the crest. The region where the downslope jet separates to form a lee wave is a zone of high dissipation (fig. 5.5c). Dissipation hot-spots are also observed in the wake e.g. in the region $1 < x^* < 1.5$ and $y^* = 0.5$. A stronger lee wave response occurs for $R = 1$ at $\Omega_t t = \pi/2$ owing to the larger Fr. The strong jet near the crest causes steepening of the isopycnals. The tidal forcing supplies more momentum to the jet at this instant (compared to $R = 0.05$), which helps it to navigate the potential energy barrier to a larger depth from the crest. Larger deformation in the isopycnals is a sign of elevated dissipation rates in the lee (fig. 5.5d). Additionally the wavelength of the lee waves (which is proportional to the background velocity), is larger when $R = 1$ compared to $R = 0.05$ at this instant (fig. 5.5a,b). In both cases, the region where jet plunges into the lee is a zone of high dissipation (fig. 5.5c,d). The high velocity jet induces strong shear in this region at $R = 1$. In addition to the shear-induced dissipation, the strongly accelerated jet induces large isopycnal deformation which contributes to enhanced turbulence and mixing. Thus ε^* is more intense at $R = 1$ when compared to $R = 0.05$ during this instant. The downstream wake is also a turbulent hot-spot in both cases. To quantify the dissipation rates in the wake region for the two cases, the instantaneous ε^* is integrated in the $y^* = 0$ plane from $z^* = 0$ to 1 and plotted along the streamwise direction in fig. 5.5e,f. Between $x^* = 0$ and 2 (near wake), the dissipation rate remains elevated in both cases. However, the integrated dissipation rate is three times larger at $R = 1$ compared to $R = 0.05$ in the near wake. For the case $R = 0.05$, the integrated dissipation rate increases gradually from $x^* = 0$ and reaches 0.2 at $x^* = 1.4$. When $R = 1$, the integrated dissipation rate reaches up to 1 at $x^* = 0.5$ and remains elevated above 0.5 between $x^* = 0.5$ and 1. The high dissipation rate in this region is attributed to mixing induced by the displacement of high density fluid in the lee by the low density fluid originating

upstream and strong velocity gradients along the vertical (Puthan et al., 2020).

The wake region (A_{wake}) in the $y^* = 0$ plane can be demarcated by the region : $x^* > 0$ and $z^* < 1$. The phase-averaged dissipation rate is integrated over this region and plotted against the tidal phase $\phi = \Omega_t t$ in fig. 5.6. Tidal oscillations clearly amplify the energy loss in the wake when compared to $R = 0$ case. The acceleration of the fluid from $\Omega_t t = 0$ to $\pi/2$ is accompanied by an increase in the dissipation rate in all tidally modulated cases. Maximum dissipation rate is observed at $\Omega_t t = \pi/2$ when the magnitude of barotropic velocity is largest. At this phase, the dissipation rate is higher when the magnitude of tidal modulation is higher (equivalently at higher R). The area-integrated dissipation rate exceeds $A_{wake}U_c^3/D$ at this instant when $R > 0$. As the flow decelerates from $\Omega_t t = \pi/2$ to $3\pi/2$, the dissipation rate reduces concomitantly until the beginning of the acceleration phase at $\Omega_t t = 3\pi/2$. At higher R, the temporal variability of the dissipation rate is also larger. For example when $R = 1$, the integrated dissipation in the wake is four times smaller at $\Omega_t t = 3\pi/2$ in comparison to its value at $\Omega_t t = \pi/2$. On the other hand at $R = 0.17$, the integrated dissipation reduces by only 5% when the flow moves from the high velocity phase ($\Omega_t t = \pi/2$) to the low velocity phase ($\Omega_t t = 3\pi/2$).

5.3.3 Energy loss in the hydraulic response region

Local dissipation is largely partitioned across three major components: dissipation in the wake, shear-induced dissipation by the hydraulic jet and energy loss from lee wave breaking. Previous studies have proposed various scaling laws relating the magnitude of local dissipation to the barotropic velocity. For example, numerical simulations of Klymak et al. (2010a) showed volume averaged local dissipation varied as U_b^3 and is smaller than the energy that radiated away. In a later study at Mendocino Escarpment, Musgrave et al. (2017) showed that local dissipation scales as U_b^k, where k lies between 1.6 and 2. The relationship between the dissipation rate and the flow speed is crucial for parametrization of dissipation in

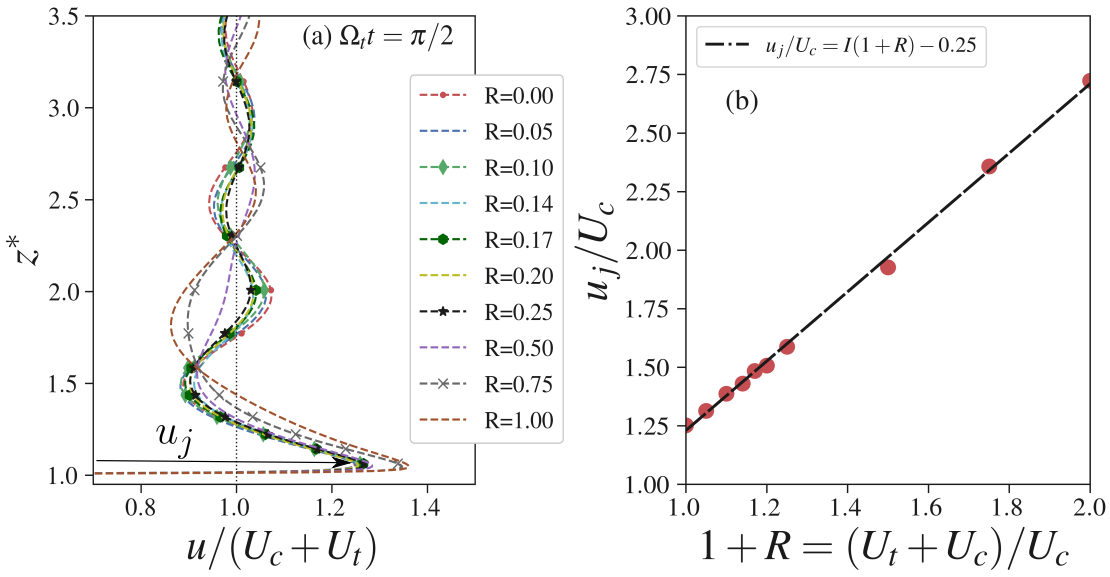

Figure 5.7: (a) Streamwise velocity profile of the hydraulic jet at the topography apex (x^*, y^*=0,0) at the maximum velocity phase ($\Omega_t t = \pi/2$). The maximum value of the jet velocity is denoted as u_j. (b) Red circles : Variation of u_j with $1+R$. The dash-dotted line is the linear fit.

global ocean models. In this section, we focus our attention towards the dissipation rate at the hydraulic response region and attempt to parametrize the permanent energy loss associated with the localized hydraulic jet.

Results of Winters and Armi (2013) noted that the velocity of the hydraulic jet has a strong influence on the dissipation magnitude. To estimate the jet velocity, the streamwise velocity profile at the apex of the hill is plotted in fig. 5.7a at $\Omega_t t = \pi/2$. The velocity is normalized by $U_c + U_t$. The velocity jet is skewed towards the apex of the obstacle along the vertical such that the maximum jet velocity (denoted as u_j) occurs at the vertical height of $z^* = 1.05$ for all cases. This accelerated layer decays away from the crest, but shows the signature of spatial oscillations associated with the hydraulic response. When $R \leq 0.25$, the vertical profiles of the streamwise velocity at the crest coincide, indicating its linear variation with the barotropic velocity $U_c + U_t$ (fig. 5.7a). However, the response of the hydraulic jet is more intense for cases $R = 0.5, 0.75$ and 1. The width of the jet increases concurrently amongst

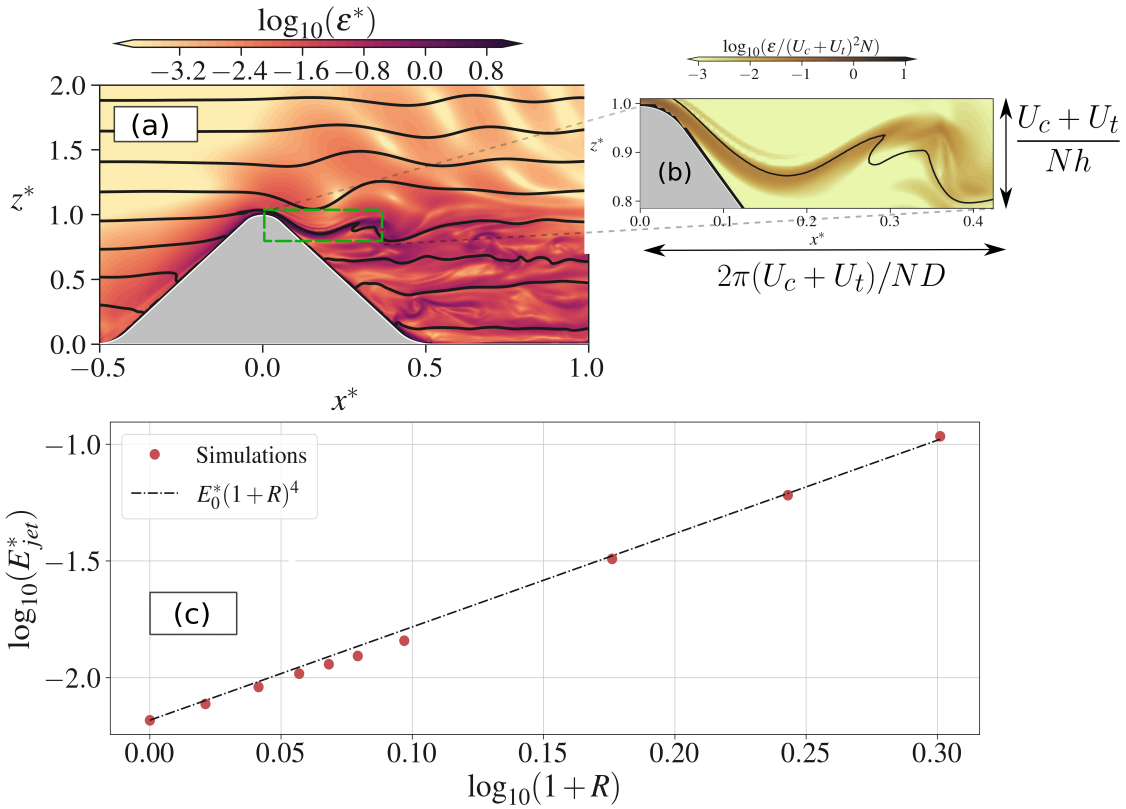

Figure 5.8: (a) Snapshot of dissipation rate induced by the hydraulic jet at the topography apex (x^*, y^*=0,0) for $R = 0.5$ and $\Omega_t t = \pi/2$. The green box shows the region of hydraulic response. The dissipation field in this region is magnified and plotted in (b). (c) The maximum value of the area-integrated and phase-averaged dissipation in the hydraulic response region in (b) plotted against $1+R$. Here, E_0^* is the area-integrated and phase-averaged dissipation in the hydraulic response region for the $R = 0$ case.

these cases to enable a larger flow transport (see Winters and Armi, 2014). Similar results have been observed in previous literature (e.g. Gayen and Sarkar, 2011), where increase in the jet velocity was associated with a modest increase in the width of the jet. Figure 5.7b shows linear relationship between the normalized jet velocity u_j/U_c and the normalized barotropic velocity $1+R$ at this instant. The linear fit is an excellent approximation for the jet velocity in the $0 \leq R \leq 1$ and $Fr \ll 1$ regime. The slope (I) of the linear fit represents the velocity intensification factor, estimated to be 1.48, close to the optimal value of 1.5 used in previous work (e.g. Winters and Armi, 2014).

Figure 8

The magnitude of the dissipation rate induced by the hydraulic jet is of interest. A snapshot of the dissipation field at the maximum velocity phase for the case $R = 0.5$ reveals several density disturbances occurring downstream (fig. 5.8a). The region associated with the hydraulic response (green box in fig. 5.8a) extends to a single wavelength of a lee wave in the streamwise direction, given by $\Delta x^* = 2\pi(U_c + U_t)/ND$ (Hunt and Snyder, 1980). Along the vertical, the region extends from $z^* = 1 - (U_c + U_t)/Nh$ to $z^* = 1$. Hereinafter, the area of this region is denoted as A_{jet}. The spatial dimensions of the hydraulic response region increases linearly as $1 + R$ along the vertical (z^*) and horizontal (x^*) directions. Thus, A_{jet} is proportional to $(1 + R)^2$. Previous studies show that the appropriate length scale associated with the turbulent patch in this zone is $(U_c + U_t)/N$ (e.g. Winters, 2015). Therefore, the dissipation in the turbulent layer is expected to scale as $(U_c + U_t)^2 N$, or equivalently, $U_c^2 N(1 + R)^2$. The turbulent layer in the hydraulic response region is shown in fig. 5.8b using contours of dissipation in units of $(U_c + U_t)^2 N$. The dissipation is concentrated in a thin shear layer associated with the separation of the intensified velocity jet (fig. 5.7a). Its value lies between $10^{-2} - 10^{-1} \times (U_c + U_t)^2 N$, consistent with estimates in literature (e.g. Jalali and Sarkar, 2017). The velocity jet transports low density fluid from the crest to this region, causing small density overturns during the displacement of high density fluid. In addition, momentum is also extracted from the jet through shear at the obstacle boundary. Therefore, these intense shear and mixing events contribute to the localized dissipation in this region.

To determine a possible scaling of the maximum dissipation in the hydraulic response region at $\Omega_t t = \pi/2$, ε is integrated over the region A_{jet}. The maxima of its normalized value across the tidal phase, E^*_{jet}, is then plotted against $1 + R$ in fig. 5.8c (red circles). The black dash-dotted line denotes the curve: $E^*_0(1 + R)^4$, where E^*_0 is the area-integrated and phase-averaged dissipation for the $R = 0$ case. This line clearly captures the variability of E^*_{jet} in the regime of $0 \leq R \leq 1$, which scales as $(1 + R)^4$. The explanation for this behavior is as follows. The maximum barotropic velocity is $U_c(1 + R)$. Therefore, the maximum dissipation

in this region is proportional to $(1+R)^2$. Since A_{jet} also scales as $(1+R)^2$, the area integrated dissipation E^*_{jet} varies as $(1+R)^4$. The bi-quadratic dependence of area-integrated dissipation on velocity ratio makes this zone an important sink of kinetic energy in abyssal flows especially at larger velocity ratios.

5.4 Discussions and conclusions

An LES study was carried out to examine the wake created by a stratified tidally modulated flow in the presence of weak background rotation. The barotropic flow U_b has a mean component U_c, and a tidal component U_t. The frequency of tidal modulation Ω_t is held constant and the velocity ratio $R = U_t/U_c$ is varied from 0 to 1 by varying U_t and keeping U_c constant. The Froude number Fr_c is small so that the near bottom flow is forced to separate laterally from the obstacle.

The frequency of the shed vortices reduces monotonically from its no-tide value of $\Omega_{s,c}$ when $R = 0$ to $\Omega_t/2$ when $R = 0.2$. When $0.2 \leq R \leq 1$, vortices are shed at $\Omega_t/2$. Tidal modulations tend to slow down the frequency of shed vortices by delaying the vortex separation during the deceleration phase of the tidal cycle and trapping it in the recirculation zone. For example, when $R = 0.2$, the vortices detach from the hill and move into the wake only during the tidal acceleration phase of each cycle. The momentum loss associated with the tidal forcing prevents migration of vortices into the wake during the deceleration phase when $R \geq 0.2$. This process is controlled by the tidal strength parameter $\overline{S} = R/Ex_c$. A significant reduction (larger than 10%) in the vortex shedding frequency is observed when $\overline{S}$ is larger than 0.28. When $0.4 \leq \overline{S} \leq 2$, the tidal forcing exerts control on the frequency of shed vortices by permitting vortex of a single sign to shed every tidal cycle. As a result, vortices are shed at a frequency equal to the tidal subharmonic.

The dissipation rate is spatially intermittent, with elevated values (exceeding U_c^3/D)

in the near wake and the hydraulic jet region. In the horizontal plane, dissipation remains concentrated in the thin shear layer extending from the hill. Dissipation rate in the wake increases during the tidal acceleration until it reaches its maximum value during the maximum velocity phase. The maximum dissipation rate increases with increasing R, explained by elevated shear and large deformations of isopycnals induced by stronger tidal modulations.

Upstream blocking at lower Froude numbers often forces flow near the crest of the topography to accelerate to compensate for the transport deficit. This phenomenon creates a localized jet in the lee which plunges below the apex of the hill. Low density fluid above the hill displaces the high density fluid in the lee creating a localized dissipation hot-spot. The jet velocity varies linearly with the maximum barotropic velocity $U_t + U_c$ (or equivalently $1 + R$), with minor deviations at larger velocity ratios. The intensification factor I, is estimated to be 1.48. At lower Froude numbers, the maximum area-integrated dissipation in this hydraulic response region scales as $(1+R)^4$ in the regime of $0 \leq R \leq 1$.

Acknowledgments

This chapter, in part, is currently being prepared for submission, for publication of the material. It may appear in *Journal of Geophysical Research: Oceans* as "Wake vortices and dissipation in tidally modulated abyssal hill wakes", P. Puthan, G. Pawlak and S. Sarkar. The dissertation author is the primary investigator and author of this paper.

Chapter 6

Energetics and mixing in buoyancy-driven near-bottom stratified flow

The interaction of abyssal flow with deep ocean topography generates internal waves. Breaking of internal waves in the abyssal ocean is one of the dominant sources of turbulent mixing (Munk and Wunsch, 1998). In this chapter, turbulence and mixing in near-bottom convectively driven flow is examined by numerical simulations of a model problem: a statically unstable disturbance at a slope with inclination β in a stable background with buoyancy frequency N. The influence of slope angle and initial disturbance amplitude are quantified in a parametric study. The flow evolution involves energy exchange between four energy reservoirs, namely the mean and turbulent components of kinetic energy (KE) and available potential energy (APE). In contrast to the zero-slope case where the mean flow is negligible, the presence of a slope leads to a current that oscillates with $\omega = N \sin\beta$ and qualitatively changes the subsequent evolution of the initial density disturbance. The frequency, $N \sin\beta$, and the initial speed of the current are predicted using linear theory. The energy transfer in the sloping cases

is dominated by an oscillatory exchange between mean APE and mean KE with a transfer to turbulence at specific phases. In all simulated cases, the positive buoyancy flux during episodes of convective instability at the zero-velocity phase is the dominant contributor to turbulent kinetic energy (TKE) although the shear production becomes increasingly important with increasing β. Energy, that initially resides wholly in mean available potential energy (MAPE), is lost through conversion to turbulence and the subsequent dissipation of TKE and TAPE (turbulent available potential energy). A key result is that, in contrast to the explosive loss of energy during the initial convective instability in the non-sloping case, the sloping cases exhibit a more gradual energy loss that is sustained over a long time interval. The slope-parallel oscillation introduces a new flow time scale of $T = 2\pi/(N\sin\beta)$ and, consequently, the fraction of initial APE that is converted to turbulence during convective instability progressively decreases with increasing β. For moderate slopes with $\beta < 10^{\circ}$, most of the net energy loss takes place during an initial, short ($Nt \approx 20$) interval with periodic convective overturns. For steeper slopes, most of the energy loss takes place during a later, long ($Nt > 100$) interval when both shear and convective instability occur, and the energy loss rate is approximately constant. The mixing efficiency during the period dominated by convectively driven turbulence is found to be substantially higher than the widely used value of 0.2.

6.1 Introduction

Topographic internal gravity waves are a major driver of turbulent mixing in the ocean that, in turn, is a key control on the ocean stratification and the meridional overturning circulation. Convective overturns have been identified in the context of breaking lee waves in observations (Alford et al., 2014; Marques et al., 2021) and two-dimensional simulations (Legg and Klymak, 2008; Buijsman et al., 2012) of tidal flow over oceanic ridges. Turbulence at

specific phases, notably from down to upslope flow, has been traced to convective overturns in three-dimensional simulations of oscillating flow past steep model obstacles, e.g. a linear slope at critical angle (Gayen and Sarkar, 2011), a triangular obstacle (Rapaka et al., 2013; Jalali et al., 2014), a multiscale obstacle patterned after a transect of a ridge at Luzon strait (Jalali and Sarkar, 2017), and in the internal-wave driven bottom boundary layer of lakes (Lorke et al., 2015; Becherer and Umlauf, 2011).

The mixing efficiency, fraction (Γ) of the total energy loss rate that is used for the mixing of density, has received much attention in the literature on stratified turbulence because it quantifies the inevitable modification by small-scale processes of the large-scale stratification in the ocean. Although Γ is typically assumed to be 0.2 in mixing parameterizations and in estimates derived from ocean observations, its measurements exhibit considerable variability (Sohail et al., 2018; Thorpe, 1994). Central questions that are fundamental to internal-wave driven near-bottom turbulence and also have implications for the diagnostic and prognostic ability of convective overturns with regards to turbulence are as follows: What is the rate at which the available potential energy (APE) of a convective overturn is lost and how is this energy loss partitioned among kinetic energy dissipation and APE dissipation? What is the net amount of initial energy that is dissipated by turbulence? What are the salient characteristics of the turbulence that arises from a convective overturn on a slope? How do the answers to the previous three questions depend on slope steepness?

We address the aforementioned questions using simulations of a model problem, formulated in our study, that is designed to study the behavior of a near-bottom convective overturn in isolation, as an idealization motivated by recent observations of large isolated convective overturns in energetic regions (Aucan et al., 2006; Alford et al., 2011; Bluteau et al., 2011). In particular, an initial density disturbance with APE is introduced in a stratified fluid over a slope (fig. 6.1), and its evolution followed for different values of the disturbance amplitude and slope angle.

6.2 Formulation

6.2.1 Governing equations

The coordinate axis is rotated in the $x-z$ plane by the slope angle β for ease of numerical simulation. The governing equations in this rotated coordinate system (x_s, y_s, z_s) are as follows:

$$\boldsymbol{\nabla} \cdot \mathbf{u}_s = 0 \tag{6.1}$$

$$\frac{D\mathbf{u}_s}{Dt} = -\frac{1}{\rho_0}\nabla p^* + \nu\nabla^2\mathbf{u}_s - \frac{g\rho^*}{\rho_0}(\sin\beta\mathbf{i} + \cos\beta\mathbf{k}) - \boldsymbol{\nabla}\cdot\boldsymbol{\tau} \tag{6.2}$$

$$\frac{D\rho^*}{Dt} = \alpha\nabla^2\rho^* - (u_s\sin\beta + w_s\cos\beta)\frac{\mathrm{d}\rho_b}{\mathrm{d}z} - \boldsymbol{\nabla}\cdot\boldsymbol{\Psi} \tag{6.3}$$

where $\mathbf{u}_s$ is the velocity field in the rotated coordinates with components u_s, v_s, and w_s along the x_s, y_s and z_s directions, respectively. At the bottom boundary ($z_s = 0$), no slip ($\mathbf{u} = \mathbf{0}$) is imposed on the velocity and ρ obeys the zero normal-flux boundary condition (BC). Since,

$$\rho = \rho_0 + (z_s\cos\beta + x_s\sin\beta)\frac{\mathrm{d}\rho_b}{\mathrm{d}z} + \rho*,$$

$\partial\rho/\partial z_s = 0$ at $z_s = 0$ requires $\partial\rho^*/\partial z_s = -\cos\beta\, d\rho_b/dz$ as the BC for ρ^*.

6.2.2 Problem Setup

The model problem is illustrated in Figure 6.1. The background at time $t = 0$ has zero velocity and is unstable owing to a finite-height disturbance: a single wavelength of a mode, $\rho^* = -\rho_p\sin(mz_s)$, with specified wave number m.

The ρ^* perturbation at $t = 0$ is of the form $\rho^* = -\rho_p\sin(mz_s)$ and spans a single wavelength, extending from the bottom to $z_s = \lambda = 2\pi/m$. The perturbation leads to a density

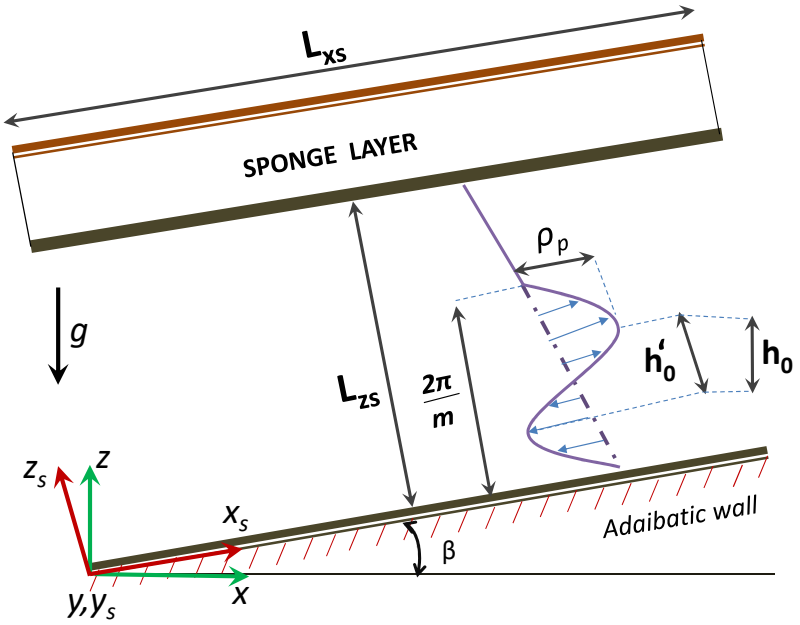

Figure 6.1: Schematic of the problem. Flow is induced by a convective instability introduced over a slope inclined at angle β with the horizontal. The instability is imposed at $t = 0$ through a density perturbation of amplitude ρ_p and wavelength $2\pi/m$ in z_s.

overturn with height, h_0, which is computed as :

$$h_0' = \frac{2}{m}\cos^{-1}\left(\frac{N^2\rho_0}{g\rho_p m\cos\beta}\right) \tag{6.4}$$

$$h_0 = h_0'\cos\beta = \frac{2\cos\beta}{m}\cos^{-1}\left(\frac{N^2\rho_0}{g\rho_p m\cos\beta}\right) \tag{6.5}$$

Two series of simulations are performed. The first series (Table 6.1) contains six cases that combine two values of ρ_p and three values of β, and is designed to obtain an overall view of the flow that results from the convective overturn and the pathways taken by the potential energy associated with the initial density profile. In the second series (Table 6.2), a wide range of angles is examined with β up to 45°.

$$\Gamma(t) = \frac{\int_0^t \langle \chi_\rho^T + \chi_\rho^M \rangle_{z_s} dt}{\int_0^t \langle \varepsilon^T + \chi_\rho^T + \varepsilon^M + \chi_\rho^M \rangle_{z_s} dt} \tag{6.6}$$

Table 6.1: Key parameters of Series A. There are six LES cases, denoted by ANGβ-ρ^*, with $\beta = \{0^\circ, 2.5^\circ, 5^\circ\}$ and $\rho^* = \{0.01, 0.02\}$ kg/m^3. The spanwise domain length L_{ys} is 10m with $N_y = 64$ points and grid spacing $\Delta y_s = 0.156$ m. The slope-normal size is $L_{zs} = 150$ m and there are $N_z = 641$ variably-spaced points with $\Delta z_{min} = 0.0037$ m. The density disturbance has a wavelength ($2\pi/m$) of 130m. Here, Ra is given by $g\rho_p h_0^3/(\rho_0 \nu\kappa)$, where h_0 is computed from eq. (6.5).

Case	ρ_p (kg/m^3)	β ($^\circ$)	L_{xs} (m)	N_x	R_ρ	Ra ($\times 10^{13}$)
ANG0-1	0.01	0°	60	256	0.2950	0.497
ANG0-2	0.02	0°	60	256	0.5900	2.167
ANG2.5-1	0.01	2.5°	30	128	0.2952	0.495
ANG2.5-2	0.02	2.5°	30	128	0.5954	2.16
ANG5-1	0.01	5°	30	128	0.2960	0.488
ANG5-2	0.02	5°	30	128	0.5920	2.14

Table 6.2: Series B has slope angle (β) that is steeper than in series A. β varies between 10 and 45° while the initial disturbance of density (amplitude $\rho_p = 0.02$ kg/m^3, wave number $m = 2\pi/130$ m^{-1}, Ra decreases with increasing β due to reducing size of overturns. The domain with slope-parallel dimensions of $L_{xs} = 30$ m and $L_{ys} = 10$ m has a grid with $N_x = 128$ and $N_y = 64$ points, and $\Delta x_s = 0.23$ m and $\Delta y_s = 0.156$ m. Here, Ra is given by $g\rho_p h_0^3/(\rho_0 \nu\kappa)$, where h_0 is computed from eq. (6.5).

Case	ρ_p (kgm^{-3})	β ($^\circ$)	R_ρ	Ra ($\times 10^{13}$)
ANG10	0.02	10°	0.600	2.05
ANG20	0.02	20°	0.628	1.724
ANG25	0.02	25°	0.650	1.507
ANG30	0.02	30°	0.681	1.27
ANG45	0.02	45°	0.834	0.575

The mixing efficiency (Γ) defined by eq. (6.6) measures the fraction of irreversible energy loss that goes towards scalar mixing, it does not involve quantities like the buoyancy flux that can be negative, and varies between 0 and 1 as an efficiency should.

6.3 Temporal variability of the mean flow

The presence of the slope leads to a qualitative difference in the evolution of the initially unstable patch. A mean flow develops along the slope and oscillates in time, contrary to the non-sloping case where the mean flow is zero. $\langle u \rangle$ and $\langle \rho^* \rangle$ oscillate with the frequency,

$N\sin\beta$, and the velocity lags density by a phase of $\pi/2$. Linear theory will be used to explain these features of the oscillation. The governing equations are linearized about a base state, $\mathbf{u} = \rho^* = p^* = 0$, diffusive effects are neglected and normal-mode perturbations of the form $A_p(z)\exp\{i(kx+ly)\}\exp\{st\}$ are introduced for each flow variable. The modal amplitudes satisfy the following system:

$$\frac{\partial w_p}{\partial z_s} + i(ku_p + lv_p) = 0 \tag{6.7}$$

$$su_p = -\frac{ikp_p}{\rho_0} - \frac{\rho_p g}{\rho_0}\sin\beta \tag{6.8}$$

$$sv_p = -\frac{ilp_p}{\rho_0} \tag{6.9}$$

$$sw_p = -\frac{1}{\rho_0}\frac{\partial p_p}{\partial z_s} - \frac{\rho_p g}{\rho_0}\cos\beta \tag{6.10}$$

$$s\rho_p = \frac{\rho_0 N^2}{g}(u_p\sin\beta + w_p\cos\beta) \tag{6.11}$$

The boundary condition at $z_s = 0$ is $u_p = v_p = w_p = 0$ and $\frac{\partial\rho}{\partial z_s} = 0$. It is straightforward to simplify above equations to obtain the following eigenvalue relation :

$$\begin{aligned} &\left[\left(\sin^2\beta + \frac{s^2}{N^2}\right)\frac{\partial^2}{\partial z_s^2} - 2ik\cos\beta\sin\beta\frac{\partial}{\partial z_s}\right]\rho_p = \left[\frac{s^2}{N^2}(k^2+l^2) + l^2 + k^2\cos^2\beta\right]\rho_p \\ \Rightarrow &\left(\sin^2\beta + \frac{s^2}{N^2}\right)\frac{\partial^2\rho_p}{\partial z_s^2} - ik\sin(2\beta)\frac{\partial\rho_p}{\partial z_s} - \left(\frac{s^2}{N^2}(k^2+l^2) + l^2 + k^2\cos^2\beta\right)\rho_p = 0 \end{aligned} \tag{6.12}$$

It is evident that if $k = l = 0$, a perturbation of background density in the z_s direction leads to a non-trivial steady harmonic response (since s is purely imaginary) with frequency ω and time period T given as

$$\omega = |s| = N\sin\beta, \quad T = \frac{2\pi}{N\sin\beta}\,. \tag{6.13}$$

Substitution of $k = 0$ in eq. (6.8) leads to $u_p = i(g/\rho_0 N)\rho_p$ for the $k = l = 0$ mode implying a

temporal phase difference of $\pi/2$ between the mean ($k = l = 0$) density and velocity fields. Finally, the solution for the mean flow after neglecting diffusion and dissipation becomes:

$$\begin{aligned} \langle \rho^* \rangle &= \rho_0^*(z_s)\cos(\omega t)\,, \\ \langle u_s \rangle &= -\frac{g\rho_0^*(z_s)}{\rho_0 N}\sin(\omega t) = \frac{b_0(z_s)}{N}\sin(\omega t)\,, \end{aligned} \tag{6.14}$$

where $\rho_0^*(z_s)$ is the initial density departure from the background and $b_0(z_s)$ is the corresponding buoyancy. The maximum value attained by u_s is b_0/N, much larger than the magnitude of steady diffusion-driven upslope flow that arises at a sloping boundary in a stratified fluid (Phillips, 1970; Phillips et al., 1986; Peacock et al., 2004).

Equation (6.14) can be interpreted as an oscillatory exchange of energy between the MAPE and MKE reservoirs. The APE of the initial density anomaly leads to a slope-parallel oscillatory current whose speed has amplitude b_0/N.

6.4 Vertical variability of the mean flow

In the sloping cases, the evolution is qualitatively different. The oscillatory mean flow discussed in section 6.3 modulates the density so that mixing is superposed on an oscillatory mean stratification. Case ANG5-2 is used as an example to discuss features of the vertical variability that are found to be common to all the sloping cases simulated for this study. Eight different time points are selected in the evolution of ANG5-2 and the slope-normal profiles of $\langle u \rangle$ and $\langle \rho^* \rangle$ at those times are plotted in fig. 6.2. The velocity, hereafter denoted as $\langle u \rangle_{max}$, chosen for the header is at $z = 0.21 L_{zs}$, the vertical location at which the velocity variation is maximum.

Figure 6.2(e-h) show four quarter phases of the first oscillatory cycle marked on the header as A,B,C and D, respectively. The APE is maximum at time A (fig. 6.2a) and is completely transferred to MKE at time B (fig. 6.2b) when the density profile coincides with

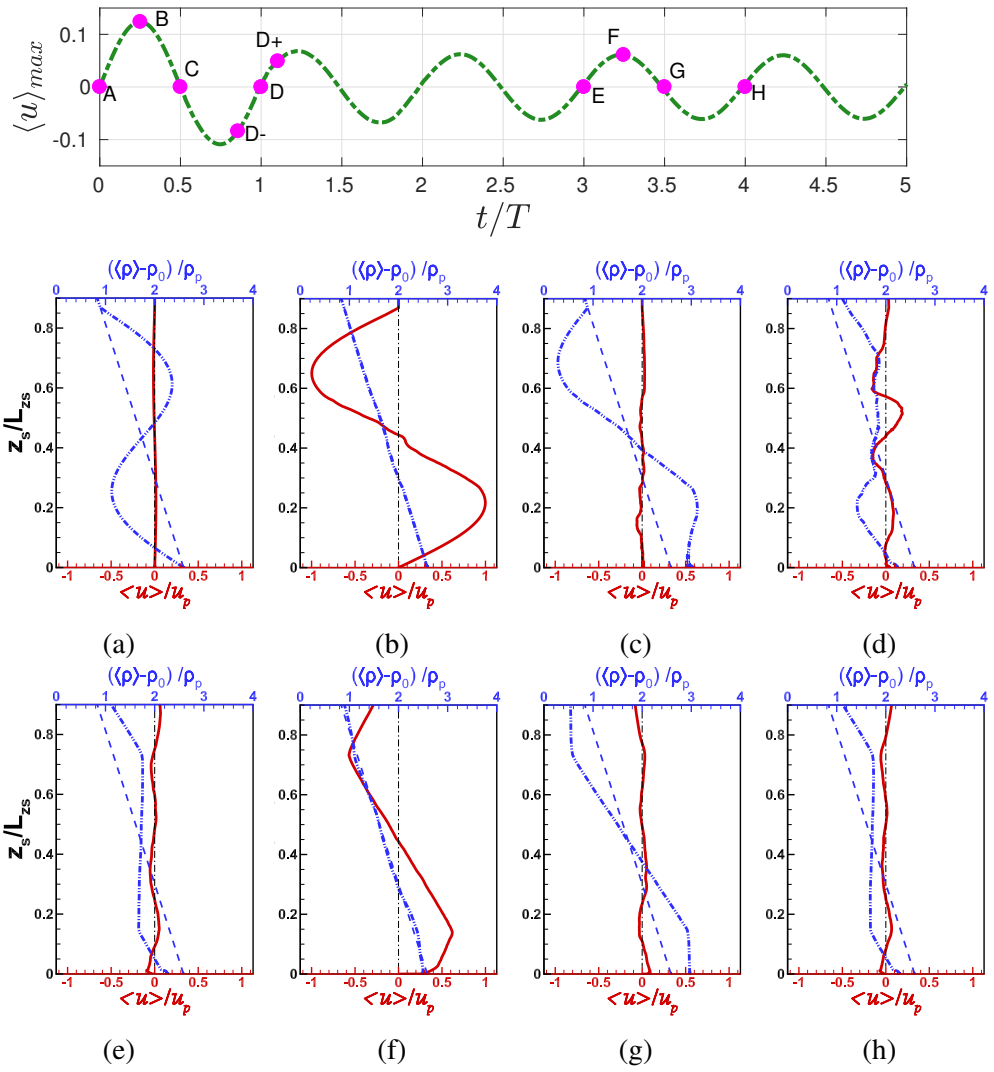

Figure 6.2: Vertical profiles of mean density (dash-dotted blue line) and mean streamwise velocity (solid red line) in case ANG5-2 at 8 time instants (circles on the velocity time-series of the header). The variables are made non-dimensional with ρ_p and $u_p = g\rho_p/\rho_0 N$ respectively. First row: (a) $t = 0$, (b) $t = T/4$ ($Nt = 18$), (c) $t = T/2$ ($Nt = 36$) and (d) $t = T$ ($Nt = 72$). Second row: (e) $t = 3T$, (f) $t = 3T + T/4$, (g) $t = 3T + T/2$ and (h) $t = 4T$. Background ρ_b is in dashed blue.

the initial background. At this point, $\langle u \rangle$ achieves its maximum amplitude, giving rise to upslope and downslope currents centered at $z_s/L_{zs} = 0.21$ and $z_s/L_{zs} = 0.66$, respectively. These currents disturb the equilibrium density configuration and eventually strengthen the stratification in the central zone at C (fig. 6.2c) so that N^2 exceeds its initial background value. At $t = 3T/4$ (not shown), $\langle u \rangle$ reaches a local maximum in amplitude and is oppositely directed to that at $t = T/4$. As the flow approaches $t = T$, the density cannot recover to its initial unstable configuration. A large convective overturning event (LCOE) with turbulence is initiated and it results in the $\langle \rho^* \rangle$ profile (fig. 6.2d) that has much weaker density variation than in the initial anomaly.

Examination of the fourth cycle (points E,F,G and H shown in the bottom row of fig. 6.2) leads to the following observations. First, at E (fig. 6.2e), the initial unstable density profile is absent. Second, the velocity currents are weaker at F (fig. 6.2f) compared to those at the same phase (B) in the first cycle. These two observations are related to the the mixing that has taken place over three cycles. Between points B and C, energy is transferred from MKE back to MAPE, with some energy lost to dissipation and mixing. At C, the central region (z_s/L_{zs} =0.33 to 0.66) is stable but there is a region of instability adjacent to the bottom. .

6.5 Energetics

The problem is initialized with zero velocity, an unstable mean density, and no density fluctuations. Thus, at $t = 0$ the energy resides exclusively in the MAPE reservoir. Figure 6.4 illustrates the effect of finite slope on evolution of the energy reservoirs and the time-integrated dissipation terms. In the non-sloping case ANG0-2 (fig. 6.4a), the initial APE decays and asymptotes to an approximately constant value by $Nt \approx 30$. The transfer to MKE is negligible. Both TKE and TAPE increase initially, peak at $Nt \approx 15$, and then decay. Visualizations (not shown) indicate that it is a single LCOE whose breakdown is responsible for energy transfer

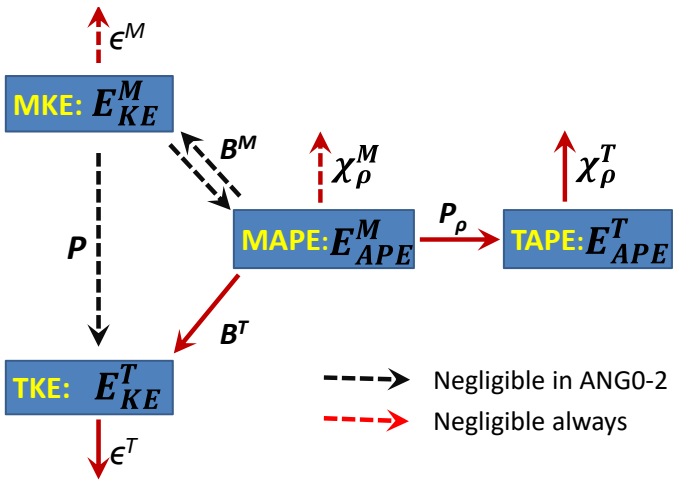

Figure 6.3: Schematic of energy pathways in flow over slope.

from MAPE to TKE and TAPE, which then gets dissipated. The loss in net energy (E_{loss} in (fig. 6.4c) increases rapidly after TAPE and TKE peak. About $3/4$ of the intial energy is dissipated in case ANG0-2. In contrast to the case with zero bottom slope, case ANG2.5-2 has significant MKE. The evolution of MAPE and MKE (fig. 6.4b) corresponds to a damped harmonic oscillator with frequency $2N\sin\beta$. During the oscillation, there is energy transfer to TKE and TAPE as well as dissipation. In this case, the bottom has a shallow slope so that the time period, $T = 2\pi/(N\sin\beta)$ is large ($NT = 144$) in terms of the buoyancy time scale. There is substantial dissipation during the first cycle with $E_{loss} \approx 60\%$ at $t = T$ (fig. 6.4d). The loss is entirely due to turbulence (primarily ε^T) with negligible contribution from mean dissipation and, furthermore, occurs at specific intervals during the oscillation. The underlying turbulence mechanism remains the same as in the non-sloping ANG0-2 case, i.e. convective instability, but the oscillatory nature of the flow causes convectively-unstable overturns at multiple phases of the cycle instead of the LCOE of ANG0-2. The largest burst of turbulence occurs at the end of each cycle as the near-bottom flow reverses from downslope to upslope.

A map of energy transfers in the problem is rendered in fig. 6.3. In all cases, the pathways of MAPE to TKE and MAPE to TAPE are active and responsible for dissipation in the system. The energy loss is dominated by dissipation of turbulent KE and APE; the direct

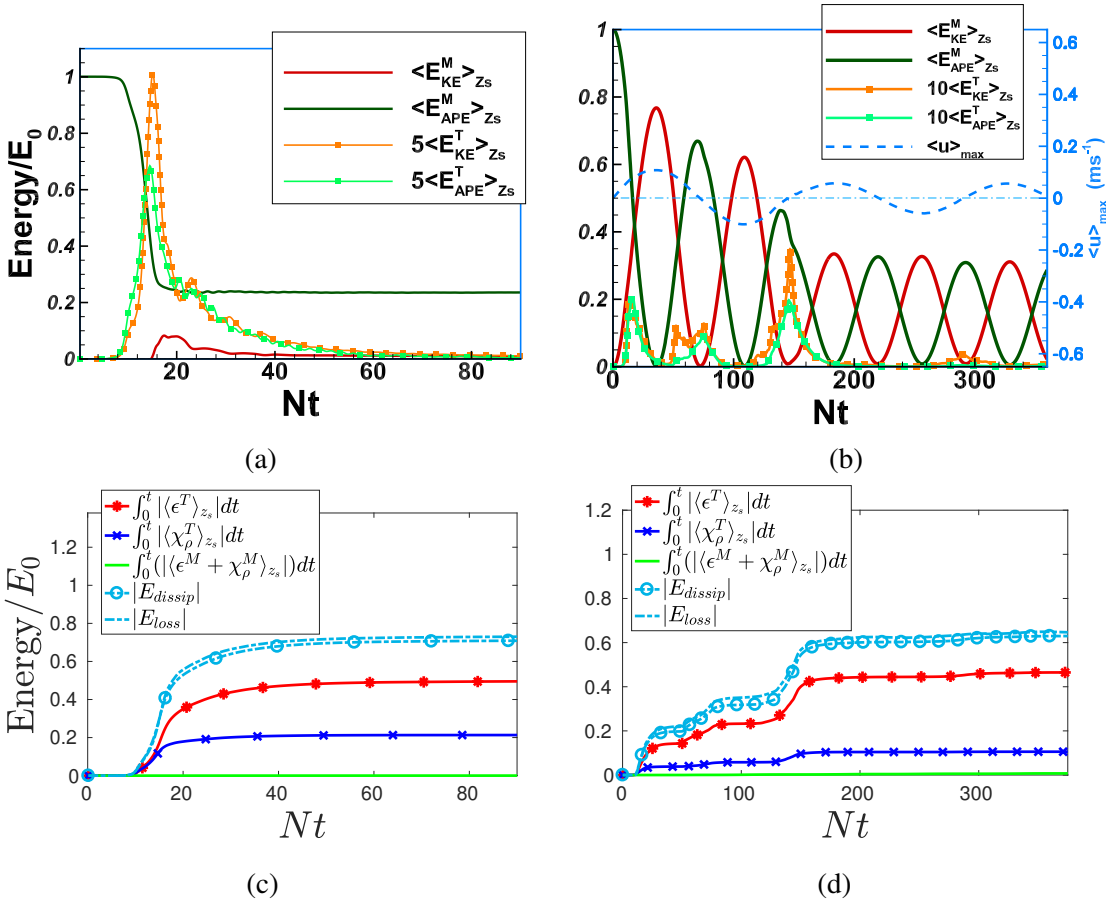

Figure 6.4: Time evolution of TKE, MKE, TAPE and MAPE averaged over z_s: (a) non-sloping case ANG0-2, (b) sloping case ANG2.5-2. The corresponding values of time-integrated dissipation terms are shown in (c) and (d).

dissipation of mean components is negligible. In the absence of slope, there is negligible MKE at all time. However in the sloping cases, there is a significant mean buoyancy flux that facilitates an oscillatory MKE-MAPE exchange. The mean flow also introduces a non-zero production (P) that additionally modulates TKE.

6.6 Mixing efficiency

The cumulative mixing efficiency (Γ defined by eq. (6.6)) is plotted in fig. 6.5. In the non-sloping case ANG0-2, Γ increases rapidly to its peak value of almost 0.8 before decreasing

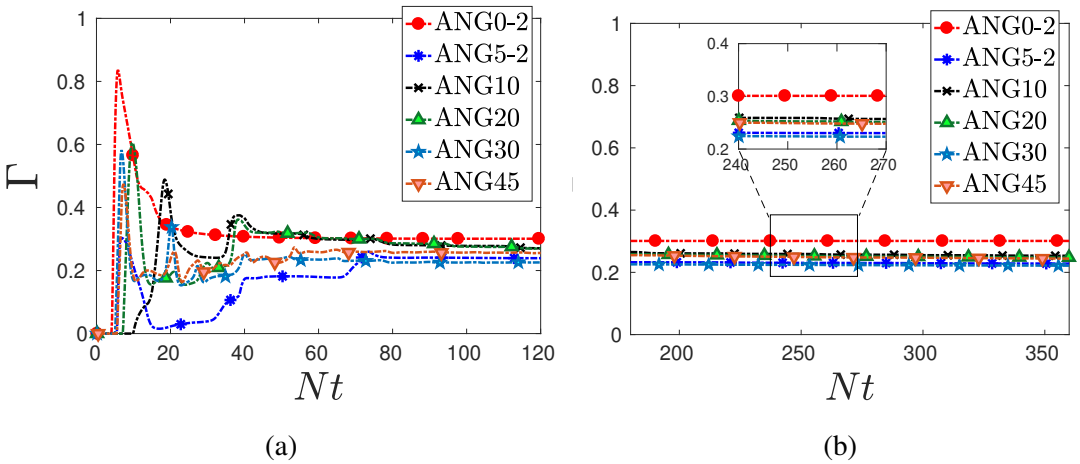

Figure 6.5: Mixing efficiency for all cases with $\rho_p = 0.02$ listed in table 6.1 and table 6.2 in two regimes: (a) CDL, (b) QSL

to about 0.3. This result is in agreement with a previous laboratory experiment of an unstable density interface immersed in a stable background Wykes and Dalziel (2014) where Γ was found to reach values that exceeded 0.75. Results from other numerical studies of oscillating flows with convective and shear driven turbulence, e.g. an oscillating stratified boundary layer on a slope (Chalamalla and Sarkar, 2015) and internal wave breaking at a pycnocline owing to parametric subharmonic instability (Gayen and Sarkar, 2014) have reported similar findings of $\Gamma > 0.2$, with the asymptotic values of Γ reaching 0.3 - 0.4 in most cases. The long-time Γ (fig. 6.5b) lies between 0.24-0.27, independent of the slope angle, when $\beta \neq 0$. The long-time Γ of 0.3 for the ANG0-2 case is somewhat higher. Based on the present simulations, the conventional assumption of $\Gamma = 0.2$ in parameterizations of ocean mixing may induce a bias when applied to situations with convectively driven mixing, e.g. internal waves at rough bathymetry.

Acknowledgements

This chapter, in full, is a reprint of the material as it appears in "Energetics and mixing in buoyancy-driven near-bottom stratified flow", P. Puthan, M. Jalali, V. K. Chalamalla and S. Sarkar, *Journal of Fluid Mechanics*, 869, 2019. The dissertation author is the primary investigator and author of this paper.

Chapter 7

Summary

The role of bottom topography in ocean dynamics has received increasing attention in recent years. The momentum transported by topographic internal waves acts as drag on the impinging flow, and the energy converted from the flow to internal waves acts as a source for both remote and local turbulent mixing. Concurrently, wakes are generated downstream when the flow flow separates at steep multiscale bathymetry (e.g. Buijsman et al., 2014). In previous studies, no-slip and slip BC have been employed to model the obstacle and bottom boundaries in numerical simulations (Rotunno et al., 1998; Ding and Street, 2002). Although, no-slip BC is the physically correct BC, the computational grid is too coarse to resolve the physical boundary layer at high Re_D. Therefore, slip BC or quadratic drag law BC (also known as partial-slip BC) are often employed to simulate geophysical wakes at high Re_D. In the first phase of the thesis research, the role of BC is explored in the wake of a conical obstacle in a uniformly stratified background. The topographic Froude number Fr_c is 0.2 and Reynolds number Re_D is 15000. Simulations of a steady current impinging on an idealized conical hill are conducted with no-slip (**NOSL**), slip (**SL**) and drag law (**DL**) BCs. A hybrid (**Hybrid**) case with no slip on the obstacle and slip at the flat bottom is also simulated.

During the encounter with the obstacle, the stratified flow at $Fr_c = 0.2$ exhibits up-

stream flow blocking, steady lee waves and flow separation followed by recirculation. These features are altered by changing the BC. In **NOSL**, the recirculation zone has a counter-rotating lee vortex pair with little unsteadiness while in **SL**, **DL** and **Hybrid**, counter-rotating vortices are shed off the body to form a Kármán vortex street. At this Re_D of 15000, bottom friction evidently exerts a strong constraint on the wake that reduces unsteadiness near the body in **NOSL**. It is only further downstream (x/D) that the wake develops a sinuous barotropic instability. On the other hand, shedding of vortices in **SL**, **DL** and **Hybrid** cases occur at a distinct frequency. This frequency does not vary with the vertical location. Spectra of streamwise (u) and lateral velocity (v) estimate this frequency as $St = f_{s,c}D/U_c = 0.26$. The boundary layers on the flat and sloping bottom are resolved in **NOSL**. Therefore, a laboratory experiment conducted with the present obstacle geometry and $Re_D = 15000$ and $Fr_c = 0.2$ would be expected to match the results of **NOSL** and not **SL**, **DL** and **Hybrid**. Indeed, for similar parameters of $Fr_c = 0.2$ and $Re_D = 13700$, (Hunt and Snyder, 1980) report a quasi-steady recirculation zone containing an attached counter-rotating vortex pair with some irregular unsteadiness in the wake. The drag coefficient associated with wall shear is ≈ 0.02, which is much larger than bottom drag estimates found in observation studies (e.g. MacKinnon et al., 2019). At high Re of geophysical wakes, **NOSL** is inappropriate because the viscous sublayer cannot be resolved and, therefore, a BC such as **DL** is appropriate.

The well known generators of lee wake vortices are boundary layer vorticity, curvature of the obstacle and baroclinicity. An unstratified simulation of the same flow in the presence of slip conditions at the boundary reveals a narrow wake where lee vortices are absent. Previous studies of unstratified simulations with no-slip boundary conditions reveal a standing horseshoe vortex and periodic shedding of hairpin vortices at low Re_D (Acarlar and Smith, 1987) and intermittent shedding of vortex patches at high Re_D (Garcia-Villalbaa et al., 2009). Therefore, stratification is necessary for formation of lee wake vortices of the type observed in geophysical wakes. In the presence of stratification, baroclinic torque (operative only in the balances for

horizontal vorticity components) is dominant, independent of the BC type. Vortex stretch and tilt are also substantial. The simulation result, namely, that horizontal vorticity is produced by the baroclinic torque and tilted into the vertical, supports the lee-vortex mechanism proposed by Smolarkiewicz and Rotunno (1989).

In the second phase, LES simulations of a tidally modulated current, $U_b = U_c + U_t \sin(2\pi f_t t)$, with a conical obstacle having base diameter D is examined on an f-plane. The quadratic drag law BC (**DL**) is applied at the obstacle and the flat bottom. The velocity ratio $R = U_c/U_t$ is fixed at 1, the Froude number Fr_c is 0.15 and the topographic Rossby number Ro_c is 5.5. With the addition of tides, the observed wake-vortex frequency (denoted as f_s) in the wake is altered from $f_{s,c}$ and found to be a function of the ratio between $f_{s,c}$ and the tidal frequency f_t, namely $f^* = f_{s,c}/f_t$. The relative frequency parameter $f^* = f_{s,c}/f_t$ is varied between 0.1 and 1. Below $f^* = 0.25$, the lee vortices are found at its natural value of $f_{s,c}$. When f^* approaches about 0.25, instead of the typical asymmetric shedding of vortex monopoles, vortices separate laterally from the obstacle from each side during every tidal cycle to form periodic vortex dipoles. These dipoles are unstable and break down within few diameters of the obstacle. A Kármán vortex street with asymmetrically placed vortices develops downstream, but with frequency f_s in the wake altered from $f_{s,c}$ to $f_t/4$. This synchronization to $f_t/4$ is observed when $0.25 \leq f^* < 0.5$.

When $0.5 \leq f^* \leq 1$, wake vortices appear at the first subharmonic of the tidal frequency, i.e the wake synchronizes to $f_t/2$. The periodicity and lateral symmetry imposed by the tidal forcing on the near wake is different from the spatio-temporal symmetry of a Kármán vortex street. As a result of tidal synchronization, the spatio-temporal symmetry of a Kármán wake is re-established while respecting the temporal periodicity of the tide by modifying the wake-vortex frequency to $f_t/(2n)$ $(n = 1, 2)$. While $f_t/2$ is the preferred frequency of wake vortices for cases with $0.5 \leq f^* \leq 1$, the value of $f_t/4$ is the preferred frequency when $0.25 \leq f^* < 0.5$. It is interesting that tidal oscillations that are faster than natural shedding act to slow down the

observed frequency through synchronization to a tidal subharmonic.

Tides, by altering the wake vortex frequency, also have an effect on the form drag as well as wake turbulence. When $U_t = U_c$, vortices in an abyssal hill wake can be found at frequencies $f_{s,c}$, $f_t/4$ or $f_t/2$ on varying the relative frequency $f^* = f_{s,c}/f_t$. These three regimes of vortex dynamics are explored to reveal states of high time averaged form drag $\langle F_D \rangle$. Results demonstrate a twofold amplification of $\langle F_D \rangle$ relative to the no-tide ($U_t = 0$) case when f^* lies between 0.5 and 1. When $0.25 \leq f^* < 0.5$, the amplification in drag is approximately 60%. This amplification stems from bottom intensified low pressure zones in the obstacle lee. These low pressure zones are associated with large vortical regions close to the boundary. For example, when $f^* = 5/6$, these vortices have sufficient time to develop and grow in the lee. They induce a pressure drop and remain attached to the obstacle during the entire tidal cycle, thereby supporting the pressure drop over a longer duration and amplifying $\langle F_D \rangle$. However, when $f^* = 2/15$, the rapidly varying tide-associated pressure gradient restricts the size of the low pressure zone in the lee.

Notable changes also occur in the spatial organization of the near-wake vortices in these high drag states. When $f^* = 2/15$, vortex pulses which occur every tidal cycle, feed vorticity into a larger eddy in the recirculation zone. These larger eddies form a Kármán vortex wake downstream. At $f^* = 5/12$, laterally symmetric eddy dipoles are shed in the near wake. The lateral symmetry is controlled by the tidal flow up to a streamwise distance of U_t/f_t. Beyond this location, the vortices partially break down or merge to create a disorganized wake downstream. This event is accompanied by a change in the wake vortex frequency from f_t to $f_t/4$. At $f^* = 5/6$, strong asymmetric shedding at a frequency of $f_t/2$ is observed in the entire wake. The wake is laterally wider in comparison to the other regimes. The timing of the shed vortices is strongly influenced by the barotropic tidal oscillation. When $|\omega_z|$ is volume-averaged over the wake, its temporal variation is affected by the tidal oscillation. At $f^* = 2/15$, the temporal evolution is in phase with tides owing to the formation of vortex

pulses. On the other hand, at $f^* = 5/12$, the temporal evolution is out of phase with the tidal oscillation. Excess vorticity is added to the wake from the lateral motion of recirculating fluid and the attendant shear-layer roll-up during the low-velocity phase.

Tidal synchronization can also occur when the amplitude of tidal modulations are small relative to the mean flow. In th regime of $0 < R \leq 1$, tidal modulations tend to slow down the frequency of shed vortices by delaying the vortex separation during the deceleration phase of the tidal cycle and trapping it in the recirculation zone. For example, when $R = 0.2$, the vortices detach from the hill and move into the wake only during the tidal acceleration phase of each cycle. The momentum loss associated with the tidal forcing prevents migration of vortices into the wake during the deceleration phase when $R \geq 0.2$. This process is controlled by the tidal strength parameter $\overline{S} = R/Ex_c$. A significant reduction (larger than 10%) in the vortex shedding frequency is observed when $\overline{S}$ is larger than 0.28. When $0.4 \leq \overline{S} \leq 2$, the tidal forcing exerts control on the frequency of shed vortices by permitting vortex of a single sign to shed every tidal cycle. As a result, vortices are shed at a frequency equal to the tidal subharmonic.

Internal-wave (IW) driven turbulence is also a large energy sink in the abyssal ocean. In the third phase of this study, we examine the evolution of a patch of unstably stratified fluid induced by IW propagation over a sloping bottom. The presence of a slope leads to a current that oscillates with frequency of $N \sin\beta$ and qualitatively changes the subsequent evolution of the initial density disturbance. The flow evolution involves energy exchange between four major energy reservoirs, namely the mean and turbulent counterparts of kinetic energy (KE) and available potential energy (APE). In the presence of a sloping bottom, the energy transfer is dominated by an oscillatory exchange between mean APE and mean KE with frequency of $2N \sin\beta$, where N is the buoyancy frequency and β is the slope angle with the horizontal. Some energy is also transferred to turbulence. In the absence of a slope, energy transfer occurs from mean APE to turbulent KE and turbulent APE. A key result is that, in contrast to the

explosive loss of energy during the initial convective instability in the non-sloping case, the sloping cases exhibit a more gradual energy loss to turbulence that is sustained over a long time interval. For moderate slopes with $\beta < 10^{\circ}$, most of the net energy loss takes place during an initial, short $Nt \approx 20$ interval with periodic convective overturns. For steeper slopes, most of the energy loss takes place during a later, long ($Nt > 100$) interval when both shear and convective instability occur, and the energy loss rate is approximately constant. The mixing efficiency during the period dominated by convectively driven turbulence is found to be substantially higher than the widely used value of 0.2.

Future directions

During flow-topography interactions, multiple time scales emerge in the $R - Ex_c$ parameter space. Owing to the statistically stationary nature (meaning that the mean and variance do not change in time) of the flow, techniques such as proper orthogonal decomposition (POD) (Lumley, 1970) or its spectral counterpart (SPOD) (Schmidt and Colonius, 2020) have shown promise in capturing the coherent structures. For example, SPOD has been extensively applied to simulations of compressible jets (Towne et al., 2018; Nekkanti and Schmidt, 2021) and recently to unstratified and stratified bluff body wakes (Nidhan et al., 2020, 2021). Therefore, application of such modal decomposition techniques to extract the spatial and temporal flow features in geophysical wakes is an essential follow up.

Bibliography

Acarlar, M. S. and Smith, C. R. (1987). A study of hairpin vortices in a laminar boundary layer. Part 1. Hairpin vortices generated by a hemisphere protuberance. *J. Fluid Mech.*, 89:1–41.

Alford, M. H., Klymak, J. M., and Carter, G. S. (2014). Breaking internal lee waves at Kaena Ridge, Hawaii. *Geophys. Res. Lett.*, 41:906–912.

Alford, M. H., MacKinnon, J. A., Nash, J. D., Simmons, H., Pickering, A., Klymak, J. M., Pinkel, R., Sun, O., Rainville, L., Musgrave, R., Beitzel, T., Fu, K., and Lu, C. (2011). Energy flux and dissipation in Luzon Strait: Two tales of two ridges. *J. Phys. Oceanograph.*, 41:2211–2222.

Alford, M. H., Peacock, T., et al. (2015). The formation and fate of internal waves in the South China Sea. *Nature*, 521(65):0028–0836.

Aucan, J., Merrifield, M. A., Luther, D. S., and Flament, P. (2006). Tidal mixing events on the deep flanks of Kaena Ridge, Hawaii. *J. Phys. Oceanogr.*, 36:1202–1219.

Baines, P. G. (1995). Topographic Effects in Stratified Flows. *Cambridge University Press*, 482.

Barbi, C., Favier, D., Maresca, C., and Telionis, D. (1986). Vortex shedding and lock-on of a cylinder in oscillatory flow. *J. Fluid Mech.*, 170:527–544.

Becherer, J. and Umlauf, L. (2011). Modelling the effect of shear-induced convection. *J. Geophys. Res.*, 116:C10017.

Beckmann, A. and Haidvogel, D. B. (1997). A numerical simulation of flow at Fieberling Guyot. *J. Geophys. Res.*, 102:5595–5613.

Bell, T. (1975). Lee waves in stratified fluid with simple harmonic time dependence. *J. Fluid Mech.*, 67:705–722.

Black, K. and Gay, S. (1987). Eddy formation in unsteady flows. *J. Geophys. Res.*, 92:9514–9522.

Bluteau, C. E., Jones, N. L., and Ivey, G. N. (2011). Dynamics of a tidally forced stratified

shear flow on the continental slope. *J. Geophys. Res.*, 116:C11017.

Buijsman, M., Klymak, J. M., Legg, S., Alford, M., Farmer, D., Mackinnon, J. A., Nash, J. D., Park, J., Pickering, A., and Simmons, H. (2014). Three-dimensional double-ridge internal tide resonance in Luzon Strait. *J. Phys. Oceanogr.*, 44:850–869.

Buijsman, M., Legg, S., and Klymak, J. M. (2012). Double-ridge internal tide interference and its effect on dissipation in Luzon Strait. *J. Phys. Oceanogr.*, 42:1337–1356.

Caldeira, R. M. A., Marchesiello, P., Nezlin, N. P., DiGiacomo, P. M., and McWilliams, J. C. (2005). Island wakes in the Southern California Bight. *J. Geophys. Res.*, 110:C11012.

Callendar, W., Klymak, J., and Foreman, M. (2011). Tidal generation of large sub-mesoscale eddy dipoles. *Ocean Science*, 7(4):487.

Canals, M., Pawlak, G., and MacCready, P. (2008). Tilted baroclinic tidal vortices. *J. Phys. Oceanograph.*, 39:333–350.

Chalamalla, V., Santilli, E., Scotti, A., Jalali, M., and Sarkar, S. (2017). SOMAR-LES: A framework for multi-scale modeling of turbulent stratified oceanic flows. *Ocean Modelling*, 120:101–119.

Chalamalla, V. and Sarkar, S. (2015). Mixing, dissipation rate and their overturn-based estimates in a near-bottom turbulent flow driven by internal tides. *J. Phys. Oceanogr.*, 45:1969–1987.

Chang, M., Jan, S., Liu, C., Cheng, Y., and Mehsah, V. (2019). Observations of island wakes at high Rossby numbers: Evolution of submesoscale vortices and free shear layers. *J. Phys. Oceanograph.*, 49:2997–3016.

Chen, G., Wang, D., Dong, C., Zu, T., Xue, H., Shu, Y., Chu, X., and Chen, H. (2015). Observed deep energetic eddies by seamount wake. *Scientic Reports*, 5:17416:1–10.

Coutis, P. F. and Middleton, J. H. (2002). The physical and biological impact of a small island wake in the deep ocean. *Deep Sea Res. I*, 49:1341–1361.

Cusack, J., Garabato, A. C. N., Smeed, D. A., and Girton, J. B. (2017). Observation of large lee wave in the Drake passage. *J. Phys. Oceanograph.*, 47:793–810.

Dalziel, S., Patterson, M., Caulfield, C., and Brun, S. (2011). The structure of low-Froude-number lee waves over an isolated obstacle. *J. Fluid Mech.*, 689:3–31.

Denniss, T., Middleton, J. H., and Manasseh, R. (1995). Recirculation in the lee of complicated headlands: A case study of Bass Point . *J. Geophys. Res.*, 100:16087–16101.

Dewey, R. K. and Crawford, W. R. (1988). Bottom stress estimates from vertical dissipation rate profiles on the continental shelf. *J. Phys. Oceanograph.*, 18:1167–1177.

Dietrich, D. E., Bowman, M. J., Lin, C. A., and Mestasnunez, A. (1996). Numerical Studies of Small Island Wakes in the Ocean. *Geophysical & Astrophysical Fluid Dynamics*, 83:195–231.

Ding, L., Calhoun, R. J., and Street, R. L. (2003). Numerical Simulation of strongly stratified flow over a three-dimensional hill . *Boundary-Layer Meteorology*, 107:81–114.

Ding, L. and Street, R. L. (2002). Numerical Study of the Wake Structure behind a Three-Dimensional Hill. *Journal of Atmospheric Sciences*, 60:1678–1690.

Dong, C. and McWilliams, J. C. (2007). A numerical study of island wakes in the Southern California Bright. *Continental Shelf Res.*, 27:1233–1248.

Dong, C., McWilliams, J. C., and Shchepetkin, A. F. (2006). Island wakes in deep water. *J. Phys. Oceanograph.*, 37:962–981.

Dong, C., McWilliams, J. C., and Shchepetkin, A. F. (2007). Island wakes in shallow water. *J. Phys. Oceanograph.*, 37:962–981.

Drazin, P. (1961). On the steady flow of a fluid of variable density past an object. *Tellus*, 13(2).

Edwards, K. A., MacCready, P., Moum, J. M., Pawlak, G., Klymak, J. M., and Perlin, A. (2004). Form drag and mixing due to tidal flow past a sharp point . *J. Phys. Oceanograph.*, 34:1297–1312.

Egbert, G. D. and Ray, R. D. (2000). Significant dissipation of tidal energy in the deep ocean inferred from satellite altimeter data. *Nature*, 405:775–778.

Egbert, G. D. and Ray, R. D. (2001). Estimates of M2 tidal energy dissipation from TOPEX/POSEIDON altimeter data. *J. Geophys. Res.*, 106(22):475–502.

Epifanio, C. C. and Durran, D. R. (2001). Three-dimensional effects in high-drag-state flows over long ridges. *J. Atmos. Sci.*, 58:1051–1065.

Epifanio, C. C. and Rotunno, R. (2005). Dynamics of Orographic wake formation in flows with Upstream blocking. *J. Atmos. Sci.*, 62:3127–3150.

Garabato, A. C. N., Williams, E. E. F., Spingys, C. P., Legg, S., Polzin, K. L., Forryan, A., Abrahamsen, E. P., Buckingham, C. E., Griffies, S. M., McPhil, S. D., Nicholls, K. W., Thomas, L. N., and Meredith, M. P. (2019). Rapid mixing and exchange of deep-ocean waters in an abyssal boundary current. *Proceedings of the National Academy of Sciences*, 116(27):13233–13238.

Garcia-Villalbaa, M., Li, N., Rodi, W., and M.A.Leschziner (2009). Large eddy simulaation of seperated flow over a three-dimensional axisymmetric hill . *J. Fluid Mech.*, 627:55–96.

Garrett, C. and Kunze, E. (2007). Internal tide generation in the deep ocean. *Annual Review*

of Fluid Mechanics, 39:57–87.

Gayen, B. and Sarkar, S. (2011). Direct and large-eddy simulations of internal tide generation at a near-critical slope. *J. Fluid Mech.*, 681:48–79.

Gayen, B. and Sarkar, S. (2014). PSI to turbulence during internal wave beam refraction through the upper ocean pycnocline. *Geophys. Res. Lett.*, 41:8953–8960.

Germano, M., Piomelli, U., Moin, P., and Cabot, W. H. (1991). A dynamic subgrid-scale eddy viscosity model. *Phys. Fluids A*, 3(7):1760–1765.

Gill, A. E. (1982). *Atmosphere–Ocean dynamics*. Academic Press.

Girton, J., Mickett, J., Zhao, Z., Alford, M., Voet, G., Cusack, J., Carter, G., Pearson-Potts, K., Pratt, L., Tan, S., and Klymak, J. M. (2019). Flow-topography interactions in the Samoan Passage. *Oceanography*, 32(4):184–193.

Griffin, O. M. and Hall, M. S. (1991). Review-vortex shedding lock-on and flow control in bluff body wakes. *Journal of Fluids Engineering, Transactions of the ASME*, 113(4):526–537.

Gula, J., Molemaker, M., and McWilliams, J. C. (2015). Topographic vorticity generation, submesoscale instability and vortex street formation in the gulf stream. *Geophys. Res. Letters*, 42:4054–4062.

Hasegawa, D., Yamazaki, H., Lueck, R. G., and Seuront, L. (2004). How islands stir and fertilize the upper ocean. *Geophys. Res. Lett.*, 31:L16303.

Holloway, P. E. and Merrifield, M. A. (1999). Internal tide generation by seamounts, ridges, and islands. *J. Geophys. Res.*, 104:25937–25951.

Howritz, R. W., Taylor, S., Lu, Y., Paquin, J., Schillinger, D., and Greenberg, D. A. (2021). Rapid reduction of tidal amplitude due to form drag in a narrow channel. *Continental Shelf Res.*, 213:104299.

Hunt, J. and Snyder, W. (1980). Experiments on stably and neutrally stratified flow over a model three-dimensional hill. *J. Fluid Mech.*, 96:671–704.

Isugachi, O., Shimada, M., Sakaida, F., and Kawamura, H. (2009). Investigation of Kuroshio-induced cold-core eddy trains in the lee of the Izu Islands using high-resolution satellite images and numerical simulations. *Remote sensing and environment*, 113:1912–1925.

Jalali, M., Rapaka, N. R., and Sarkar, S. (2014). Tidal flow over topography: effect of excursion number on wave energetics and turbulence. *J. Fluid Mech.*, 750:259 – 283.

Jalali, M. and Sarkar, S. (2017). Large eddy simulation of flow and turbulence at the steep topography of Luzon Strait. *Geophys. Res. Lett.*, 44(18).

Jalali, M., VanDine, A., Chalamalla, V. K., and Sarkar, S. (2017). Oscillatory stratified flow over supercritical topography: Wave energetics and turbulence. *Computers & Fluids*, 158:39–48.

Jayne, S. R. and Laurent, L. (2001). Parameterizing tidal dissipation over rough topography. *Geophys. Res. Lett.*, 28(5):811–814.

Keulegan, G. H. and Carpenter, L. H. (1958). Forces on cylinders and plates in an oscillating fluid. *American Society of Mechanical Eng.*, 60(5):423–440.

Kimura, S., Choo, H. S., and Suginoto, T. (1994). Characteristics of the eddy caused by lzu-Oshima Island and the Kuroshio Branch Current in Sagami Bay, Japan . *J. Oceanogrph.*, 50:373–389.

King, B., Zhang, H. P., and Swinney, H. L. (2009a). Tidal flow over three-dimensional topography in a stratified fluid. *Phys. Fluids*, 21:116601.

King, B., Zhang, H. P., and Swinney, H. L. (2010). Tidal flow over threedimensional topography generates outofforcingplane harmonics. *Geophys. Res. Lett.*, 37:L14606.

King, E. M., Stellmach, S., Noir, J., Hansen, U., and Aurnou, J. M. (2009b). Boundary layer control of rotating convection systems. *Nature*, 457(7227):301.

Klymak, J. M. (2018). Nonpropagating form drag and turbulence due to stratified flow over large scale abyssal hill topography. *J. Phys. Oceanograph.*, 48:2383–2395.

Klymak, J. M., Legg, S., and Pinkel, R. (2010a). A simple parameterization of turbulent tidal mixing near supercritical topography. *J. Phys. Oceanograph.*, 40:2059–2074.

Klymak, J. M., Moum, J. N., Nash, J. D., Kunze, E., Girton, J. B., Carter, G. S., Lee, C. M., Sanford, T. B., and Gregg, M. C. (2006). An estimate of tidal energy lost to turbulence at the Hawaiian Ridge. *J. Phys. Oceanogr.*, 36:1148–1164.

Klymak, J. M., Pinkel, R., and Legg, S. (2010b). High-mode stationary waves in stratified flow over large obstacles. *J. Fluid Mech.*, 644:321–336.

Konstantinidis, E. and Balabani, S. (2007). Symmetric vortex shedding in the near wake of a circular cylinder due to streamwise perturbations. *Journal of Fluids and Structures*, 23(7):1047–1063.

Konstantinidis, E. and Liang, C. (2011). Dynamic response of a turbulent cylinder wake to sinusoidal inflow perturbations across the vortex lock-on range. *Phys. Fluids*, 23(7).

Lamb, H. (1930). *Hydrodynamics*. Cambridge University Press.

Lamb, K. G. (2014). Internal wave breaking and dissipation mechanisms on the continental slope/shelf. *Annual Review of Fluid Mechanics*, 46:231–254.

Lamb, K. G. and Dunphy, M. (2018). Internal wave generation by tidal flow over a two-dimensional ridge: Energy flux asymmetries induced by a steady surface trapped current. *Journal of Fluid Mechanics*, 836:192–221.

Laurent, L. C. S. and Garrett, C. (2002). The role of internal tides in mixing the deep ocean. *J. Phys. Oceanogr.*, 32:2882–2899.

Leal, L. G. (1989). Vorticity transport and wake structure for bluff bodies at finite Reynolds number. *Physics of Fluids A*, 1:124–131.

Ledwell, J. R., Montgomery, E. T., Polzin, K. L., Laurent, L. C. S., Schmitt, R. W., and Toole, J. M. (2000). Evidence for enhanced mixing over rough topography in the abyssal ocean. *Nature*, 403:179–182.

Legendre, D., Luaga, E., and Magnauet, J. (2009). Influnce of slip on the dynamics of two-dimensional wakes. *J. Fluid Mech.*, 633:437–447.

Legg, S. (2021). Mixing by oceanic lee waves. *Ann. Rev. Fluid Mech.*, 53:173–201.

Legg, S. and Klymak, J. M. (2008). Internal hydraulic jumps and overturning generated by tidal flows over a tall steep ridge. *J. Phys. Oceanogr.*, 38:1949–1964.

Leo, L. S., Thompson, M. Y., Di Sabatino, S., and Fernando, H. J. (2016). Stratified flow past a hill: dividing streamline concept revisited. *Boundary-layer meteorology*, 159(3):611–634.

Lesieur, M. (2008). *Turbulence in Fluids*. Springer.

Lighthill, J. (1986). Fundamentals concerning wave loading on offshore structures. *J. Fluid Mech.*, 173:667–681.

Lilly, D. K. (1992). A proposed modification of the germano subgrid-scale closure method. *Phys. Fluids A: Fluid Dynamics*, 4(3):633–635.

Lin, J. T. and Pao, Y. H. (1979). Wakes in stratified fluids: a review. *Ann. Rev. Fluid Mech.*, 11:317–338.

Liu, C. and Chang, M. (2018). Numerical studies of submesoscale island wakes in the Kuroshio. *J. Geophys. Res.*, 123:5669–5687.

Lorke, A., Umlauf, L., and Mohrholz, V. (2015). Straatification and mixing on sloping boundaries. *Geophys. Res. Letters*, 35:L14610.

Lumley, J. L. (1970). *Stochastic Tools in Turbulence*. Academic Press.

MacCready, P. and Pawlak, G. (2001). Stratified flow along a Corrugated Slope: Separation Drag and Wave Drag . *J. Phys. Oceanograph.*, 31:2824–2839.

MacKinnon, J. A., Alford, M. H., Voet, G., Zeiden, K., Johnston, T. M. S., Siegelman, M.,

Merrifield, S., and Merrifield, M. (2019). Eddy wake generation from broadband currents near Palau. *J. Geophys. Res.*, 124:4891–4903.

Magaldi, M. G., Ozgokmen, T. M., Griffa, A., Chassignet, E. P., Iskandarani, M., and Peters, H. (2008). Turbulent flow regimes behind a coastal cape in a stratified and rotating environment. *Ocean Modelling*, 25:65–82.

Marques, O., Alford, M. H., Pinkel, R., k, J. A. M., Klymak, J. M., Nash, J. D., Waterhouse, A. F., Kelly, S. M., Simmons, H. L., and Braznikov, D. (2021). Internal tide structure and temporal variability on the reflective continental slope of Southeastern Tasmania. *J. Phys. Oceanograph.*, 51:611–631.

Mashayek, A., Ferrari, R., Merrifield, S., Ledwell, J., Laurent, L. S., and Garabato, A. N. (2017). Topographic enhancement of vertical turbulent mixing in the southern ocean. *Nature Communications*, 8:14197.

Maslowe, S. A. (1991). Barotropic instability of the Bickley jet. *J. Fluid Mech.*, 229:417–426.

McCabe, R. M., MacCready, P., and Pawlak, G. (2006). Form Drag due to Flow Separation at a Headland. *J. Phys. Oceanograph.*, 36:2136–2152.

Meneveau, C., Lund, T. S., and Cabot, W. H. (1996). A lagrangian dynamic subgrid-scale model of turbulence. *J. Fluid Mech.*, 19(3):353–385.

Molemaker, J., McWilliams, J. C., and Dewar, W. K. (2015). Submesoscale instability and generation of mesoscale anticyclones near a separation of the California undercurrent. *J. Phys. Oceanograph.*, 45:613–629.

Morison, J. R., Johnson, J. W., and Schaaf, S. A. (1950). The force exerted by surface waves on piles. *J. of Petroleum Tech.*, 2(5):149–154.

Munk, W. and Wunsch, C. (1998). Abyssal recipes ii: energetics of tidal and wind mixing. *Deep-Sea Res. I*, 45:1977–2010.

Munroe, J. R. and Lamb, K. G. (2005). Topographic amplitude dependence of internal wave generation by tidal forcing over idealized three-dimensional topography . *J. Geophys. Res.*, 110.

Musgrave, R. C., Mackinnon, J. A., R.Pinkel, and Waterhouse, A. F. (2016). Tidally driven processes leading to near-field turbulence in a channel at the crest of the Mendocino Escarpment. *J. Phys. Oceanograph.*, 46:1137–1155.

Musgrave, R. C., Mackinnon, J. A., R.Pinkel, Waterhouse, A. F., Nash, J., and Kelly, S. M. (2017). The influence of subinertial internal tides on near topographic turbulence at the Mendocino Ridge: observations and modeling. *J. Phys. Oceanograph.*, 47:2139–2154.

Nash, J. D. and Moum, J. N. (2001). Internal hydraulic flows on the continental shelf: High

drag states over a small bank. *J. Geophys. Res.*, 106:4593–4612.

Nekkanti, A. and Schmidt, O. T. (2021). Frequency-time analysis, low-rank reconstruction and denoising of turbulent flows using SPOD . *J. Fluid Mech.*, page A26.

Nicoud, F. and Ducros, F. (1999). Subgrid-scale stress modelling based on the square of the velocity gradient tensor flow. *Turbulence and Combustion*, 62(3):183–200.

Nidhan, S., Chongsiripinyo, K., Schmidt, O. T., and Sarkar, S. (2020). Spectral proper orthogonal decomposition analysis of the turbulent wake of a disk at Re=50000 . *Phys. Rev. Fluids*, 5(12):124606.

Nidhan, S., Schmidt, O. T., and Sarkar, S. (2021). Coherence in turbulent stratified wakes deduced using spectral proper orthogonal decomposition . *arXiv:2105.06656*.

Nikurashin, M. and Ferrari, R. (2010). Radiation and dissipation of internal waves generated by geostrophic flows impinging on small scale topography: Application to the Southern Ocean. *J. Phys. Oceanograph.*, 40:2025–2042.

Nikurashin, M. and Legg, S. (2011). A mechanism for local dissipation of internal tides generated at rough topography. *J. Phys. Oceanograph.*, 41:378–395.

Pawlak, G., MacCready, P., Edwards, K. A., and McCabe, R. (2003). Observations on the evolution of tidal vorticity at a stratified deep water headland. *Geophys. Res. Lett.*, 30:2234.

Peacock, T., Stcker, R., and Aristoff, J. (2004). An experimental investigation of the angular dependence of diffusion-driven flow. *Phys. Fluids*, 16(9).

Perfect, B., Kumar, N., and Riley, J. (2018). Vortex structures in the wake of an idealized seamount in rotating, stratified flow. *Geophysical research letters*, pages 9098–9105.

Perfect, B., Kumar, N., and Riley, J. (2020). Energetics of seamount wakes. Part 1: Energy Exchange . *J. Phys. Oceanograph.*, 50(5):1365–1382.

Perret, G., Dubos, T., and Stegner, A. (2011). How Large-Scale and Cyclogeostrophic Barotropic Instabilities Favor the Formation of Anticyclonic Vortices in the Ocean. *J. Phys. Oceanogr.*, 41:303–328.

Phillips, O. M. (1970). On flows induced by diffusion in a stably stratified fluid. *Deep-Sea Res. I*, 17:435–443.

Phillips, O. M., Shyu, J., and Salmun, H. (1986). An experiment on boundary mixing: mean circulation and transport rates. *J. Fluid Mech.*, 173:473–499.

Pinkel, R., Buijsman, M., and Klymak, J. M. (2012). Breaking topographic lee waves in a tidal channel in Luzon Strait. *Oceanography*, 25:160–165.

Polzin, K. L., Garabato, A. C. N., Abrahamsen, E. P., Jullion, L., and Meredith, M. P. (2014). Boundary mixing in Orkney Passage outflow. *J. Geophys. Res.*, 119:8627–8645.

Polzin, K. L., Toole, J. M., Ledwell, J. R., and Schmitt, R. W. (1997). Spatial variability of turbulent mixing in the abyssal ocean. *Science*, 276:93–96.

Puthan, P., Jalali, M., Chalamalla, V. K., and Sarkar, S. (2019). Energetics and mixing in buoyancy-driven near-bottom stratified flow. *J. Fluid Mech.*, 869:214–237.

Puthan, P., Jalali, M., Ortiz-Tarin, J. L., Chongsiripinyo, K., Pawlak, G., and Sarkar, S. (2020). The wake of a three-dimensional underwater obstacle: Effect of bottom boundary conditions. *Ocean Modelling*, 149:101611.

Puthan, P., Sarkar, S., and Pawlak, G. (2021a). High drag states in tidally distorted wakes . *arXiv:2109.04514*.

Puthan, P., Sarkar, S., and Pawlak, G. (2021b). Tidal synchronization of lee vortices in geophysical wakes. *Geophys. Res. Lett.*, 48.

Rapaka, N. R., Gayen, B., and Sarkar, S. (2013). Tidal conversion and turbulence at a model ridge: direct and large eddy simulations. *J. Fluid Mech.*, 715:181–209.

Rapaka, N. R. and Sarkar, S. (2016). An immersed boundary method for direct and large eddy simulation of stratified flows in complex geometry. *J. Comp. Phys.*, 322:511–534.

Ritchet, O., Muller, C., and Chomaz, J. (2019). Impact of a mean current on the internal tide energy dissipation at the critical latitude. *J. Phys. Oceanograph.*, 47:1457–1472.

Rosso, I., Hogg, A. M., Kiss, A. E., and Gayen, B. (2015). Topographic influence on submesoscale dynamics in the Southern Ocean. *Geophys. Res. Lett.*, 42:1139–1147.

Rotunno, R., Grubisic, V., and Smolarkiewicz, P. K. (1998). Vorticity and potential vorticity in mountain wakes. *J. Atmos. Sciences*, 56:2796–2808.

Ruan, X., Thompson, A. F., Flexas, M. M., and Sprintall, J. R. (2017). Contribution of topographically generated submesoscale turbulence to Southern Ocean overturning. *Nature Geoscience*, 10:840–846.

Rudnick, D. L., Zeiden, K. L., Ou, C. Y., Johnston, T. M. S., MacKinnon, J. A., Alford, M. H., and Voet, G. (2019). Understanding vorticity caused by flow passing an island. *Oceanography*, 32(4):66–73.

Saenko, O. A. and Merryfield, W. J. (2004). On the effect of topographically enhanced mixing on the global ocean circulation. *J. Phys. Oceanograph.*, 35:826–834.

Sarkar, S. and Scotti, A. (2017). From topographic internal gravity waves to turbulence. *Annu. Rev. Fluid Mech.*, 49:195–220.

Sarpkaya, T. (2001). On the force decompositions of Lighthill and Morrison. *J. Fluids and Structures*, 15:227–233.

Sarpkaya, T. (2004). A critical review of the intrinsic nature of vortex-induced vibrations. *J. Fluids and Structures*, 19:389–447.

Schar, C. and Durran, D. R. (1996). Vortex formation and vortex shedding in continuosly stratified flows past isolated topography. *J. Atmos. Sciences*, 54:534–554.

Schmidt, O. T. (2020). Bispectral mode decomposition of nonlinear flows. *Nonlinear Dynamics*, 102:2549–2501.

Schmidt, O. T. and Colonius, T. (2020). Guide to Spectral Proper Orthogonal Decomposition . *AIAA Journal*, pages 1023–1033.

Shakespeare, C. J. and Hogg, A. M. (2019). On the momentum flux of internal tides. *J. Phys. Oceanograph.*, 49:993–1013.

Sheppard, P. A. (1956). Airflow over mountains. . *Q J R Meteorol Soc*, 82:528–529.

Signell, R. P. and Geyer, W. R. (1991). Transient eddy formation around headland. *J. Geophys. Res.*, 96:2561–2575.

Smith, R. B. (1989). Comment on "Low froude number flow past three-dimensional obstacles. Part-I Baroclinically generated Lee vortices" . *J. Atmos. Sciences*, pages 3611–3613.

Smith, R. B. and Grubisic, V. (1993). Aerial observations of hawaii's wake. *J. Atmos. Sci.*, 50(22):3728–3750.

Smolarkiewicz, P. K. and Rotunno, R. (1989). Low froude number flow past three-dimensional obstacles. part-i baroclinically generated lee vortices. *J. Atmos. Sciences*, 46(8):1154–1164.

Snyder, W., Thompson, R. S., Eskridge, R. E., Lawson, R. E., Castro, I., Lee, J., Hunt, J., and Ogawa, Y. (1985). The structure of strongly stratified flow over hills: dividing-streamline concept. *Journal of Fluid Mechanics*, 152:249–288.

Sohail, T., Gayen, B., and Hogg, A. M. (2018). Convection enhances mixing in the southern ocean. *Geophys. Res. Lett.*, 45:4198–4207.

Srinivasan, K., McWilliams, J. C., Molemaker, J., and Barkan, R. (2018). Submesoscale vortical wakes in the lee of the topography. *J. Phys. Oceanograph.*, 49:1949–1971.

Thorpe, S. (1994). Statically unstable layers produced by overturning internal gravity waves. *J. Fluid Mech.*, 260:333–350.

Towne, A., Schmidt, O. T., and Colonius, T. (2018). Spectral proper orthogonal decomposition and its relationship to dynamic mode decomposition and resolvent analysis . *J. Fluid Mech.*,

pages 821–867.

Venayagamoorthy, S. K. and Fringer, O. B. (2007). On the formation and propagation of nonlinear internal boluses across a shelf break. *J. Fluid. Mech.*, 577:137–159.

Vic, C., Roullet, G., Capet, X., Carton, X., Molemaker, J., and Gula, J. (2015). Eddy-topography interactions and the fate of Persian Gulf outflow. *J. Geophys. Res.*, 120:6700–6717.

Voet, G., Alford, M. H., MacKinnon, J. A., and Nash, J. D. (2020). Eddy wake generation from broadband currents near Palau. *J. Phys. Oceanograph.*, 50:1489–1507.

Vosper, S., Castro, I., Snyder, W., and Mobbs, S. (1999). Experimental studies of strongly stratified flow past three-dimensional orography. *Journal of Fluid Mechanics*, 390:223–249.

Vosper, S. B. (2000). Three-dimensional numerical simulations of strongly stratified flow past conical orography. *J. Atmos. Sciences*, 57:3716–3739.

Warner, S. J. and MacCready, P. (2009). Dissecting the pressure field in tidal flow past a headland: When is form drag "real"? *J. Phys. Oceanograph.*, 39:2971–2983.

Warner, S. J. and MacCready, P. (2014). The dynamics of pressure and form drag on a sloping headland: Internal waves versus eddies. *J. Geophys. Res.*, 119(3):1554–1571.

Warner, S. J., MacCready, P., Moum, J. M., and Nash, J. D. (2012). Measurement of tidal form drag using seafloor pressure sensors . *J. Phys. Oceanograph.*, 43:1150–1172.

Wijesekera, H. W., Jarosz, E., Teague, W. J., Wang, D. W., Fribance, D. B., Moum, J. M., and Warner, S. J. (2014). Measurements of form and frictional drags over a rough topographic bank. *J. Phys. Oceanograph.*, 44:2409–2432.

Williamson, C. and Brown, G. (1998). A series in $1/\sqrt{Re}$ to represent the Strouhal-Reynolds number relationship of the cylinder wake. *Journal of Fluids and Structures*, 12:1073–1085.

Winters, K. and Armi, L. (2014). Topographic control of stratified flows: upstream jets, blocking and isolating layers. *J. Fluid Mech.*, 753:80–103.

Winters, K. B. (2015). Tidally driven mixing and dissipation in the stratified boundary layer above steep submarine topography. *Geophys. Res. Lett.*, 42:7123–7130.

Winters, K. B. and Armi, L. (2013). The response of a continuously stratified fluid to an oscillating flow past an obstacle. *J. Fluid Mech.*, 727:83–118.

Wolanski, E., Imberger, J., and Heron, M. L. (1984). Island wakes in shallow coastal waters. *J. Geophys. Res.*, 89:10553–10569.

Wunsch, C. and Ferrari, R. (2004). Vertical mixing, energy, and the general circulation of the

oceans. *Ann. Rev. Fluid Mech.*, 36:281–314.

Wykes, M. S. D. and Dalziel, S. B. (2014). Efficient mixing in stratified flows: Experimental study of a rayleigh-taylor unstable interface within an otherwise stable stratification. *J. Fluid Mech.*, 756:1027–1057.

Yang, L., Nikurashin, M., Hogg, A. M., and Sloyan, B. M. (2018). Energy loss from transient eddies due to lee wave generation in the southern ocean. *J. Phys. Oceanograph.*, 48:2867–2885.

Yu, X., Rosman, J. H., and Hench, J. L. (2018). Interaction of waves with idealised high-relief bottom roughness. *J. Geophys. Res.*, 123:3038–3059.

Yua, J., Zheng, Q., Jingd, Z., Qia, Y., Zhang, S., and Xie, L. (2018). Satellite observations of sub-mesoscale vortex trains in the western boundary of the South China Sea. *Journal of Marine Systems*, 183:56–62.

Zeiden, K. L., Ridnick, D. L., and MacKinnon, J. A. (2019). Glider observations of a mesoscale oceanic island wake. *J. Phys. Oceanograph.*, 49:2217–2235.

Zhang, L., Buijsman, M. C., Comino, E., and Swinney, H. L. (2017). Internal wave generation by tidal flow over periodically and randomly distributed seamounts. *J. Geophys. Res.*, 122:5063–5074.

Zhang, X. and Nikurashin, M. (2020). Small scale topographic form stress and local dynamics of the Southern ocean. *J. Geophys. Res.*, 125:e2019JC015420.

Zheng, Q., Lin, H., Meng, J., Hu, X., Song, Y. T., Zhang, Y., and Li, C. (2008). Sub-mesoscale ocean vortex trains in the Luzon Strait. *J. Geophys. Res.*, 113:1–12.